Electron Tunneling and Spin Relaxation in a Lateral Quantum Dot

by

Sami Amasha

B.A. in Physics and Math, University of Chicago, 2001

Submitted to the Department of Physics
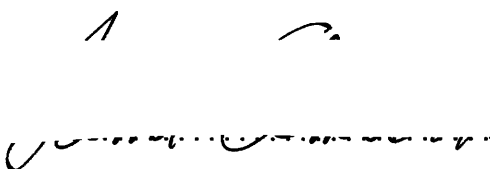in partial fulfillment of the requirements for the degree of
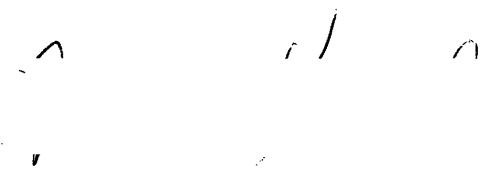
Doctor of Philosophy

at the

MASSACHUSETTS INSTITUTE OF TECHNOLOGY

February 2008

Author ...
Department of Physics
December 11, 2007

Certified by
Marc A. Kastner
Donner Professor of Physics and Dean of the School of Science
Thesis Supervisor

Accepted by ....
Thomas J. Greytak
Professor and Associate Department Head for Education
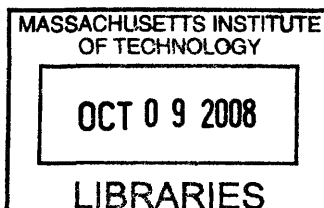
Electron Tunneling and Spin Relaxation in a Lateral Quantum Dot

by

Sami Amasha

Submitted to the Department of Physics
on December 11, 2007, in partial fulfillment of the
requirements for the degree of
Doctor of Philosophy

Abstract

We report measurements that use real-time charge sensing to probe a single-electron lateral quantum dot. The charge sensor is a quantum point contact (QPC) adjacent to the dot and the sensitivity is comparable to other QPC-based systems. We develop an automated feedback system to position the energies of the states in the dot with respect to the Fermi energy of the leads. We also develop a triggering system to identify electron tunneling events in real-time data.

Using real-time charge sensing, we measure the rate at which an electron tunnels onto or off of the dot. In zero magnetic field, we find that these rates depend exponentially on the voltages applied to the dot. We show that this dependence is consistent with a model that assumes elastic tunneling and accounts for the changes in the energies of the states in the dot relative to the heights of the tunnel barriers. In a parallel magnetic field B the spin states are split by the Zeeman energy and we measure the ratio of the rates for tunneling into the excited and ground spin states of an empty dot. We find that the ratio decreases with increasing B. However, by adjusting the voltages on the surface gates to change the orbital configuration of the dot, we restore tunneling into the excited spin state.

We also measure the spin relaxation rate $W \equiv T_1^{-1}$ between the Zeeman split spin states for a single electron confined in the dot. At $B = 1$ T we find that $T_1 > 1$ s. The dependence of W on magnetic field is a power-law, and the exponent is consistent with the prediction for the spin relaxation mechanism of spin-orbit mediated coupling to piezoelectric phonons. Since spin relaxation involves the orbital states of the dot via the spin-orbit interaction, we can achieve electrical control over W by using the surface gates to manipulate the orbital states. We demonstrate that we can vary W by over an order of magnitude at fixed Zeeman splitting, and we extract the spin-orbit length, which describes the strength of the spin-orbit interaction in GaAs.

Thesis Supervisor: Marc A. Kastner
Title: Donner Professor of Physics and Dean of the School of Science

3

Acknowledgments

When I reflect on the six plus years that I have spent in graduate school, I remember plenty of perplexing problems, several exhilarating moments of insight, a few difficult times, and many incredibly good ones. Through all of this, I have had the encouragement, advice, and help of many people. Thus I think it is fitting to begin this thesis by acknowledging the people who have made this work possible.

First, I would like to thank my advisor Marc Kastner. Marc's enthusiasm and unwavering support for our research has been an inspiration. I admire his ability to identify important physical phenomena in data, and his good judgment in deciding on the most efficient way to investigate them. I have learned much from Marc's guidance and feel very fortunate to have had the opportunity to work with him.

Being in Marc's research group has given me the opportunity to work with and to get to know many talented people. Andrei Kogan is a superb experimental physicist, and he taught me the art of assembling a good experiment. Andrei also has a knack for asking penetrating, insightful questions, and I have tried to learn from his example. I have also gotten to know David Goldhaber-Gordon, who made the samples I first studied when I joined the Kastner group. David has the rare ability to devise and carry-out truly elegant experiments, and I appreciated his thoughtful comments about our experiments and our data. I am really looking forward to working for him as a post-doc in his research group.

When I started in the Kastner lab, Ghislain Granger took me under his wing, and taught me many basic lab skills, from the proper way to solder to how to transfer helium. He also became a good friend, with whom I could discuss things happening in the lab, as well as in my life outside the lab. I also want to thank Nicole Morgan, Jessica Thomas, and Marija Drndic for the many tips and pointers they gave me about lab work, classes, and MIT. Their advice made my transition to graduate school much smoother. I also benefited from the advice of Laurie Calvet and Boris Khaykovich.

A number of people in Marc's lab have contributed to the real-time charge detection measurements discussed in this thesis. I worked very closely with Kenny

MacLean to setup and perform all of these experiments, and this was one of the best experiences I have ever had. I really appreciate the ingenuity and commitment Kenny brings to his work. I am always excited to talk with Kenny about physics and experiments, because I know Kenny will have insights that will give me a deeper understanding of the subject. I also want to thank Dominik Zumbühl for not only helping to fabricate the quantum dot sample used in this work, but for the guidance and encouragement he provided during the course of these experiments. I really enjoyed discussing the data with Dominik, because he always has good ideas, as well as suggestions for further experiments. I am also grateful to Iuliana Radu for fabricating the quantum dot sample I have studied in this thesis. She is also a trusted friend, who I can go to for good advice about both science and life. In addition, Iuliana 'saved' me by converting me to Mozilla's Firefox and Open Office Draw. I am also indebted to both Iuliana and Andreas Klust for inviting me to share many holidays with them, when I could not leave MIT to see my own family.

During the time that I worked on the research in this thesis, I had the pleasure of being labmates with a number of people. Tamar Mentzel is an inquisitive and thorough scientist, whose passion for physics I admire. I am also grateful to her for teaching me how to run outside in cold weather! I have really enjoyed working with Ian Gelfand, whose irrepressible enthusiasm for research is an uplifting force. Ian's many fantastic stories have provided much entertainment, and I am happy that I got to contribute to one of them (the story of how our lab got a couch!). I have also enjoyed getting to know Colin Dillard and Jingshih Hu. Finally, I have had the opportunity to work with a fantastic group of MIT undergraduate students, including Colin Cross, Anat Burger, Jessica Schirmer, Vladimir Rosenhaus, KaiWing Fung, and Maria Schriver.

I also benefited from the help of a number of people in the scientific community. I am particularly grateful to the members of my committee, Ray Ashoori and Leonid Levitov. Ray has provided advice on everything from charge sensing, to putting together an effective presentation, and for this I am grateful. I really enjoyed discussing the data with Leonid, and his insights greatly helped my understanding of it. I also

through. I also want to thank my Uncle Eli and my cousins Mitchell & Lourdes, Gail & Jimi, and Elisa & Brett, as well as all their children, David, Steven, Eli, Michael, Amanda, Kai, and Savannah. So many times during both college and graduate school they invited me into their homes, and for this I am truly grateful.

Finally, this thesis is dedicated to two remarkable women who were significant influences in my life. My Grandmother Shirley Wein was a steady, loving presence. She never obsessed with daily tribulations, rather she focused on the big things: am I healthy and am I enjoying what I am doing? She brought perspective to life, and I am grateful to her for this. My Aunt Renee Zafrani was also an important role model. When she decided to do something, she always did it right: she prepared thoroughly, invested the necessary time and effort, and evaluated the results with an unparallel attention to detail. She always sought to learn new things, and every time I visited her she would asked me about my research and how my work could be applied. I am indebted to my Grandmother and my Aunt; I miss you both.

Contents

List of Figures

List of Tables

Chapter 1

Introduction

Advances in material processing and synthesis techniques have led to the development of a wide variety of nanoscale structures. One type of structure that has attracted much interest is the quantum dot [1, 2, 3, 4, 5]. A quantum dot consists of a droplet of electrons confined to a small region of space, where the typical length scales of the dot are less than 100 nm. On these short length scales, quantum mechanics is needed to understand the behavior of the dot.

There are several different types of quantum dots, including self-assembled dots [6], vertical quantum dots [5], and gate-defined dots on semiconductor heterostructures [4], carbon nanotubes [7], and semiconducting nanowires [8]. In this thesis, we study a gate-defined quantum dot (also called a lateral quantum dot or laterally gated quantum dot) on an AlGaAs/GaAs heterostructure. In this material, the band structure causes the conduction electrons to be confined in the direction perpendicular to the heterointerface, but the electrons are free to move in the plane of the interface and form a two dimensional electron gas (2DEG) [9]. We fabricate a lateral quantum dot on this heterostructure by patterning metallic gates on the surface. Applying negative voltages to these gates repels the electrons in the 2DEG underneath them, and isolates a small droplet of electrons, namely the quantum dot, from the remaining 2DEG regions, which are called the leads. The primary advantage of this type of quantum dot is that its properties can be tuned *in-situ* by adjusting the gate voltages. For example, we can control the rates at which electrons tunnel between

the dot and the leads. We can also control the number of electrons on the dot, thus we can view quantum dots as artificial atoms with a tunable atomic number [2].

Quantum dots can be used to model physical phenomena. For example, we construct a model Kondo system by using a quantum dot as an artificial magnetic impurity atom [10, 11, 12, 13]: a dot that contains an odd number of electrons has a net spin, and the electrons in the leads screen this net spin, much as conduction electrons screen magnetic impurity atoms in material systems. The advantage of the model system is that we can study the Kondo effect out of equilibrium and tune properties of the system [14], such as the Kondo temperature, that are fixed by chemistry in material systems. This ability allows us to test theoretical predictions about the Kondo effect. For example, theory predicts that the Kondo effect creates a peak in the density of states at the Fermi energy of the leads, and that applying a magnetic field splits this peak about the Fermi energy [15, 16, 17]. Using non-equilibrium measurements on a quantum dot, we can observe this splitting of the Kondo peak, and probe how the splitting depends on field [18, 19]. We also observe the photon-assisted Kondo effect in a quantum dot by using non-equilibrium measurements to observe the photon-assisted satellites [20].

Potential applications of lateral quantum dots extend beyond model systems and include applications based on the spin physics of the dot. Until recently, most electronic devices have used only the charge of the electron to store or transport information. The burgeoning field of spintronics [21, 22, 23] seeks to take advantage of the electron's spin degree of freedom to build improved electronic devices. For example, the rapid increase in the storage capacity of modern hard-drives is a result of technology based on giant magneto-resistance, which is a spin based effect. Quantum dots have several potential applications in spintronics. Quantum dots can be used as spin filters [24, 25] and spin pumps [26]. Individual quantum dots can also be used as spin memory [27, 28], where information is stored in the spin of an electron confined to the quantum dot.

Another important application of lateral quantum dots is quantum computing. Applying a magnetic field to the dot splits the spin-up and spin-down states of the

dot by the Zeeman energy. This provides a two level quantum system that can be used as a qubit [29], which is the basic unit in a quantum computer [30]. Recent work has demonstrated that quantum dots satisfy many of the criteria for a viable qubit [31]. Loss and DiVincenzo [29] have shown that all the necessary gate operations on a quantum dot qubit can be built out of two basic operations: the manipulation of a single spin in a quantum dot and the controlled coupling of the spins in two dots using the exchange interaction. Koppens *et al.* [32] have demonstrated single spin manipulation through electron spin resonance [33], while measurements by Petta *et al.* [34] have demonstrated the controlled coupling of spins in a double dot. Moreover, Elzerman *et al.* [35] and Hanson *et al.* [36] have demonstrated various methods to measure the spin of an electron in a dot, thus providing a reliable read-out for the qubit. An important remaining challenge is to understand and to control the interactions between the electron's spin and its solid-state environment.

The two most important of these interactions are the hyperfine and spin-orbit interactions. The hyperfine interaction causes decoherence of the spin states by coupling the electron's spin to nuclear spins [37, 38, 39, 40, 34, 41]; however, because the effective nuclear magnetic field changes slowly, coherent behavior is still observed and measurements show the decoherence time $T_2 \gtrsim 1$ μs [34]. Recently methods have been suggested for suppressing the hyperfine-induced decoherence [42, 43, 44].

The spin-orbit interaction (SOI) causes spin relaxation by mixing the orbital and spin states, thus providing a mechanism for coupling the spin to electric fluctuations in the environment of the dot [45, 46, 47, 48]. This coupling induces spin relaxation and brings the probabilities of being in the excited and ground spin states to thermal equilibrium. The timescale for energy relaxation is T_1, and since relaxation necessarily destroys any coherent spin state, it sets an upper limit on the decoherence time $T_2 < 2T_1$ [46]. Understanding and controlling the interactions between the dot and its environment is essential for developing lateral dots into viable qubits.

The spin readout techniques, as well as the studies of the decoherence and relaxation mechanisms discussed above, are possible because of the development of charge sensing techniques in quantum dots [49, 50, 51, 35]. Previously, most measurements

of lateral quantum dots involved applying a voltage across the dot and measuring the resulting current through the dot. To have measurable currents, electrons must tunnel onto and off of the dot frequently, and this tunneling necessarily disturbs the spin state of the dot. Much of the development of the lateral quantum dot qubit has relied on the use of a different method to measure the dot, namely charge sensing. In general, charge sensing consists of coupling the quantum dot to another system that is sensitive to the charge on the dot. By measuring the second system, one can then determine the charge on the dot. The advantage to charge sensing is that it is effective even when the tunneling rates between the dot and the leads are slow. In addition to making the measurements of relaxation and decoherence possible, charge sensing has been used to test predictions of counting statistics and correlations in quantum dots [52, 53, 54].

In the work reported in this thesis, we use real-time charge sensing techniques to measure electron tunneling and spin relaxation in a single-electron lateral quantum dot. The organization of this thesis is as follows. In Chapter 2 we introduce the basic physics of lateral quantum dots, in both zero and finite magnetic field. In Chapter 3, we discuss our real-time charge detection system in detail, as well as a novel triggering system we develop to handle the large amounts of data that we acquire.

In Chapter 4, we use our charge sensing system to study electron tunneling in a quantum dot. Section 4.3 focuses on tunneling in zero magnetic field. We show that the tunneling rates into and out of the quantum dot depend exponentially on the voltages applied to the dot, and that this dependence is consistent with a model that assumes elastic tunneling between the dot and the leads, and accounts for the energies of the states in the dot relative to the heights of the tunnel barriers. In Section 4.4, we study tunneling in a magnetic field. Previous experiments have shown that the spin polarization of the electrons emitted from a quantum dot in a magnetic field does not depend on the spin of the dot, contrary to expectation [55]. In this section we use real-time charge detection and gate pulsing techniques to measure tunneling into the spin states of an empty quantum dot. We find that the ratio of the rates for tunneling into the excited and ground spin states of the dot depends on the magnetic

field and the orbital configuration. We consider several possible explanations, but find that none of these account for the observed dependence. These observations further emphasize the need for a better understanding of the spin physics of tunneling in a quantum dot. Such an understanding could lead to new applications for dots in spintronics.

In Chapter 5, we describe techniques for measuring the spin relaxation time T_1. T_1 depends on the Zeeman splitting between the spin states, and by measuring T_1 as a function of magnetic field we determine that the spin relaxation mechanism in lateral quantum dots is spin-orbit mediated coupling to piezoelectric phonons. At low magnetic fields, T_1 becomes very long, and we find that $T_1 > 1$ s at $B = 1$ T. This result is very promising for applications of dots in quantum computing and as spin memory in spintronics.

In Chapter 6, we use our understanding of the mechanism of spin relaxation to exert electrical control over the spin relaxation rate at a constant Zeeman splitting. While the relaxation rate can be controlled using the magnetic field, electrical control is advantageous since it can be implemented locally and on fast timescales, and is amenable to scalable architectures. In this chapter, we demonstrate *in-situ* electrical control of the spin relaxation rate by using gate voltages to manipulate the mixing of the spin and orbital states. These results show the promise of dots in spintronics and are an important step toward controlling one of the interactions between the spin states of the dot and its solid-state environment.

Finally, Chapter 7 summarizes the work in this thesis and suggests directions for future research.

Chapter 2

Lateral Quantum Dots

This chapter briefly reviews the salient features of lateral quantum dots in AlGaAs/GaAs heterostructures. In the first section, we describe the heterostructure material used in the device which we study in this thesis. The second section introduces the basic physics of quantum dots, while the third section discusses transport measurements in dots. In the final section, we examine the effect of a magnetic field on the physics of the dot. For more details, the reader is referred to references [9], [4], [56],[57], and [58].

2.1   Heterostructure and device

To fabricate a lateral quantum dot (QD), one starts with an AlGaAs/GaAs heterostructure grown by molecular beam epitaxy (MBE). A typical heterostructure consists of a layer of $Al_{0.3}Ga_{0.7}As$ δ-doped with Si grown on top of a thick layer of GaAs. The Si is an n-type dopant and electrons move from the AlGaAs into the GaAs, leaving behind positively charged donor ions. These ions produce an electric field perpendicular to the interface that pulls the electrons back toward the AlGaAs [9]. Because of the offset between the AlGaAs and GaAs conduction bands, the electric field cannot pull the electrons back into the AlGaAs, and the electrons remained trapped at the interface, forming a two-dimensional electron gas (2DEG). The electrons are free to move in the plane of the interface, but they are confined in a
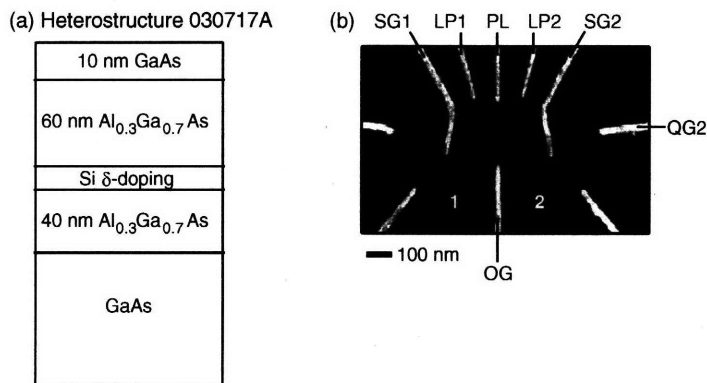
Figure 2-1: (a) Schematic of the heterostructure material used in the device which we study in this thesis. (b) Electron micrograph of the geometry of the gates of a device similar to that studied in this thesis. The unlabeled gates are not used and are kept grounded for all experiments.

triangular potential well in the direction perpendicular to the interface. The typical width of the wavefunction in the confined direction is about 5 nm.

A schematic of the heterostructure used to fabricate the QD we study in this thesis is shown in Fig. 2-1(a). This heterostructure, designated 030717A, has been grown by our collaborators M. P. Hanson and A. C. Gossard at the University of California, Santa Barbara. Starting from the surface, it consists of a 10 nm GaAs cap, followed by a 100 nm layer of $Al_{0.3}Ga_{0.7}As$ δ-doped with a single layer of Si with density 4×10^{12} cm^{-2}, and finally a thick layer of undoped GaAs [58]. The 2DEG formed at the AlGaAs/GaAs interface 110 nm below the surface has a density of 2.2×10^{11} cm^{-2} and a mobility of 6.4×10^5 cm^2/Vs [58, 59]. More details about this heterostructure can be found in Granger (2005) [58].

We use electron beam lithography to pattern Ti/Au gate electrodes on the surface of the heterostructure. The geometry of the gates for the device which we use (designated DDL UR Small, also known as DDS-ESR1), is similar to that shown in Fig. 2-1(b). Applying a negative voltage to gates SG1, LP1, PL, LP2, SG2, and OG depletes the 2DEG underneath them and forms a QD coupled by two tunnel barriers to the remaining 2DEG regions, which form the conducting leads (labeled 1 and 2 in Fig. 2-1(b)). Although the device looks like a double dot, we apply voltages to the

gates such that we form a single quantum dot. The gate geometry is based on that of Ciorga et al. [60] and allows us to confine one electron in the dot, or even to empty the dot. By applying a negative voltage to the gate QG2, we form a narrow channel called a quantum point contact (QPC) between SG2 and QG2 which can be used as a sensitive electrometer or charge sensor [50] for the quantum dot. We discuss charge sensing in detail in Chapter 3.

2.2   Physics of a quantum dot

By applying negative voltages to the gate electrodes, we create a confining potential that isolates the dot from the leads. Figure 2-2(a) shows an energy diagram of the dot. Several energy scales contribute to the physics of the system. The first of these is the temperature T, which sets the broadening of the Fermi distribution in the leads. For all the work in this thesis, we measure the dot in a dilution refrigerator and the electron temperature is $T \approx 120$ mK, giving $k_B T \approx 10$ μeV.

Another important energy scale is the single-particle orbital energy level spacing E_o. A confined electron has a discrete energy spectrum: the scale of the energy spacing between the different orbital states is $E_o \sim \frac{\hbar^2}{2m^*a^2}$, where a is the length scale of the confining potential, $m^* = 0.067m_e$ is the effective mass in GaAs, and m_e is the mass of a free electron. For the dot we study, $E_o \approx 2$ meV.

If electrons did not interact, then they would fill the dot in Fig. 2-2(a) with two electrons in the ground orbital state (one spin up and one spin down), two more in the first excited state, and so on until all the orbital states below the Fermi energy of the leads are filled. However, electrons repel each other, and if there is one electron on the dot then it takes a certain amount of energy to add a second electron to the dot in the ground orbital state. This energy is called the charging energy U_2 and the chemical potential of the 2-electron state is an energy U_2 above that of the 1-electron state (Fig. 2-2(a)) [58]. In our dot $U_2 \approx 4$ meV.

If the 2-electron state is above the Fermi energy of the leads, as in Fig. 2-2(a), then an electron cannot tunnel onto the dot. We can change the energies of the states by
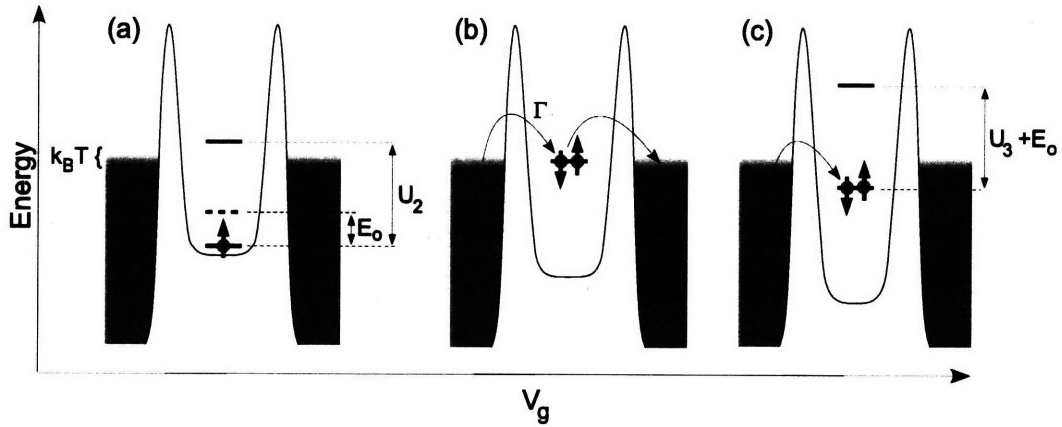
Figure 2-2: (a) Energy diagram for a single electron in a quantum dot. (b) As the gate voltages are made less negative, the energies of the levels in the dot decrease. When a level is aligned with the Fermi energy of the leads, an electron can tunnel onto and off of the dot. (c) When a level is brought beneath the energy of the leads, an electron tunnels onto the dot but cannot tunnel off again, increasing the number of electrons on the dot.

changing the voltage V_g on one or more of the gates that define the dot. By making the gate voltage less negative, we lower the energy of the 2-electron state and when it is aligned with the Fermi energy of the leads, electrons can tunnel onto and off of the dot as shown in Fig. 2-2(b).

If we make the voltage on the gate even less negative, as in Fig. 2-2(c), then the 2-electron state is below the Fermi energy of the leads. An electron can tunnel onto the dot, but it cannot tunnel off because there are no available hole states at this energy, leaving the dot with two electrons. In this way, we can control the number of electrons on the dot. In our device we can completely empty the dot and then add electrons one at a time, so we know exactly how many electrons are on the dot for a given set of gate voltages.

We can extend the simple state filling picture above to larger numbers of electrons in the dot. The third electron cannot go into the ground orbital state, rather it goes into the next available orbital state which is an energy E_o above the ground orbital state. Consequently, as shown in Fig. 2-2(c), the difference between the 2- and 3-electron states is $U_3 + E_o$, where U_3 is the energy caused by Coulomb repulsion

24

for adding the third electron. Assuming a simple state filling picture, the fourth electron goes into the same orbital state as the third (with opposite spin) to form a singlet and the difference in energy is U_4. We can continue to add electrons to the dot in this way. For understanding many features of dots, this simple state filling picture is adequate. However, it is important to note that more complicated electron configurations can occur. For example, exchange effects may make it more favorable for the fourth electron to occupy a higher energy orbital state so that the 4-electron state is a triplet state rather than a singlet state [58, 59]. Finally, we note that as we add more electrons to the dot, the charging energy approaches a constant U.

A final important energy scale is the intrinsic width in energy of a state in the dot. From the Uncertainty Principle, the width of a state is inversely proportional to the lifetime of the state. One contribution to the lifetime comes from the tunneling rate between the state and the leads [61]. When a level in the dot is aligned with the Fermi energy of the leads as in Fig. 2-2(b), an electron can tunnel onto and off of the dot with rate Γ. This rate is determined by the heights and widths of the tunnel barriers, which in turn depends on the voltages applied to the gates that form the barriers. If tunneling dominates the lifetime, then the average lifetime is $1/\Gamma$, and the state has a width of $\hbar\Gamma$ [61].

2.3 Transport measurements of a quantum dot

A common method for probing a QD is to measure electron transport through the dot. Electrical contact to the 2DEG is made using Ni/Ge/Au ohmic contacts that are fabricated with the device. These contacts to the 2DEG give access to the leads, which are often named drain and source following transistor terminology. The leads are explicitly labeled 'd' and 's' in Fig. 2-3 and correspond to leads 1 and 2, respectively. To measure the QD, we apply a voltage between the drain and source and measure the resulting current through the dot. The circuit we use is sketched in Fig. 2-3. The dc voltages for the gates and the drain-source bias are provided by a National Instruments 6703 analog output card in the data acquisition computer for
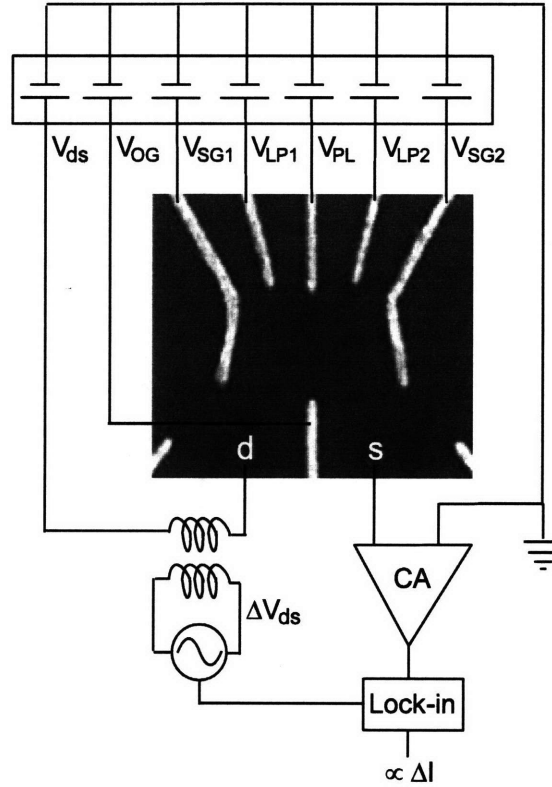
Figure 2-3: Sketch of the circuit we use for transport measurements of a quantum dot. The dc voltages on the gates and for the dc drain-source bias V_{ds} are obtained by dividing down the output of an analog output voltage card that is in the data acquisition computer. An oscillating voltage ΔV_{ds} is inductively coupled to V_{ds}, and this allows us to measure dI/dV_{ds}. CA denotes the current pre-amplifier.

the experiment. The voltage output of the card is divided down to smaller values and filtered before being applied to the QD.

A dc drain-source bias voltage V_{ds} is inductively coupled to an oscillating voltage source at frequency f_{ds} via a transformer; this allows us to introduce a small oscillating voltage ΔV_{ds} on top of the dc voltage [58]. The resulting current through the QD consists of a dc component and a component ΔI that oscillates at frequency f_{ds}. We amplify this current using an Ithaco 1211 current pre-amplifier and then measure the pre-amplifier output using a lock-in amplifier, which isolates the oscillating component ΔI. In this way, we measure the differential conductance $dI/dV_{ds} \approx \Delta I/\Delta V_{ds}$ of the QD [58]. We usually report the conductance in terms of $e^2/h \approx 1/25800 \ \Omega^{-1}$, which
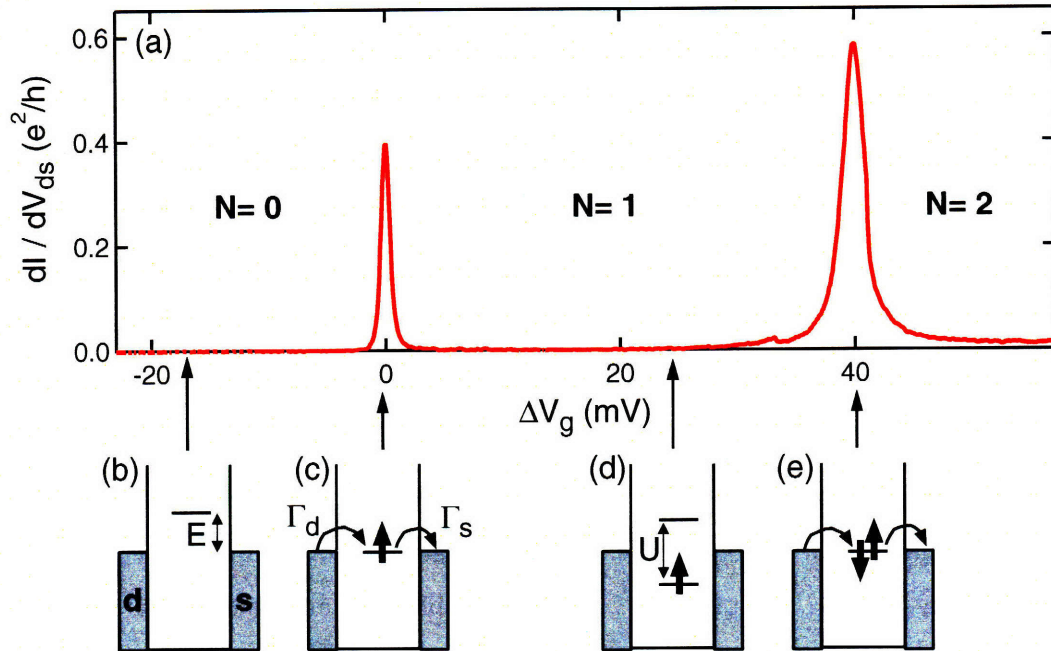
Figure 2-4: (a) Example of dI/dV_{ds} vs ΔV_g with $V_{ds} = 0$. $\Delta V_g = 0$ corresponds to the position of the first Coulomb blockade peak. The diagrams (b)-(e) show the energies of the states of the dot at the different gate voltages. The drain and source leads are labeled 'd' and 's' in (b).

is the fundamental quantum of conductance [9, 61].

Figure 2-4(a) shows a measurement of dI/dV_{ds} as we change the voltages on the gates; here ΔV_g refers to the change in the voltage applied to each of the three gates LP1, PL, and LP2. $\Delta V_g = 0$ is chosen to correspond to the position of the first Coulomb blockade peak. We understand the peaks in conductance using the considerations from the previous section. The dot diagrams in Figs. 2-4(b)-(e) illustrate the energies of the states of the dot at a given value of ΔV_g. At the most negative values of ΔV_g, the dot contains zero electrons and the 1-electron state is above the Fermi energy of the leads (Fig. 2-4(b)). Thus an electron cannot tunnel onto the dot and the conductance through the dot is low.

Changing the voltages on the gates changes the energies of the states of the dot. The energy E of the ground state relative to the Fermi energy of the source (Fig. 2-

4(b)) is

$$E = -e\frac{C_g'}{C_{tot}'}\Delta V_g$$

where C_g' is the combined capacitance of the dot to the three gates and C_{tot}' is the total capacitance of the dot to all the gates and leads [56, 58]. We define $\alpha_g = C_g'/C_{tot}'$. Making ΔV_g less negative lowers the energies of the states of the dot and when the energy of the 1-electron state is the same as the Fermi energy in the leads ($E = 0$), electrons can tunnel between the drain lead and the dot with rate Γ_d and between the source lead and the dot with rate Γ_s (Fig. 2-4(c)). Consequently, at this value of ΔV_g the conductance is at a maximum. As ΔV_g is made positive, the 1-electron state is filled. The energy of the 2-electron state is above the Fermi energy of the leads (Fig. 2-4(d)), so transport is once again blocked, and the conductance is low. At even more positive values of ΔV_g, the 2-electron state is at the same energy as the leads (Fig. 2-4(e)), and conductance is once again at a maximum. The conductance peaks are called Coulomb blockade peaks, and from the dot diagrams it is clear that the separation ΔV_{peaks} between the peaks is $\Delta V_{peaks} = U_2/e\alpha_g$.

We can understand the lineshape of the Coulomb blockade peaks. The width of a peak depends on the tunneling rate $\Gamma_t = \Gamma_s + \Gamma_d$ and the electron temperature T. The rate Γ_t determines the intrinsic width of the state while the temperature determines the width of the Fermi distribution of the leads, which act as probes of the quantum dot. In the limit where $\hbar\Gamma_t \gg k_B T$, the intrinsic width dominates and the lineshape is a Lorentzian [56, 61, 9]

$$G = \frac{2e^2}{h}\frac{\Gamma_s\Gamma_d}{\Gamma_s + \Gamma_d}\left(\frac{\Gamma_t}{(\frac{\Gamma_t}{2})^2 + (\frac{e\alpha_g}{\hbar}\Delta V_g)^2}\right) \tag{2.1}$$

which is characteristic of lifetime broadening. In the limit $\hbar\Gamma \ll k_B T$, the relevant width is that of the Fermi function. In this case, the lineshape is [56]:

$$G = \frac{2e^2}{h}\frac{\Gamma_s\Gamma_d}{\Gamma_s + \Gamma_d}\frac{h}{4k_B T}\cosh^{-2}\left(\frac{e\alpha_g\Delta V_g}{2k_B T}\right) \tag{2.2}$$

These lineshapes are illustrated by the data in Figs. 2-5(a) and (b). Figure 2-5(a)

28
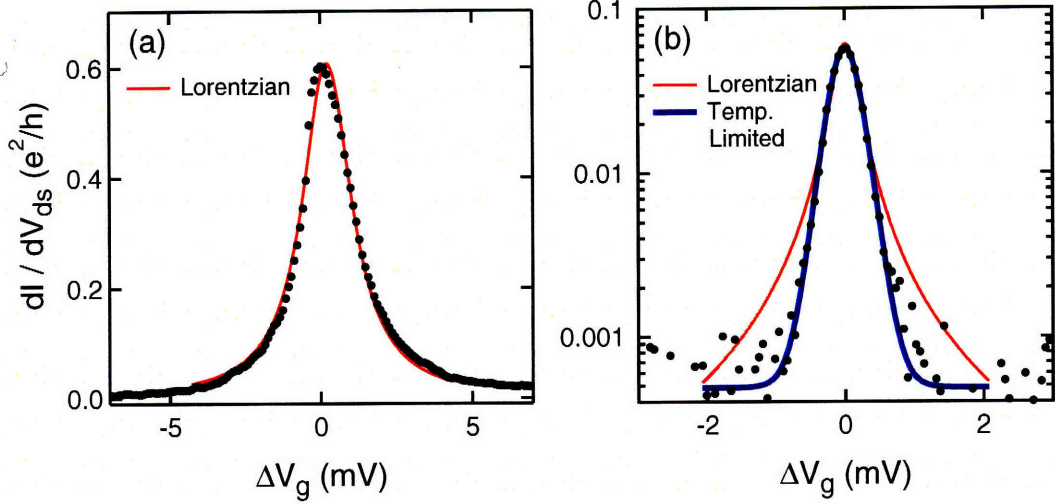
Figure 2-5: (a) Coulomb blockade peak where the peak width is dominated by lifetime broadening of the state. The line is a fit to the Lorentzian lineshape Eqn. 2.1 and is discussed in the text. (b) A Coulomb blockade peak where the width is dominated by the width of the Fermi distribution. The thin line shows a fit to the Lorentzian lineshape Eqn. 2.1, while the thick line shows a fit to the temperature limited lineshape Eqn. 2.2.

shows an example of a Coulomb blockade peak where we adjust the gate voltages so that the tunneling rates to the leads are large and the peak is lifetime broadened. The solid line is a fit to Eqn. 2.1 and it is in good agreement with the data. Using an estimate for α_g (we will discuss a method for measuring α_g later in this section), we find that $\hbar\Gamma_t \approx 150\mu eV$, corresponding to $\Gamma_t \approx 230$ GHz.

Figure 2-5(b) shows an example of a Coulomb blockade peak where we reduce the tunneling rates to the leads so we are in the temperature-limited regime. The thin solid line shows a fit to the Lorentzian lineshape and clearly it does not give good agreement with the data. The thick solid line shows a fit to the temperature-limited lineshape Eqn. 2.2 and is in much better agreement. From this fit and a separately measured value of α_g, we extract $T \approx 129$ mK.

We also measure the conductance as a function of the drain-source bias voltage V_{ds} and an example of this is shown in Fig. 2-6(a). The diagrams in Figs. 2-6(b)-(e) illustrate the position of the levels on the dot at the different values of V_{ds} labeled in
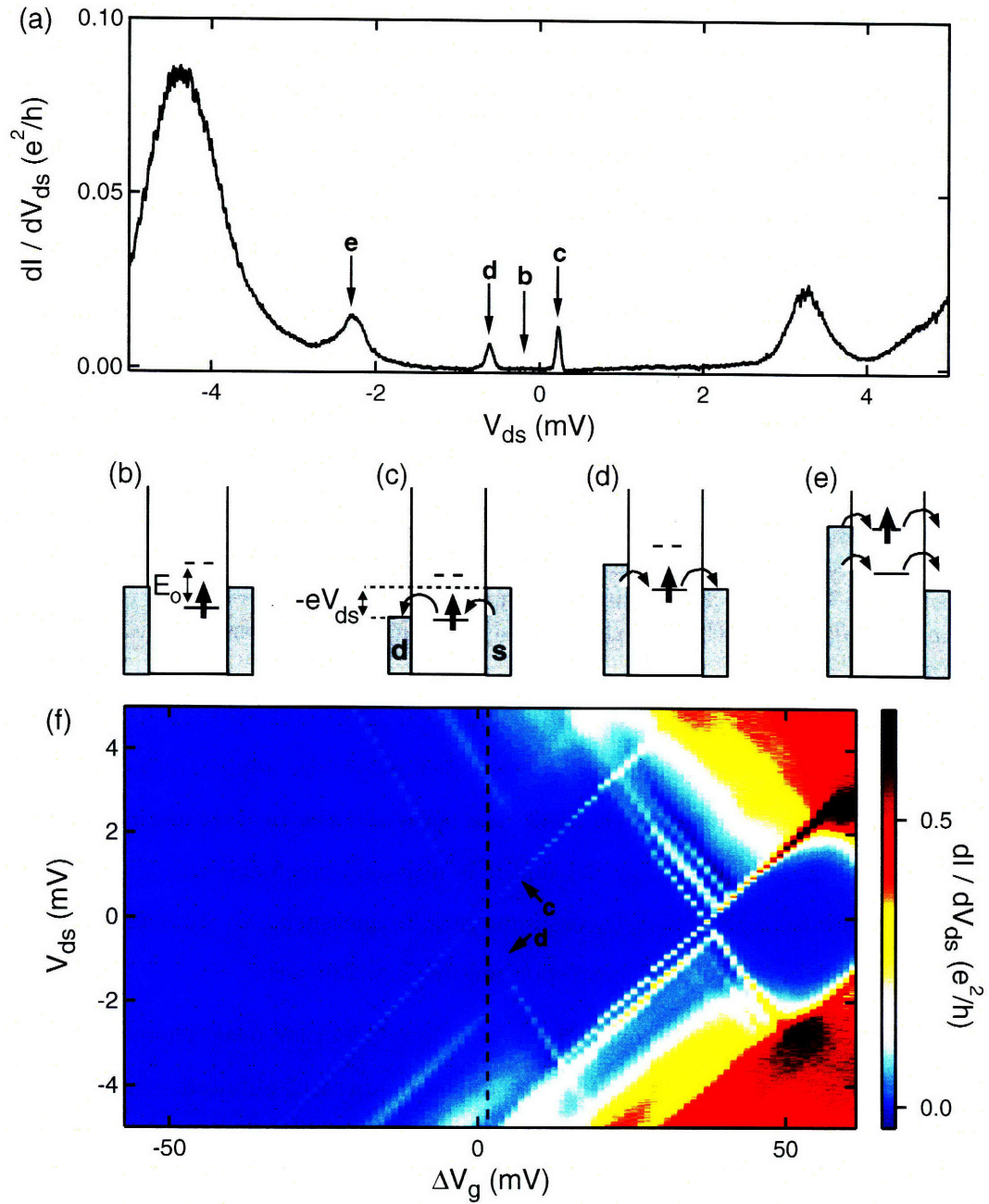
Figure 2-6: (a) Example of dI/dV_{ds} vs V_{ds} for a fixed ΔV_g. (b)-(e) Positions of the levels on the dot for different values of V_{ds} labeled in (a). (f) Example of dI/dV_{ds} vs V_{ds} and ΔV_g. $\Delta V_g = 0$ corresponds to the position of the first Coulomb blockade peak at $V_{ds} = 0$. The dashed line marks the position of the trace in (a). The transport lines corresponding to the dot configurations in (c) and (d) are also labeled.

Fig. 2-6(a). For this trace the dot contains one electron, and the gate voltages are set such that at $V_{ds} = 0$ the energy of the 1-electron state is just below the Fermi energy as shown in Fig. 2-6(b). The empty level in the diagram in Fig. 2-6(b) is an excited orbital state that is an energy E_o above the ground state. Since the electron is below the Fermi energy of both leads, it cannot tunnel off and transport is blocked, so the conductance is low.

The effect of applying V_{ds} is to change the Fermi energy of the drain lead (labeled 'd' in Fig. 2-6(c)) by an energy $-eV_{ds}$ relative to the source lead (labeled 's'), which is held at virtual ground because it is connected to the input of the current amplifier. Applying a positive V_{ds} lowers the Fermi energy of the drain lead (Fig. 2-6(c)). When it becomes aligned with the ground state of the dot, the electron can tunnel off of the dot and transport is permitted, leading to an increase in current. The current does not increase indefinitely with V_{ds}; rather, when the ground state is completely in the transport window (the state is higher in energy than the drain but lower in energy than the source) the current saturates at $I = e(\Gamma_s^{-1} + \Gamma_d^{-1})^{-1} = e\frac{\Gamma_s\Gamma_d}{\Gamma_s+\Gamma_d}$. This is the current corresponding to electrons tunneling through the dot one electron at a time. The step-like increase in current with V_{ds} gives a peak in dI/dV_{ds} when the level in the dot is aligned with the Fermi energy in the leads (Fig. 2-6(c)) and this peak is labeled as **c** in Fig. 2-6(a).

Applying a negative V_{ds} raises the Fermi energy of the drain lead as shown in Fig. 2-6(d). The capacitance C_{ds} between the drain lead and the dot causes the energies of the states of the dot to shift and this change is given by $-e\alpha_{ds}V_{ds}$, where $\alpha_{ds} = C_{ds}/C_{tot}$. For sufficiently negative V_{ds} the ground state of the dot is aligned with the source lead, giving a peak in dI/dV_{ds} as shown in Fig. 2-6(a). Making V_{ds} even more negative further increases the energy of the drain lead. When it is aligned with the energy of the excited orbital state (Fig. 2-6(e)) then there is an additional state for electrons to tunnel into: an electron can tunnel into either the excited orbital state or the ground orbital state. This additional channel for tunneling onto the dot results in a peak in dI/dV_{ds}, labeled **e** in Fig. 2-6(a).

Figure 2-6(f) shows an example of data where we vary both V_{ds} and ΔV_g. The

31

dashed line marks the position of the bias sweep shown in Fig. 2-6(a). The transport lines corresponding to the energy level configurations in Figs. 2-6(c) and (d) are labeled in Fig. 2-6(f). Along line **c**, the change in the energy of the ground state caused by ΔV_g is compensated by V_{ds} so that the ground state energy remains equal to the Fermi energy of the drain. The slope of this line depends on the capacitance ratios α_g and α_{ds} [58]. To calculate the slope of line **c**, we note that the energy of the ground state relative to the source lead is given by $E = -e\alpha_g \Delta V_g + -e\alpha_{ds} V_{ds}$, and that this must be equal to the energy of the drain lead. $E = -eV_{ds}$. This condition gives $V_{ds} = m_c \Delta V_g$ with slope $m_c = \alpha_g/(1 - \alpha_{ds})$. For the configuration in Fig. 2-6(d), $E = -e\alpha_g \Delta V_g + -e\alpha_{ds} V_{ds}$ and the energy of the ground state must be equal to that of the source lead, so $E = 0$. This gives the slope $m_d = V_{ds}/\Delta V_g = -\alpha_g/\alpha_{ds}$. Thus by measuring the slopes of these two lines, we can determine the capacitance ratios α_g and α_{ds}.

Inside the lines labeled **c** and **d** in Fig. 2-6(f) electrons cannot tunnel onto and off of the dot, so the number of electrons on the dot is fixed [58]. In particular, for $\Delta V_g < 0$ these lines do not intersect other transport lines even for very large values of V_{ds}. This is the signature that there are no electrons on the dot for $\Delta V_g < 0$.

2.4 Quantum dot in a magnetic field

The effects of applying a magnetic field to a quantum dot depend on the orientation of the field with respect to the 2DEG. Applying the field perpendicular to the 2DEG leads to exchange effects in multi-electron dots [62, 63, 64, 65]. These effects give the spin states different spatial distributions, which influences the coupling of the spin states to the leads [63, 65]. A perpendicular field can also influence the confinement potential felt by the electrons [66]. Finally, a perpendicular field causes the energies of the electrons in the leads to become quantized into Landau levels, and this affects transport through the dot [60].

To avoid the orbital and exchange effects associated with a perpendicular magnetic field, we apply the field parallel to the plane of the 2DEG. Since the electrons are
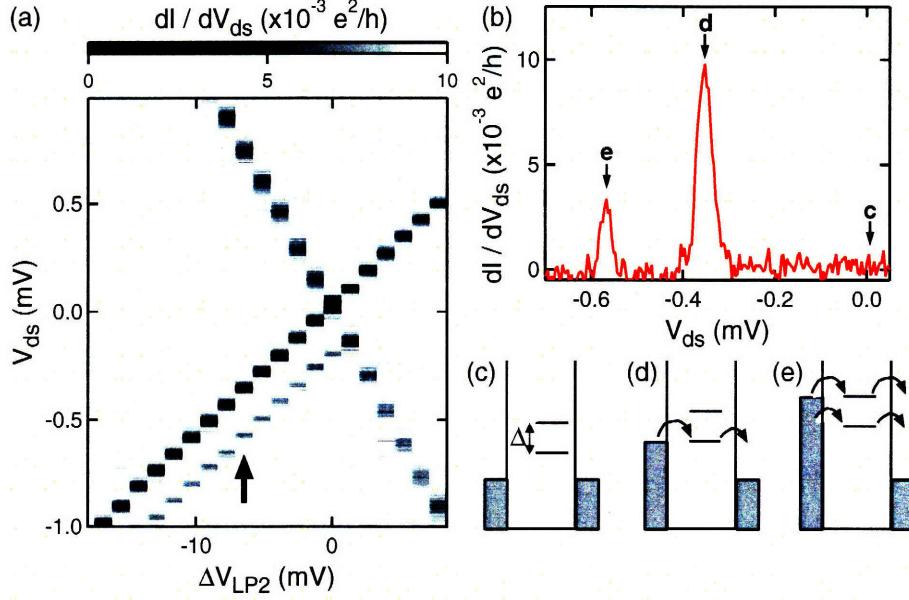
Figure 2-7: (a) dI/dV_{ds} as a function of ΔV_{LP2} and V_{ds} at $B = 6$ T. $\Delta V_{LP2} = 0$ corresponds to the position of the Coulomb blockade peak at $V_{ds} = 0$. The transport line marked by the arrow is caused by tunneling through the excited spin state. (b) dI/dV_{ds} vs V_{ds} at $\Delta V_{LP2} = -6.5$ mV. (c)-(e) Energies of the states of the dot for the different values of V_{ds} labeled in (b).

tightly confined in the direction perpendicular to the 2DEG (the z direction), the electrons do not form Landau levels. However, the field still couples to the spin of an electron confined in the dot. The interaction is given by $H = \frac{g\mu_B}{\hbar}\mathbf{S}\cdot\mathbf{B}$, where $\mathbf{B}$ is the magnetic field, $\mu_B = 58$ μeV/T is the Bohr magneton, and the spin operators $\mathbf{S} = \frac{\hbar}{2}\boldsymbol{\sigma}$, where $\boldsymbol{\sigma}$ are the Pauli matrices. For electrons in the GaAs conduction band, $g = -0.44$ [67]. This is different from the value of g in vacuum because of the effects of the spin-orbit interaction on the band structure of GaAs [68]. Thus the effect of the magnetic field on the quantum dot is to split the spin states of the dot by the Zeeman energy $\Delta = |g|\mu_B B$. The spin-up state, in which the spin is aligned with the magnetic field, is the ground spin state, while the spin-down state, which corresponds to the spin being anti-aligned with the field, is the excited spin state.

We observe this spin splitting using transport measurements [69]. Fig. 2-7(a) shows a measurement of dI/dV_{ds} as a function of ΔV_{LP2} and V_{ds} in a magnetic field

$B = 6$ T. The extra transport line marked by the arrow in the figure is caused by transport through the excited spin state[1]. Figure 2-7(b) shows a measurement of dI/dV_{ds} vs V_{ds} taken at $\Delta V_{LP2} = -6.5$ mV, while the diagrams in Figs. 2-7(c)-(e) show the energies of the spin states at the various values of V_{ds} that are labeled in Fig. 2-7(b). At $V_{ds} = 0$, both spin states are above the Fermi energy of the leads, as shown in Fig. 2-7(c). Making V_{ds} more negative raises the Fermi energy of the drain lead, and when it is equal to the energy of the ground spin state, electrons can tunnel from the drain to the source. This causes a peak in dI/dV_{ds}, labeled **d** in Fig. 2-7(b). At even more negative V_{ds}, the drain lead is at the same energy as the excited spin state, and this produces a second peak in dI/dV_{ds}, labeled **e** in Fig. 2-7(b).

From these data, we can determine Δ. We let V_{grnd} be the position of the peak labeled **d** in Fig. 2-7(b). Then V_{grnd} satisfies the condition $-eV_{grnd} = -e\alpha_{ds}V_{grnd} - e\alpha_{LP2}\Delta V_{LP2}$. Similarly, V_{exc} is the position of the peak labeled **e** and it satisfies $-eV_{exc} = -e\alpha_{ds}V_{exc} - e\alpha_{LP2}\Delta V_{LP2} + \Delta$. Subtracting these two equations and re-arranging the terms gives $\Delta = -e(1 - \alpha_{ds})(V_{exc} - V_{grnd})$, so from the peak spacing, we can extract Δ.

While we can use this type of transport measurement to find the Zeeman splitting, a number of factors contribute to uncertainty in the measurement. First, the measurement depends on aligning the spin states in the dot with the Fermi energy of the drain lead. However charge fluctuations in the heterostructure can electrostatically couple to the states in the dot and randomly shift their energies by small amounts [72]. This leads to uncertainty in the positions of the peaks. Also, uncertainty in the measurement of α_{ds} contributes to the error in Δ.

To avoid these problems, we measure the Zeeman splitting using inelastic spin-flip cotunneling spectroscopy [18]. We consider a dot that contains an odd number N of electrons, so that it has a net spin as shown in Fig. 2-8(a). When the energy of the $N + 1$-electron state is above the Fermi energy of the leads, an electron cannot tunnel onto the dot and transport is blocked. However, from the Uncertainty Principle, an electron can virtually tunnel onto the dot for a time on the order of $\hbar/U$ (Fig. 2-8(b)),

---

[1]We do not observe a corresponding transport line at $V_{ds} > 0$ because $\Gamma_s \gg \Gamma_d$ [70, 71].
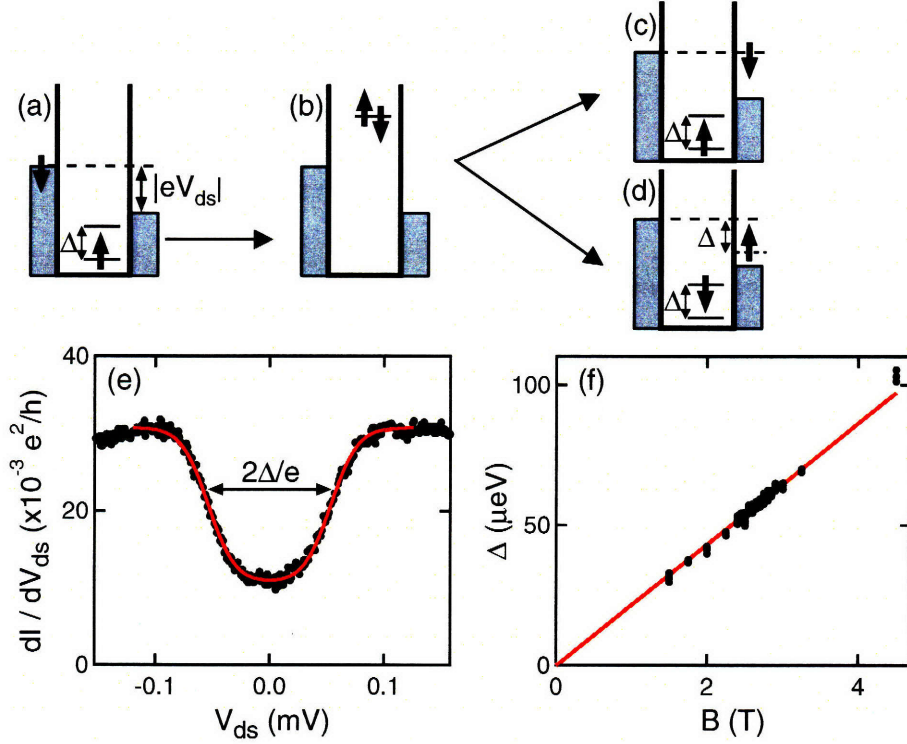
Figure 2-8: (a)-(d) are diagrams illustrating cotunneling. (e) Example of the steps in conductance caused by inelastic spin-flip cotunneling at $B = 2.5$ T. The solid curve is a fit discussed in the text. (f) Measurements of Δ as a function of B from inelastic spin-flip cotunneling measurements like those in (e).

after which one of the electrons tunnels off of the dot so that energy is conserved [73]. This process is called cotunneling [74, 75].

For $|eV_{ds}| < \Delta$ cotunneling is an elastic process, and the final state of the dot has the same energy as the initial state (Fig. 2-8(c)). However, for $|eV_{ds}| > \Delta$, cotunneling can also be an inelastic process and leave the dot in the excited spin state (Fig. 2-8(d)). This additional cotunneling process causes an increase in the conductance dI/dV_{ds} for $|V_{ds}| > \Delta/e$, as is shown by the data in Fig. 2-8(e). The width of the cotunneling gap is a direct measure of $2\Delta/e$. For a cotunneling process with negligible intrinsic width, the lineshape of the gap is given by [76]:

$$\frac{dI}{dV_{ds}} = C_e + C_i \left[F\left(\frac{eV_{ds} + \Delta}{k_B T}\right) + F\left(-\frac{eV_{ds} - \Delta}{k_B T}\right) \right]$$

35

where, C_e is the conductance from elastic cotunneling. C_i describes the additional contribution from inelastic cotunneling, and

$$F(x) = (1 + (x - 1)\exp(x))/(\exp(x) - 1)^2.$$

This lineshape has steps centered at $V_{ds} = \pm\Delta/e$ with width $5.4k_BT/e$. The solid line in Fig. 2-8(e) shows the result of fitting this lineshape to the data, and from this fit we extract Δ. Using inelastic spin-flip cotunneling to measure Δ is advantageous because the positions in V_{ds} of the steps in conductance do not depend on aligning the states with the Fermi levels in the leads, and so this measurement is not sensitive to charge fluctuations. Also, this measurement of Δ does not require measuring α_{ds}. Using inelastic cotunneling, we measure Δ as a function of B and the data is shown in Fig. 2-8(f). We fit these data to $\Delta = |g|\mu_B B$ (solid line in Fig. 2-8(f)) and from this we obtain $|g| = 0.37$.

Since cotunneling involves a virtual intermediate state, it is a higher order process than resonant tunneling through the dot. The tunneling rate of a cotunneling process is of the order $\hbar\Gamma^2/U$ [73]. Thus cotunneling is significant when $\hbar\Gamma$ is comparable to U. In the following chapters, we apply voltages to the gates so that $\Gamma \lesssim 1000$ Hz $\ll U/\hbar$, and in this regime cotunneling gives a negligible contribution to the tunneling rates.

Chapter 3

Real-Time Charge Sensing

In most of the work reported in this thesis, we study a quantum dot where the tunneling rate between the dot and its leads is very slow. In this limit, the current through the dot is small or non-existent and we cannot measure the dot using transport techniques. Consequently, we use a different method of measuring the dot, namely charge sensing [50, 49, 51, 77, 35, 78, 79, 80]. The first two sections of this chapter introduce how we implement real-time charge sensing to measure a quantum dot and discuss the characterization of this real-time charge sensing system. The final section describes the triggering system we develop in conjunction with the real-time charge sensing system in order to identify electron tunneling events efficiently. We use this triggering system extensively in the measurements described in the following chapters.

3.1 Charge sensing in real time

There is a lower limit to the tunneling rate that one can measure using transport techniques (Fig. 3-1(a)). Using a very low noise transport circuit, one can in principle measure currents as low as $I_{min} \approx 10$ fA. The current through the dot is approximately $I_{dot} \approx e\Gamma$, where Γ is the tunneling rate through the barriers. This puts a lower limit on the tunneling rate that we can measure using transport: $\Gamma_{min} \approx I_{min}/e \approx 100$ kHz. For the work in this thesis, we want to detect electrons tunneling onto and off of the dot at rates slower than this.
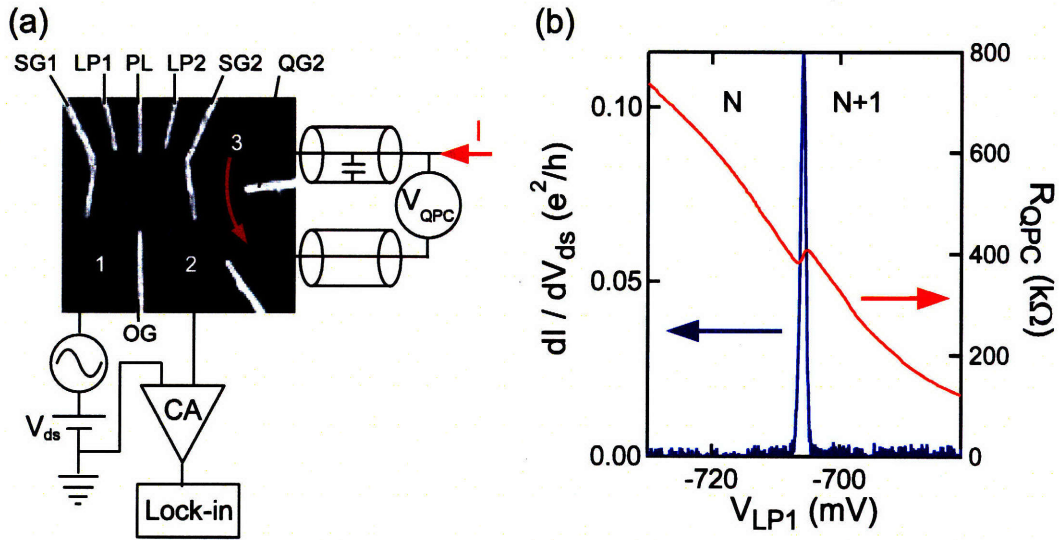
Figure 3-1: (a) Circuit diagram for measuring transport and charge sensing in a quantum dot. Negative voltages are applied to the labeled gates to form the dot and the adjacent QPC charge sensor; the unlabeled gate is grounded. The leads are numbered 1-3: lead 1 is the drain for the transport circuit, lead 3 is the drain for the QPC circuit, and lead 2 is the source for both circuits. The drain-source bias voltage V_{ds} is applied between leads 1 and 2. The arrows illustrate the different current paths for transport (dotted line) and charge sensing (solid line). (b) Simultaneous measurement of transport (left axis) and charge sensing (right axis). The current bias $I = \Delta I + I_{dc}$, and for these data $\Delta I = 0.2$ nArms and $I_{dc} = 0$.

To measure electron tunneling events at these slow rates we use charge sensing. The charge sensor for our quantum dot is a quantum point contact (QPC) adjacent to the dot [50, 79]. A QPC is a narrow 1-dimensional conducting channel [81, 82], and in our device it is formed between the gates labeled SG2 and QG2 in Fig. 3-1(a). Applying a slightly more negative voltage to either of the gates SG2 or QG2 changes the resistance of the QPC[1] because this voltage has the effect of changing the electrochemical potential of the channel. Adding an electron to the quantum dot has the same effect on the resistance because the negative charge of the electron changes the electrochemical potential of the QPC in the same way as a slightly more negative

---

[1]In many QPCs, the conductance decreases in steps of $2e^2/h$ as the gates are made more negative [81, 82] in zero magnetic field. We do not observe quantized conductance in our QPC, but this is not necessary for charge sensing. All that is required is that the conductance of the QPC vary with gate voltage.

gate voltage. In essence, the electron gates the QPC and in this way the QPC serves as a sensitive electrometer for detecting charge on the quantum dot [50].

We measure the average differential resistance R_{QPC} of the QPC using the circuit sketched in Fig. 3-1(a). We source a small current $I = I_{dc} + \Delta I$ that contains a dc component I_{dc} and an ac component ΔI. By measuring the average voltage ΔV_{QPC} across the QPC at the frequency of the ac excitation, we measure $R_{QPC} = \Delta V_{QPC}/\Delta I$. If the tunneling rates between the dot and its leads are large enough, then we can measure transport and charge sensing simultaneously, and such a measurement is shown in Fig. 3-1(b) [79]. As we make the voltage on gate LP1 less negative, R_{QPC} generally decreases because the capacitance between LP1 and the QPC causes the electrochemical potential of the channel to decrease. The Coulomb blockade peak in transport marks the gate voltage where the dot is transitioning between the N-electron and $N + 1$-electron states. At precisely this voltage, R_{QPC} increases because of the addition of an electron to the dot. In this way we use charge sensing to probe the number of electrons on the dot.

The great advantage of this method is that it functions even when we make the voltages on gates SG1, SG2, and OG more negative so that the tunneling rates between the dot and its leads are too small to be detected by transport measurements. Figure 3-2(a) shows an example of charge sensing data taken in the regime where we cannot measure transport, and the electrons are clearly visible in the data. Here ΔV_g refers to the change in the voltage applied to the three gates LP1, PL, and LP2. A striking feature of these data is that the behavior of the QPC as a function of the gate voltages is far from the ideal. In fact, over certain ranges in ΔV_g, we see that R_{QPC} actually *decreases* as the gate voltages are made more negative. Resonances in QPCs used as charge sensors have been observed before [83] and the lack of ideal behavior does not affect the QPC's ability to function as a charge sensor. All that is necessary for charge sensing is for R_{QPC} to be sensitive to gate voltage: then the effect of adding an electron is the same as making the gate voltages slightly more negative. Depending on whether R_{QPC} increases or decreases with more negative gate voltages, adding an electron will increase or decrease R_{QPC}, respectively (these
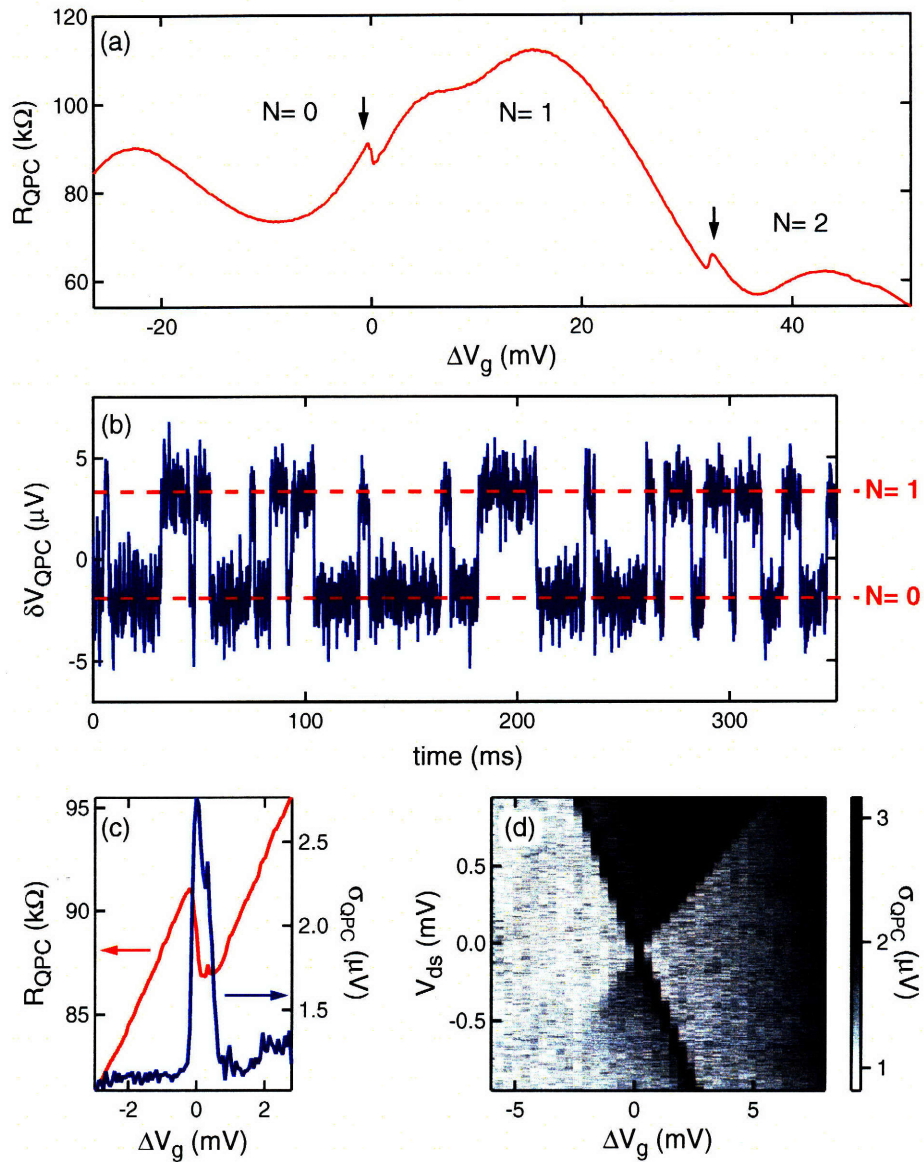
Figure 3-2: (a) Charge sensing measurement over a range of gate voltages. ΔV_g refers to the change in the voltage applied to the three gates LP1, PL, and LP2. The arrows mark the gate voltages where the number of electrons on the dot changes, and the number of electrons on the dot in each voltage range is indicated. (b) Real-time measurement of the fluctuation in voltage across the QPC caused by electron tunneling events. (c) Measurement of R_{QPC} (left axis) and the voltage noise across the QPC (right axis) as a function of the gate voltages. The voltage noise peaks at the gate voltages corresponding to the 0-1 charge transition. (d) Measurement of the QPC voltage noise as a function of V_{ds} and ΔV_g. The Coulomb blockade diamond confirms that the voltage transitions in (b) are caused by electrons tunneling onto and off of the quantum dot.

cases are demonstrated by the right and left arrows in Fig. 3-2(a), respectively).

We identify the electron at $\Delta V_g = 0$ as the first electron. One method we use to identify the first electron is to set the voltages on gates SG1, SG2, and OG to values that allow us to measure both transport and charge sensing and then identify the first electron using transport measurements like those in Fig. 2-6(f). We then gradually make the voltages on these gates more negative and follow the peak using transport and charge sensing until the transport signal becomes too small, at which point we use charge sensing alone. In this way we can identify the first electron and determine the number of electrons in the dot in each gate voltage range as shown in Fig. 3-2(a).

We can take charge sensing a step further. The response time of our charge detector is determined by R_{QPC} and the capacitance C of the coaxial line connecting the QPC to the voltage amplifier. The coaxial line has a capacitance $C \approx 500$ pF and for most measurements we set $R_{QPC} \approx 100$ kΩ. This gives a response time $\tau = R_{QPC}C \approx 50$ μs. The average time[2] an electron spends on or off the dot is Γ^{-1} and if we make the voltages on the gates SG1, SG2, and OG sufficiently negative such that $\Gamma^{-1} > \tau$, then the charge sensor responds to individual electron tunneling events in real time [77, 35, 78, 79, 80].

To observe this response, we set $\Delta I = 0$ and $I_{dc} \approx 1$ nA. The small change in the QPC resistance caused by an electron tunneling onto or off of the dot results in a small change in voltage δV_{QPC}. By measuring V_{QPC} as a function of time, we observe these tunneling events in real-time. Figure 3-2(b) shows an example of data taken with the gate voltages set at $\Delta V_g = 0$, so that the dot is at the $0 - 1$ electron transition. We see the voltage transitions between two well defined states: the upper state corresponds to 1 electron on the dot, while the lower state corresponds to 0 electrons on the dot.

We perform two tests to verify that these voltage transitions are associated with an electron tunneling onto and off of the quantum dot, as opposed to being caused by some other effect, such as electrons moving around randomly in the donor layer. The amount of time the electron spends on or off the dot is random, with the average

---

[2]We discuss the average time in more detail in Section 4.1.

being set by the tunneling rates. Thus the times at which the voltage transitions occur in Fig. 3-2(b) are random, and these data can be thought of as a type of noise, called telegraph noise [84]. We measure the amount of noise by finding the root-mean-square of a voltage trace like that in Fig. 3-2(b), and we denote this quantity σ_{QPC}. Figure 3-2(c) shows the results of measuring R_{QPC} (left axis) and the voltage noise σ_{QPC} (right axis) simultaneously. At both $\Delta V_g < 0$ and $\Delta V_g > 0$, σ_{QPC} is small because the dot has a fixed number of electrons (0 and 1 respectively). Near the charge transition, electron tunneling events occur and hence the noise increases, reaching a maximum at the charge transition. The correlation between the telegraph noise and the charge transition as measured by R_{QPC} is strong evidence that the voltage transitions are caused by electrons tunneling onto and off of the quantum dot.

We also measure σ_{QPC} as a function of ΔV_g and V_{ds}, much as we did with transport [53, 83]. Inside the Coulomb blockade diamonds charge transport is prohibited, and in the absence of electron tunneling events, σ_{QPC} should be small. Outside the diamonds, the level in the dot is in the transport window and hence electrons tunnel onto and off of the dot and produce voltage transitions, which we detect. Figure 3-2(d) shows an example of these type of data. The edges of the Coulomb diamond are clearly visible. This dependence of tunneling on ΔV_g and V_{ds} is exactly what we expect for electrons tunneling onto and off of a quantum dot, and confirms that this is the source of the transitions. From this diamond, we can also extract the capacitance ratios α_g and α_{ds} as discussed in 2.3.

3.2 Characterization of the real-time charge detection system

We use real-time charge detection extensively, so it is important that we characterize the detection system to understand the signal characteristics and the noise sources. Figure 3-3 shows a diagram of the circuit we use for real-time charge detection. We source a current $I_{dc} \approx 1$ nA through the QPC by applying a dc voltage across a large resistor $R_s = 10$ MΩ. For the measurements in this section, we use a resistor mounted near the sample at a temperature $T \approx 120$ mK; however, for other measurements we use a resistor at room temperature. We discuss the effects of having a room temperature source resistor at the end of this section. R_{QPC} is the resistance of the QPC, which changes in response to the change in the number of electrons on the dot, and C is the capacitance of the coaxial line going from the sample to the first stage amplifier mounted at the top of the cryostat.

The first stage amplifier is a Signal Recovery model 5184 voltage preamplifier powered using external batteries. This amplifier has a fixed gain of 10^3 and a bandwidth of approximately 1 MHz. This is much larger than the bandwidth of the charge sensor, which is limited by the rise-time $\tau = R_{QPC}C$ as discussed in the previous section.
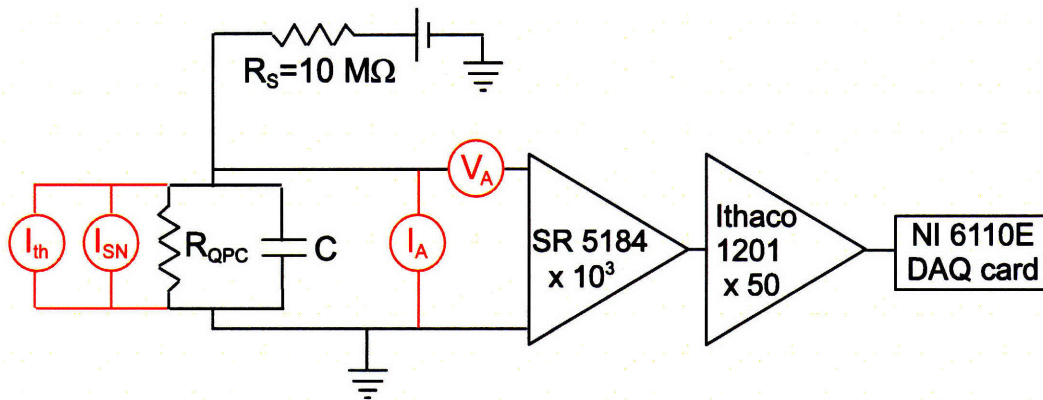
Figure 3-3: Diagram of the circuit we use for real-time charge sensing. Potential noise sources are shown, including Johnson noise I_{th}, shot noise I_{SN}, and the amplifier current and voltage noise, I_A and V_A respectively.
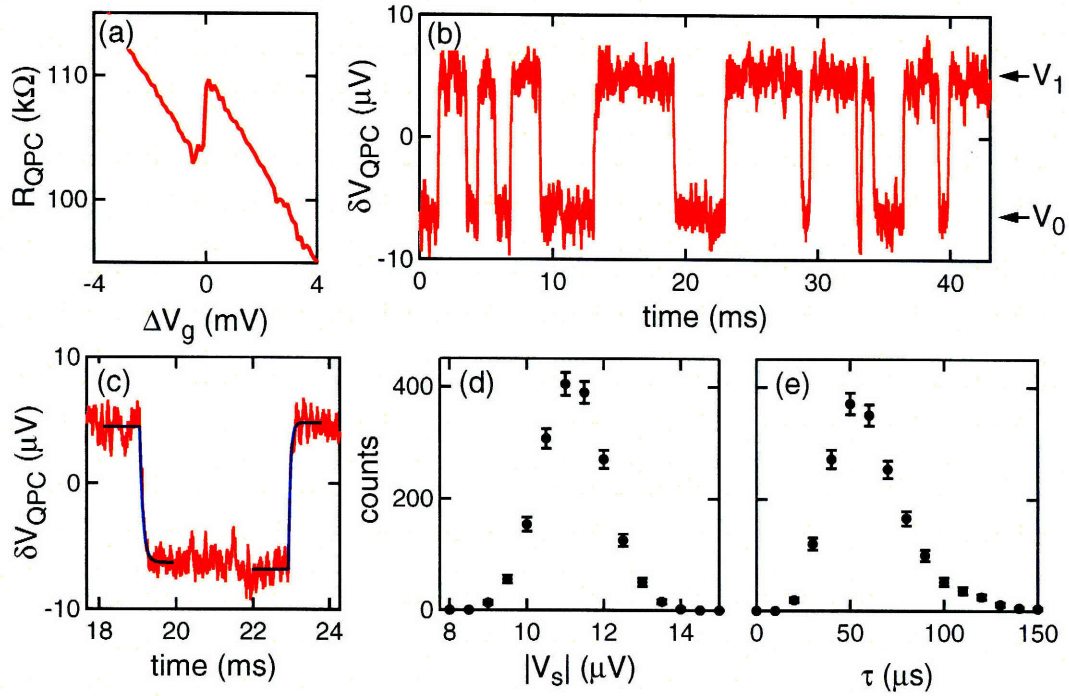
Figure 3-4: (a) R_{QPC} vs gate voltages for the first electron. (b) Real-time data showing electrons tunneling onto and off of the dot. V_0 and V_1 are the voltages corresponding to 0 or 1 electrons being on the dot, respectively. (c) Two electron tunneling events. The solid lines are fits to Eqn. 3.1 to extract the signal size $|V_s|$ and the rise time τ. (d) and (e) are histograms of the signal size and rise-time, respectively, obtained from fitting charge transitions like those in (c).

This amplifier is also ac coupled with a high-pass filter at approximately 0.5 Hz, which keeps the mean of the data at approximately 0. Following the first stage amplifier is an Ithaco Model 1201 voltage preamplifier, which is set to a gain of between 10 and 50. The low-pass filter on this amplifier is set at 100 kHz which is also above the bandwidth set by τ. The output of the second stage amplifier is passed out of the shielded room through high-frequency filters (not shown in Fig. 3-3) and is digitized by a NI 6110E card mounted in our data acquisition computer.

An example of real-time electron tunneling data is shown in Fig. 3-4(b). For these data $R_{QPC} \approx 100$ kΩ (Fig. 3-4(a)). The transitions between the $N = 0$ and $N = 1$ charge states are clearly visible in the real-time data in Fig. 3-4(b). If a charge

transition happens at time t_0 the shape of the resulting voltage signal $V_{QPC}(t)$ is

$$V_{QPC}(t) = \begin{cases} V_i & t < t_0 \\ V_i + V_s(1 - e^{-(t-t_0)/\tau}) & t \geq t_0 \end{cases} \qquad (3.1)$$

where V_i is the voltage corresponding to the dot state at time $t < t_0$ (so $V_i = V_0$ if $N = 0$ for $t < t_0$ and $V_i = V_1$ if $N = 1$ for $t < t_0$). The size of the signal is given by $|V_s| = V_1 - V_0$, where the sign of V_s depends on whether the transition is from $N = 1$ to 0 ($V_s < 0$) or $N = 0$ to 1 ($V_s > 0$). Figure 3-4(c) shows the results of fitting two transitions to Eqn. 3.1 and the agreement is excellent. From these fits, we extract V_s and τ and Fig. 3-4(d) and (e) show histograms of the results of fitting approximately 1800 charge transitions. We see that $\tau \approx 60$ μs while the average signal size is $|V_s| = 11.2$ μV, which is approximately 9% of the total voltage across the QPC. This value of τ is consistent with our estimate of $\tau = R_{QPC}C \approx 50$ μs.

To measure the noise of the detection system, we acquire data when the ground state of the dot is above the Fermi energy of the leads, so that the dot contains 0 electrons and there is no tunneling between the dot and the leads. In this case the voltage fluctuations across R_{QPC} are caused by noise sources and we record and analyze 10 s of such data. We find that the total noise is 1.2 μVrms, which corresponds to a noise of 0.11 electrons. Figure 3-5 shows a Fourier analysis of the data: Fig. 3-5(b) shows the noise spectrum $V_n(f)$ while Fig. 3-5(a) shows the integrated noise $\mathcal{V}(f) \equiv \left(\int_0^f V_n(f)^2 df \right)^{1/2}$. The noise spectrum rolls-off at frequencies $f \gtrsim 3$ kHz because of the time-constant τ of the circuit.

A number of sources contribute to the noise spectrum, some of which are indicated in Fig. 3-3. One important source of noise is the first stage amplifier. This amplifier contributes two types of noise: there is a voltage noise V_A on its inputs and a noise current I_A that it sources through the circuit [85]. The specifications of the amplifier give the total expected noise for a given input resistance R as a function of frequency $V_{spec}(f, R)$, and we can compare these specifications to the measured spectrum. For an accurate comparison at frequencies $f > (2\pi\tau)^{-1} \approx 3$ kHz, care must be taken because in this range the capacitance C contributes to the total input impedance of
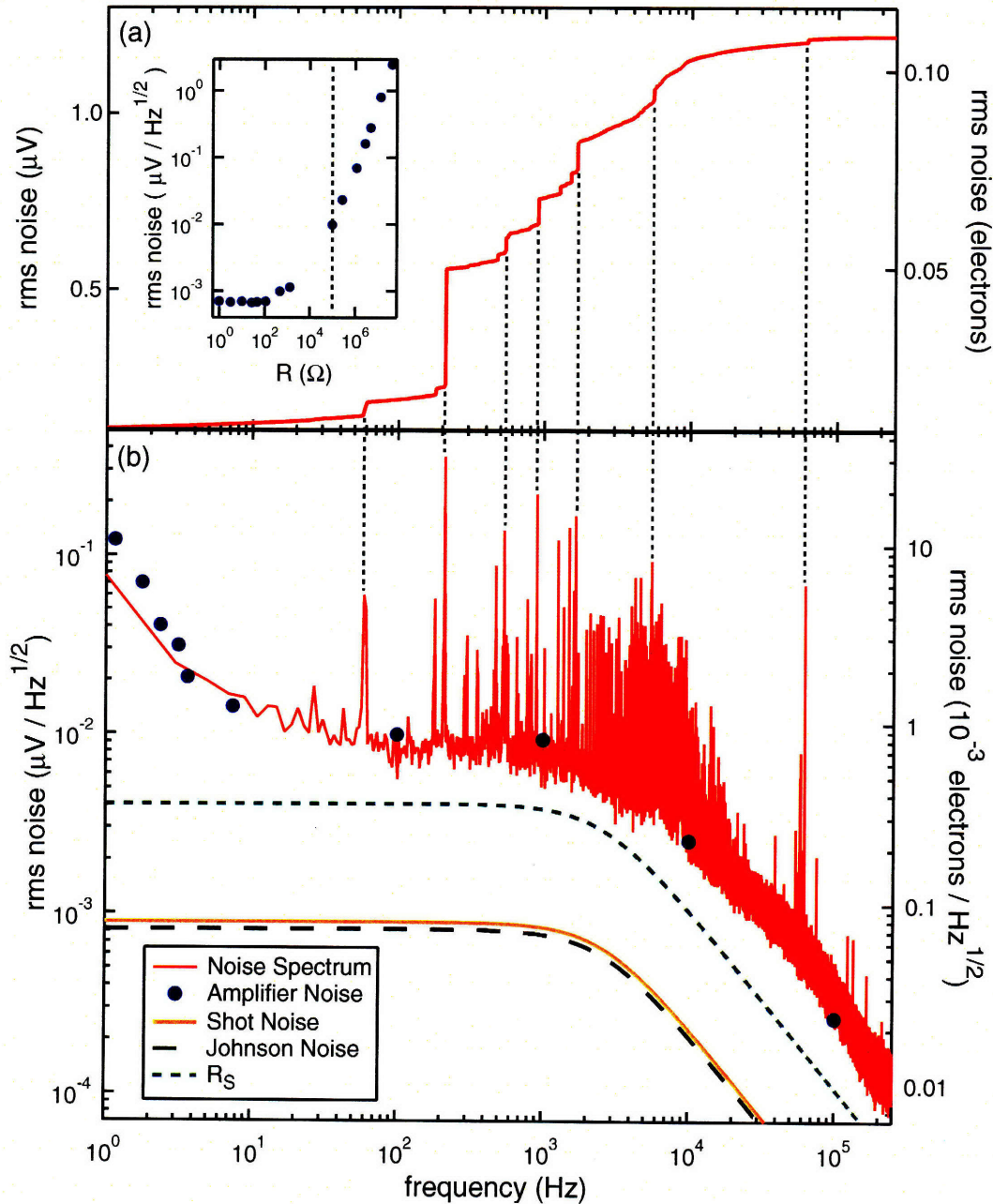
Figure 3-5: (a) Integrated noise $\mathcal{V}(f)$ and (b) noise spectrum $V_n(f)$ for the real-time charge detection system. The dashed vertical lines between (a) and (b) show how peaks in the noise spectrum give rise to sharp increases in the integrated noise. The filled circles and the lines in (b) show the expected contributions of various noise sources to the spectrum. The inset to (a) shows the specified amplifier noise as a function of the input resistance at a frequency of 1 kHz.

our circuit $Z(f) = R_{QPC}/(1 + i2\pi f\tau)$, whereas this capacitance is not present in the amplifier specifications. To account for this, we divide the specified amplifier noise $V_{spec}(f, R_{QPC})$ by $(1 + (2\pi f\tau)^2)^{1/2}$ with $\tau = 60$ μs; we will discuss the reasoning behind this approximation in the next paragraph. The specifications for the amplifier noise are shown by the filled circles in Fig. 3-5(b) and account for a good portion of the noise spectrum.

For a given resistance R on the input and a given frequency f, the amplifier specifications give the total noise $V_{spec} = (V_A^2 + (I_A R)^2)^{1/2}$. V_{spec} as a function of R at $f = 1$ kHz are shown in the inset of Fig. 3-5(a). We see that V_{spec} is approximately constant until $R \approx 100$ Ω, above which V_{spec} increases with increasing R. This indicates that the voltage noise V_A dominates the total noise at low resistances, while at larger resistances the current noise dominates [85]. The dashed line in the inset indicates $R = R_{QPC} = 100$ kΩ, and we see that at this resistance the current noise dominates. Then $V_{spec} \approx I_A R_{QPC}$ and dividing the specified voltage by $(1 + (2\pi f\tau)^2)^{1/2}$ as we do in Fig. 3-5(b) gives

$$\frac{V_{spec}}{(1 + (2\pi f\tau)^2)^{1/2}} \approx \frac{I_A R_{QPC}}{(1 + (2\pi f\tau)^2)^{1/2}} = I_A |Z(f)|$$

The total amplifier noise in our circuit is given by $V_{A,tot} = (V_A^2 + I_A^2 |Z(f)|^2)^{1/2}$, so we see that our treatment of the specified amplifier noise has accounted for the current noise contribution; there is a small contribution from the intrinsic voltage noise that we are missing. But the agreement between the specifications and the measurements indicate that this approximation is good.

While the amplifier noise describes the general features of the noise spectrum, it cannot account for the peaks in the noise at specific frequencies. These peaks have a number of possible causes. For example, the peak at 60 Hz is most likely caused by electrical pick-up because of the power-lines present in the shielded room that houses the experiment. Some of the noise peaks are also caused by vibrations in our system. The data for this spectrum has been taken in a 2.7 T magnetic field, so vibrations in the system can cause variations in the magnetic flux through the dilution refrigerator

47

wiring going to the QPC, inducing voltage pick-up at the frequency of the vibration. The presence of such pick-up is hardly surprising considering the minimal vibration isolation on the experimental setup. The contribution of these noise spikes to the total noise can be seen clearly in the integrated noise voltage in Fig. 3-5(a): the sharp jumps at specific frequencies are the contribution of the noise peaks.

Together the amplifier noise and the noise peaks account for the 1.2 μVrms of observed noise: the amplifier accounts for 0.7 μVrms while the peaks account for 1 μVrms (the noise contributions add in quadrature). Thus the charge detection system could benefit from improved vibration and electrical isolation to remove the noise peaks, as well as an improved first-stage amplifier.

Although the noise is dominated by the amplifier noise and the noise peaks, it is useful to consider some intrinsic sources of noise as these set the ultimate limit on the measurement technique. One such intrinsic noise source is the thermal or Johnson noise [85] across the QPC. We can model this as a noise current $I_{th} = (4k_B T/R_{QPC})^{1/2} \approx 8$ fA/Hz$^{1/2}$. Then the voltage V_{th} that falls across the parallel combination of R_{QPC} and C is

$$V_{th} = I_{th}|Z(f)| = \left(\frac{4k_B T R_{QPC}}{1 + (2\pi f \tau)^2} \right)^{1/2}$$

The Johnson noise spectrum is plotted in Fig. 3-5(b) and is a small contribution to the total noise.

Another intrinsic source of noise is the shot noise through the QPC, given by the current $I_{SN} = (2eI_{dc}\mathcal{T}(1 - \mathcal{T}))^{1/2}$ [86, 87], where $\mathcal{T}$ is the transmission coefficient through the QPC. We use $\mathcal{T} = 0.5$ to get a worst-case estimate of the noise. With this value, we estimate $I_{SN} \approx 9$ fA/Hz$^{1/2}$. As before, the voltage V_{SN} that we measure is

$$V_{SN} = I_{SN}|Z(f)| = \left(\frac{2eI_{dc}\mathcal{T}(1 - \mathcal{T})}{1 + (2\pi f \tau)^2} \right)^{1/2}$$

and this is plotted in Fig. 3-5(b) and is also a small contribution.

Finally, we consider the noise contribution from the source resistor R_s being at room temperature as opposed to cryogenic temperatures. The noise current from this

resistor is $I_s = (4k_BT/R_s)^{1/2} \approx 41$ fA/Hz$^{1/2}$ at $T = 300$ K. The noise voltage caused by a warm source resistor is

$$V_s = |Z(f)|I_s = \left(\frac{4k_BT}{R_s} \frac{R_{QPC}^2}{1 + (2\pi f\tau)^2} \right)^{1/2}$$

and the results are shown in Fig. 3-5(b) for $T = 300$ K. The data for the measured noise spectrum are taken with a source resistor at $T = 120$ mK so we see the noise contribution of a warm source resistor is less than that caused by the amplifier and the noise peaks. Thus we can use a warm source resistor in our experiments without introducing additional noise.

To determine a figure of merit to describe the sensitivity of our system, we divide the total noise of 0.11 electrons by the square root of our effective noise bandwidth[3] of $(4\tau)^{-1} = 4.2$ kHz. This gives a sensitivity of approximately 2×10^{-3} e/Hz$^{1/2}$.

We can compare this with the sensitivity of other charge sensing systems. Lu *et al.* [77] couple an Al SET to a quantum dot and measure the SET by embedding it in a radio frequency (RF) impedance matching network like that developed by Schoelkopf *et al.* [51]. This system has a sensitivity of 2×10^{-1} e/Hz$^{1/2}$ and a bandwidth of 1 MHz. While this system is very sensitive, it is also somewhat cumbersome to integrate with quantum dots because it requires fabricating a separate device coupled to the dot [88]. Elzerman *et al.* [35] also use a QPC as a charge detector, but instead of measuring the voltage across a current biased QPC, they use a low noise current amplifier to measure the changes in current through a voltage biased QPC. They have a sensitivity of approximately 1×10^{-3} e/Hz$^{1/2}$ [88], which is comparable to the sensitivity of our system. Using a cryogenic amplifier Vink *et al.* [89] increase the sensitivity to $\approx 4 \times 10^{-4}$ e/Hz$^{1/2}$. Reilly *et al.* [90] and Thalakulam *et al.* [91] have adapted the RF-SET techniques to measure a QPC coupled to a quantum dot. In Reilly *et al.* the system has a bandwidth of 8 MHz and a sensitivity of $\approx 10^{-3}$ e/Hz$^{1/2}$.

In the RF-QPC system, the noise is small enough that it is dominated by the shot noise of the QPC [90]. The limit on the sensitivity comes from the small signal

---

[3]The effective noise bandwidth of a single pole RC filter is given by $\int_0^\infty (1+(2\pi\tau f)^2)^{-1} df = (4\tau)^{-1}$

produced by an electron: a charge transition in a double dot changes the QPC conductance by only ~ 0.1%. Even in the measurements by Elzerman *et al.*, the change in current through the QPC caused by an electron tunneling event is only 1% [88]. One of the big advantages of our charge detection system is our large signal size: a tunneling electron causes a 9% change in the voltage across the QPC. This large signal size helps make our sensitivity comparable to the other QPC measurement techniques. This good signal size may be caused by making the SG2 gate narrow, which increases the coupling between the dot and the QPC [92]. Larger signals are observed in a QPC coupled to a quantum dot where the structures are defined by locally oxidizing the surface rather than by using surface gates. In this type of device, Gustavsson *et al.* [53] observe changes in current through the QPC on the order of 50%.

3.3 Edge and threshold triggers

After amplification, the voltage across the QPC is digitized by the NI6110E DAQ card as shown in Fig. 3-3. We set the card to digitize the voltages at 500 kHz, and more recently at 100 kHz. Thus a 10 s data trace can contain 1 million or more data points. Using the feedback techniques discussed in Section 4.2, we are able to keep the dot stable and take data for 12 to 16 hour periods, and up to 2 days if necessary. During this time we collect a large amount of data, from 20 to 65 gigabytes per day depending on the digitization rate. Storing this much data is impractical, so we develop tools to cull through the data quickly and identify and store the important information. These tools are called 'triggers'.

An example of a data trace is shown in Fig. 3-6(a). This trace contains 2500 points; however, the important information in the trace are the times and directions of the charge transitions (the direction of a charge transition is whether it corresponds to an electron tunneling onto or off of the dot). The function of the edge trigger is to identify these transitions in real-time data; essentially, it is an edge finder. A simple way of finding an edge is to take the derivative of the data. However, because of the
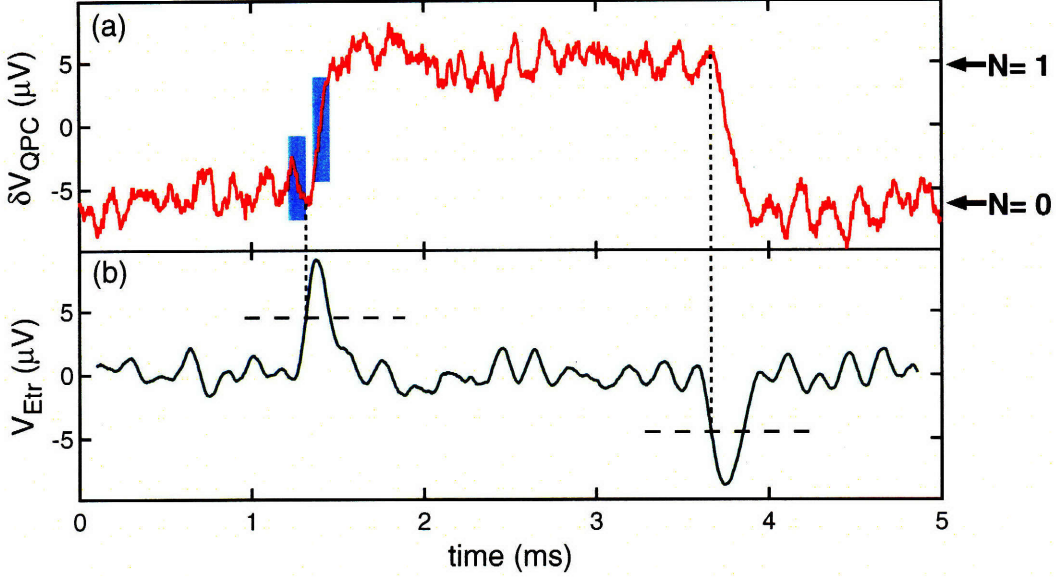
Figure 3-6: (a) Real-time data trace. The shaded rectangles show the two time periods that are averaged and then subtracted to give the value of V_{Etr} at time $t \approx 1.3$ ms, which is marked by a dotted vertical line. (b) Value of V_{Etr} as a function of time for the data in (a). The edge trigger records an electron tunneling event at the time when $|V_{Etr}|$ exceeds a threshold V_{edge}. The dashed horizontal lines mark the threshold while the dotted vertical lines mark the two times when $|V_{Etr}|$ passes threshold.

noise, we cannot simply take the difference of consecutive points. Instead, the edge trigger works by taking the difference between the average voltage at two different times, a quantity that we call $V_{Etr}(t)$. Specifically, to find $V_{Etr}(t)$ we average the data from $t - 100$ μs to t and from $t + 40$ μs to $t + 40 + 100$ μs and then subtract these two averages. Formally,

$$V_{Etr}(t) = \frac{1}{t_{ave}} \int_{t+t_{skip}}^{t+t_{skip}+t_{ave}} V_{QPC}(t) \, dt - \frac{1}{t_{ave}} \int_{t-t_{ave}}^{t} V_{QPC}(t) \, dt \qquad (3.2)$$

where $t_{ave} = 100$ μs is the time over which we average and $t_{skip} = 40$ μs is the time we skip between the regions we average. We choose the value of t_{skip} to be approximately the rise-time of the charge detection circuit. Figure 3-6(b) shows $V_{Etr}(t)$ for the data trace in Fig. 3-6(a). The edge trigger records an electron tunneling event at the time when $|V_{Etr}|$ exceeds a specified threshold V_{edge}; the sign of V_{Etr} tells us whether an

electron is tunneling onto the dot ($V_{Etr} > 0$) or off of the dot ($V_{Etr} < 0$). This is illustrated in Fig. 3-6(b), where the dashed horizontal lines mark the the threshold and the dotted vertical lines mark the two times when $|V_{Etr}|$ passes the threshold. The edge trigger automatically reduces the 2500 data points in this trace down to the 4 pieces of information that are recorded (the times and directions of the two charge transitions).

Since the edge trigger plays a large role in data collection, it is important to characterize this trigger. To do this, we create artificial charge transitions by pulsing the voltage on gate LP2. The capacitance between LP2 and the QPC causes R_{QPC} to change in response to the voltage pulse, and by properly choosing the size of the voltage pulse we can generate a QPC response that is the same size as that of a charge transition on the dot. The time-constant for the pulses ($\approx 3 \ \mu s$) is much faster than the time constant for the QPC charge detector, so the shape of the artificial signals are like those for electrons. An example of an artificial signal is shown in the inset to Fig. 3-7(b) and it closely approximates an electron tunneling onto and then off of a dot. The advantage with the artificial signals is that we know precisely when they occur.

To characterize the edge trigger, we analyze 400 artificial charge transitions. To check the accuracy of the edge trigger, we look at a 2 ms window around an artificial charge transition and check that the the edge trigger identifies precisely one charge transition during this period and that it correctly identifies the direction of the transition. We repeat this for different values of V_{edge} and the results are plotted in Fig. 3-7(a) as a function of $V_{edge}/|V_s|$, where $|V_s| \approx 11.5 \ \mu V$ is the size of the artificial signals. For $V_{edge}/|V_s| \lesssim 0.25$ the edge trigger is inaccurate because the threshold is too low and so it triggers on the noise and finds multiple electron tunneling events. For $V_{edge}/|V_s| \gtrsim 0.65$ the accuracy decreases because the threshold is so high that the trigger starts to miss charge transitions. However, in the intermediate range, we see that the trigger is very accurate, and for most experiments we typically have $V_{edge}/|V_s| \approx 0.4$.

We also measure the accuracy with which the edge trigger identifies the time of
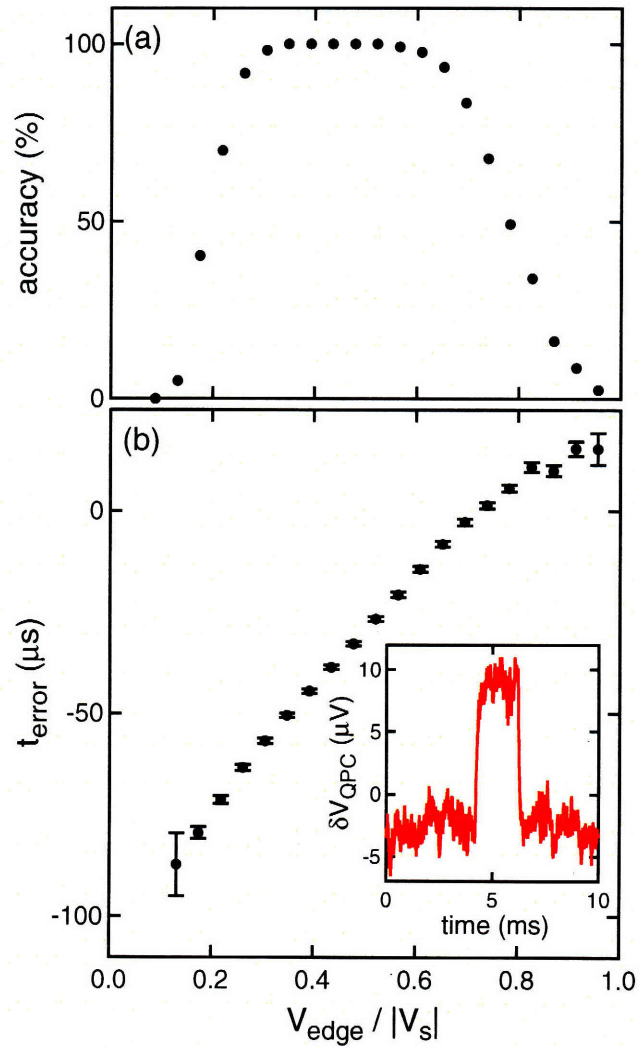
Figure 3-7: (a) The accuracy and (b) average offset t_{error} of the edge trigger as a function of the ratio of V_{edge} to the signal size $|V_s|$ for 400 artificial signals. The inset in (b) shows an example of an artificial signal generated by applying a voltage pulse to gate LP2.
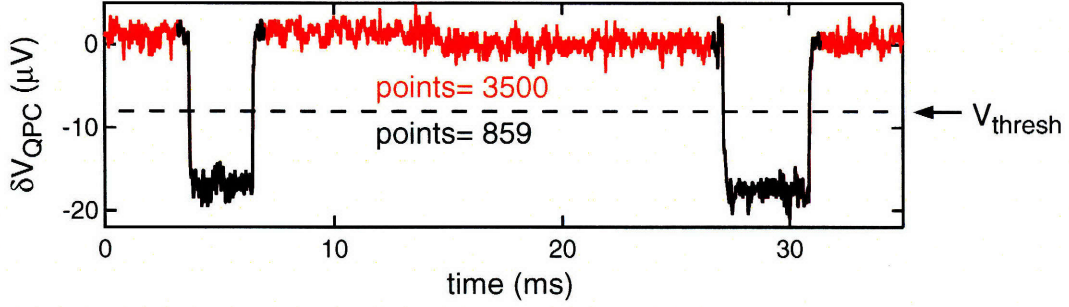
Figure 3-8: The threshold trigger saves all data points that pass below a specified threshold V_{thresh}, as well as 500 μs to either side in order to capture the transitions.

the charge transition. We define $t_{error} = t_{edge} - t_{pulse}$ where t_{edge} is the time at which the artificial charge transition occurs as determined by the edge trigger, and t_{pulse} is the actual time. The average values of t_{error} are plotted in Fig. 3-7(b) and we see there is a systematic offset that depends on $V_{edge}/|V_s|$. For $V_{edge}/|V_s| \approx 0.4$ we have $t_{error} \approx -45$ μs.

One drawback to the edge trigger is that it is calculation intensive, so depending on the digitization rate we can spend up to an equal amount of time analyzing data as acquiring data. For some data, we can use another trigger to speed up the analysis process. For example, in the data in Fig. 3-8 the dot is mostly in the $N = 1$ state, but occasionally the electron tunnels off the dot and then back on a short time later. Instead of analyzing the entire trace with the edge trigger, we first apply a threshold trigger. The threshold trigger saves only the data points for which $V_{QPC}(t) < V_{thresh}$, as well as 500 μs around these points in order to capture the edges of the transitions. The points saved by the threshold trigger are shown in black in Fig. 3-8 and we see that this trigger reduces the number of points to be analyzed from 3500 to 859. We analyze the output of the threshold trigger with the edge trigger to identify the charge transitions. Using the threshold and edge triggers in sequence can reduce the analysis time by a factor of 2 to 4.

In summary, the edge and threshold triggers allow us to reduce the amount of data we need to save by ~ 1000. This makes it possible to take data over long periods of time and acquire good statistics. As we acquire data, we randomly save data traces

54

and use these for diagnostic purposes. Much of the real-time data shown in this thesis are from such randomly saved traces.

Chapter 4

Tunneling in Quantum Dots

The rate at which an electron can tunnel between the quantum dot and the leads is an important parameter in determining the mechanism that dominates the spin physics of an electron confined in the dot. When the tunneling rates are very fast, the dot is in the Kondo regime where the spin of an electron on the dot forms virtual singlets with the spins of electrons in the leads [12, 13]. When the tunneling rates are very slow, the spin of a confined electron interacts with nuclear spins via the hyperfine interaction [37, 38, 39, 41, 34, 40] and with phonons via the spin-orbit interaction [28, 93], leading to spin decoherence and relaxation, respectively. Tunneling is also essential to potential applications for quantum dots in spintronics, such as spin filtering [24, 25].

In this chapter we use our real-time charge sensing techniques to explore electron tunneling in greater detail. The first section discusses how we measure the occupation probability of the dot and the rates at which an electron tunnels into or out of the dot. The second section describes how we use measurements of the tunneling rates to implement a novel active feedback system to maintain the stability of the dot. In the third section we describe experiments investigating the energy dependence of tunneling in a quantum dot. These results are reported in MacLean *et al.* [80]. In the final section we discuss our observations of spin dependent tunneling in a magnetic field, which are reported in Amasha *et al.* [94].

4.1 Measuring the occupation probability and tunneling rates

Before considering tunneling rates, we discuss a closely related quantity called the occupation probability P_{on}, which is the probability that there is an electron on the quantum dot. We expect P_{on} to depend on the energies of the states of the dot relative to the Fermi energy of the leads. We can simplify the situation by adjusting the gate voltages so that the tunneling rate through the barrier defined by gates SG2 and OG (which we call $b2$) is much greater than that through the barrier defined by the gates SG1 and OG (which we call $b1$). With the gate voltages set in this way, we have a quantum dot coupled to only one lead, as illustrated in Fig. 4-1(a). When the energy of the ground state of the dot is above the Fermi energy of the lead ($E > 0$), we expect that P_{on} is small. Figure 4-1(b) shows an example of real-time data with $E > 0$; as we expect the dot is unoccupied the majority of the time. As we lower the energy of the ground state by making the voltage on gate LP2 less negative, P_{on} increases until $P_{on} \sim 0.5$ at $E \sim 0$ (Fig. 4-1(c)). Finally, when the energy of the ground state is well below the Fermi energy, the dot is mostly occupied, and the electron tunnels off only occasionally (Fig. 4-1(d)).

We can quantify the dependence of P_{on} on the energy of the ground state of the dot. Using the triggering system discussed in Section 3.3 we identify when an electron tunnels onto or off of the dot. From these data, we determine the time intervals[1] t_{on} and t_{off} during which the dot is occupied or unoccupied, respectively, as shown in Fig. 4-1(c). Then we have

$$P_{on} = \frac{T_{on}}{T_{on} + T_{off}} = \frac{\tau_{on}}{\tau_{on} + \tau_{off}} \tag{4.1}$$

where T_{on} is the total time the dot is occupied and this is found by summing the measurements of t_{on}. T_{off} is the total time the dot is unoccupied, and is determined in a similar manner. τ_{on} and τ_{off} are the average times that the dot is occupied or

---

[1]Note that t_{on} and t_{off} are determined by subtracting the times at which charge transitions occur, so the systematic error t_{error} in the measurement of the transition time should cancel.
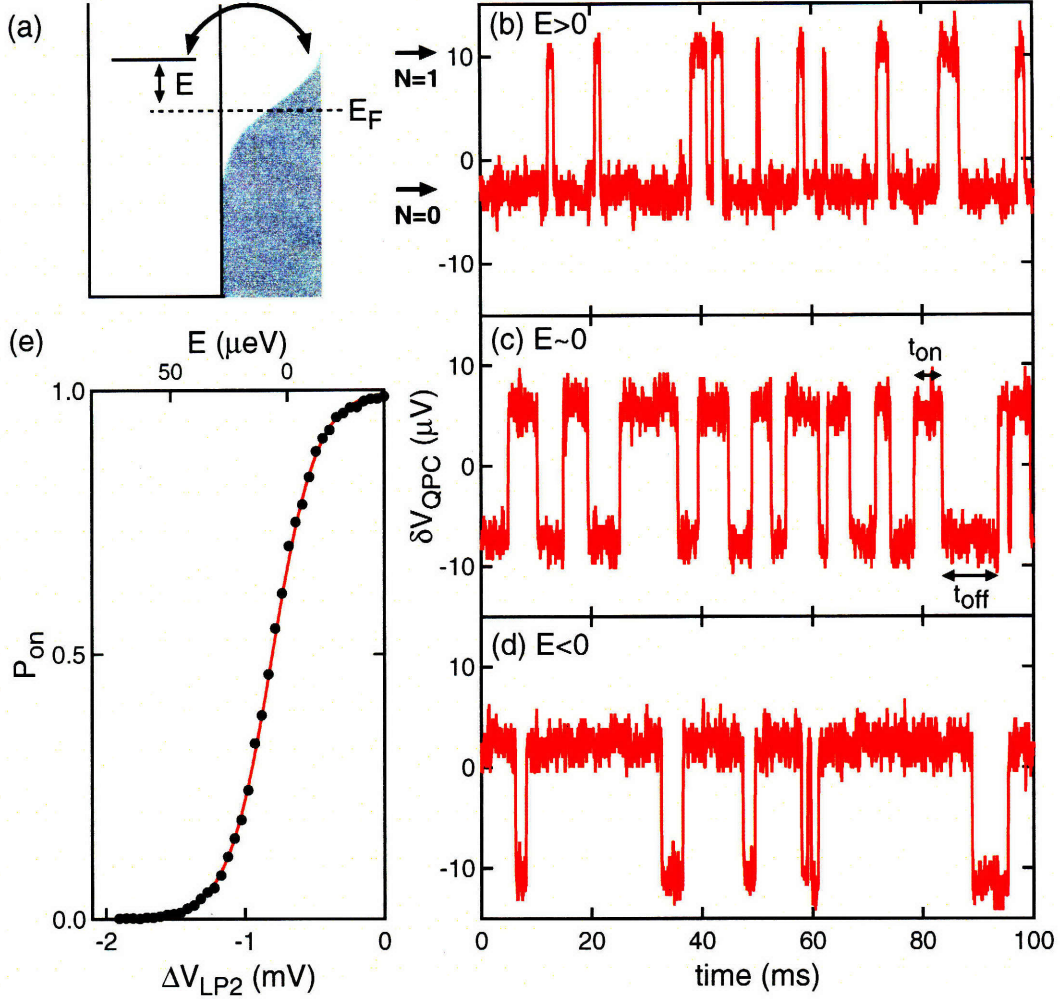
Figure 4-1: (a) Diagram showing a single-electron quantum dot coupled to one lead. E is the energy of the ground state relative to the Fermi energy E_F of the lead. (b)-(d) Real-time data when the ground state is above, near, and below the Fermi energy, respectively. The voltages on the QPC that correspond to the dot being occupied ($N = 1$) and unoccupied ($N = 0$) by an electron are indicated in (b). Examples of t_{on} and t_{off} are illustrated in (c). (e) Occupation probability P_{on} as a function of gate voltage (bottom axis) and E (top axis). The solid line is a fit discussed in the text.

unoccupied, respectively. Figure 4-1(e) shows an example of P_{on} as a function of gate voltage. As we expect, P_{on} is small at more negative gate voltages where the ground state is above the Fermi energy and increases as LP2 is made less negative.

We quantitatively understand the shape of P_{on} using thermodynamic consider-

59

ations. For a dot with one orbital state[2], there are four possibilities for the dot occupation: the dot can be empty, it can contain one electron in either the spin-up or spin-down states, and it can contain two electrons. The partition function for this system is

$$Z = 1 + 2e^{-\beta(\epsilon-\mu)} + e^{-\beta(2\epsilon+U-2\mu)}$$

where $\beta = 1/k_B T$, ϵ is the energy of the ground state relative to the bottom of the conduction band, $\mu = E_F$ is the Fermi energy of the lead, and U is the charging energy associated with having two electrons on the dot. The average number of electrons on the dot $\overline{N}_{dot}$ is given by $\overline{N}_{dot} = -\frac{\partial}{\partial\mu}(-k_B T \ln Z)$. Since $U \approx 4\text{meV} > k_B T$, we take the limit of infinite U and find $\overline{N}_{dot} = (1+\frac{1}{2}e^{\beta(\epsilon-E_F)})^{-1}$. But $\overline{N}_{dot} = 0 \times P_{off} + 1 \times P_{on} = P_{on}$, so we have

$$P_{on} = (1 + (1/2)e^{E/k_B T})^{-1} \tag{4.2}$$

where $E = \epsilon - E_F$. Essentially, P_{on} is a shifted Fermi function $P_{on} = f(E - k_B T \ln 2)$ where $f(x) = (1 + e^{x/k_B T})^{-1}$.

The energy of the ground state is related to the gate voltage by $E = -e\alpha_{LP2}\Delta V_{LP2} + E_0$, where E_0 is the energy corresponding to $\Delta V_{LP2} = 0$ and $\alpha_{LP2} = 0.06$ is measured from a noise diamond obtained by slightly adjusting the gate voltages to allow transport through $b1$. The solid line in Fig. 4-1(e) shows a fit of the data to Eqn. 4.2, and from this fit we extract a temperature of $T = 110$ mK.

The occupation probabilities are related to the tunneling rates by the equation[3]

$$\dot{P}_{on} = \Gamma_{on} P_{off} - \Gamma_{off} P_{on} \tag{4.3}$$

where $P_{off} = 1 - P_{on}$. If the dot is empty at $t = 0$, we can use this equation to find the probability distribution $\mathcal{P}_{off}$ that the dot will remain empty until time $t = t_{off}$, at which time an electron tunnels onto the dot. Given that the dot is empty, the probability that an electron will tunnel on during a short time interval Δt is

---

[2]We can safely neglect the excited orbital states because their energies are much greater than $k_B T$.

[3]We assume that at zero magnetic field the tunneling rates into the two spin states of the dot are equal.
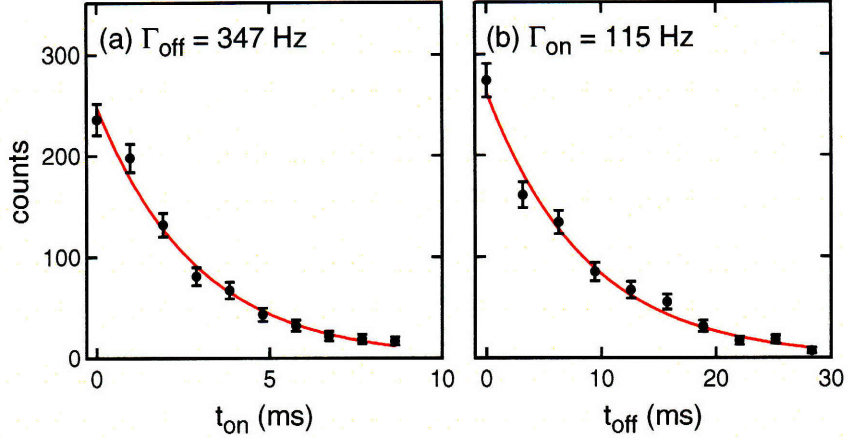
Figure 4-2: Histograms of (a) the on-times t_{on} and (b) the off-times t_{off} for real-time data. The solid lines are fits to determine the tunneling rates as discussed in the text.

given by Eqn. 4.3: $\Delta P_{on} = \dot{P}_{on}\Delta t = \Delta t(\Gamma_{on}P_{off} - \Gamma_{off}P_{on}) = \Gamma_{on}\Delta t$. In this last equality we use the fact that $P_{off} = 1$ and $P_{on} = 0$ initially. Since the probability for tunneling on is $\Gamma_{on}\Delta t$, the probability that the electron does not tunnel on is $(1 - \Gamma_{on}\Delta t)$. If we divide the time interval between $t = 0$ and t_{off} into N segments of length $\Delta t = t_{off}/N$, then the probability of tunneling onto the dot between t_{off} and $t_{off} + \Delta t$ is given by $\mathcal{P}_{off}(t_{off})\Delta t = (1 - \Gamma_{on}\Delta t)^N(\Gamma_{on}\Delta t)$, where $(1 - \Gamma_{on}\Delta t)^N$ is the probability that the electron *does not* tunnel onto the dot in the N segments before t_{off} and $(\Gamma_{on}\Delta t)$ is the probability of tunneling on between t_{off} and $t_{off} + \Delta t$. Then $\mathcal{P}_{off}(t_{off}) = \Gamma_{on}(1 - \Gamma_{on}t_{off}/N)^N$ and taking the limit as $N \to \infty$ gives

$$\mathcal{P}_{off}(t_{off}) = \Gamma_{on}e^{-\Gamma_{on}t_{off}}. \tag{4.4}$$

We can similarly show that

$$\mathcal{P}_{on}(t_{on}) = \Gamma_{off}e^{-\Gamma_{off}t_{on}}. \tag{4.5}$$

Thus we see that measurements of t_{on} determine Γ_{off}, and vice-versa. Note that from the probability distributions, the average off and on times are related to the rates by $\tau_{off} = \Gamma_{on}^{-1}$ and $\tau_{on} = \Gamma_{off}^{-1}$.

To find the tunneling rates, we histogram the measurements of t_{on} and t_{off} at a fixed set of gate voltages as shown in Fig. 4-2. By fitting these histograms to exponentials (solid lines in Fig. 4-2), we extract the tunneling rates Γ_{on} and Γ_{off} as shown.

From Eqn. 4.3 we derive a relationship between Γ_{off} and Γ_{on}. In steady state $\dot{P}_{on} = 0$ and

$$P_{on} = (1 + \Gamma_{off}/\Gamma_{on})^{-1} \tag{4.6}$$

Comparing this equation to Eqn. 4.2. we see that [83]

$$\Gamma_{off}/\Gamma_{on} = (1/2)e^{E/k_B T} \tag{4.7}$$

If we assume that tunneling is elastic, a sensible model for Γ_{off} is $\Gamma_{off} = \Gamma(1 - f(E))$ where Γ is the bare tunneling rate through the barrier and $(1 - f(E))$ is the density of hole states in the leads [77, 78, 83]. Then from Eqn. 4.7. we have $\Gamma_{on} = 2\Gamma f(E)$, which is the result we expect for electrons tunneling into the two spin states of an empty dot.

4.2 Active feedback control

For the experiments that are discussed in the following sections and chapters, we need to control the energies of the states of the dot relative to the Fermi energy and to keep these states stable. For some experiments this control is necessary because we want to study the tunneling rates when the states are at a particular energy relative to the Fermi energy of the leads. in other experiments, we position one of the states a certain energy above or below the Fermi energy and observe whether an electron tunnels onto or off of the dot, and this gives us information about whether this state is occupied. Also, we need the states to be stable to acquire good statistics.

Unfortunately, as has been noted in previous work [36]. the energies of the states in lateral quantum dots tend to shift over time because of background charge fluctuations in the heterostructure [72]. In general, these fluctuations do not change the energies

of the states relative to one another (for example, the energies of the excited states relative to the ground state remain constant); rather, the charge fluctuations tend to act like changes in gate voltage and shift the energies of all the states together. Although our heterostructure is relatively stable in this regard, we still observe two types of shifts: a slow drift of the energies of the states over time and sudden, large shifts in the energies.

To compensate for these shifts, we use a novel active feedback control system to position and to maintain the stability of the states of the dot. The feedback system uses measurements of the tunneling rate out of the ground state of the dot, which is given by $\Gamma_{off} = \Gamma(1 - f(E))$. When this state is below the Fermi energy of the lead $(E \lesssim -k_B T)$, $\Gamma_{off} \approx \Gamma e^{E/k_B T}$, so that Γ_{off} is exponentially sensitive[1] to the energy E of the ground state relative to the Fermi energy, as illustrated in Fig. 4-3(a).

The feedback system takes advantage of the exponential sensitivity of Γ_{off}. The data acquisition computer regularly measures Γ_{off} by monitoring the dot for a period of time t_f and counting the number of times N that an electron tunnels off the dot as shown in Figs. 4-3(b) and (c); Γ_{off} is then given by $\Gamma_{off} = N/t_f$. A desired set point E_{set} corresponds to a tunneling rate Γ_{set} (Fig. 4-3(a)), and if $E \approx E_{set}$ then $\Gamma_{off} \approx \Gamma_{set}$ as shown in Fig. 4-3(b). We typically choose E_{set} so that $\Gamma_{set} \approx 10$ Hz. However, if the energies of the states of the dot shift, for example if $E < E_{set}$ as in Fig. 4-3(c), then $\Gamma_{off} < \Gamma_{set}$ and the data acquisition computer automatically adjusts the voltage on gate LP2 to change E until $\Gamma_{off} \approx \Gamma_{set}$.

To determine whether Γ_{off} is sufficiently close to Γ_{set}, we test if $|\Gamma_{off} - \Gamma_{set}| < \Gamma_{tol}$, where Γ_{tol} is a tolerance that we typically choose to be between 1 and 5 Hz, depending on the precision with which we need to control the levels. The choice of Γ_{tol} affects the time needed to monitor the dot t_f: the smaller the tolerance, the longer t_f needs to be in order to make a sufficiently accurate measurement of Γ_{off}. We quantify this relationship as follows. We have $\Gamma_{off} = N/t_f$, and from counting statistics we know that the error in a count N is given by $N^{1/2}$. So the error in our measurement of Γ_{off}

---

[1]For a few data sets, the feedback system uses measurements of the tunneling rate onto the dot when $E > k_B T$. In this case $\Gamma_{on} = 2\Gamma f(E) \approx 2\Gamma e^{-E/k_B T}$ and so we are also exponentially sensitive to the dot energy.
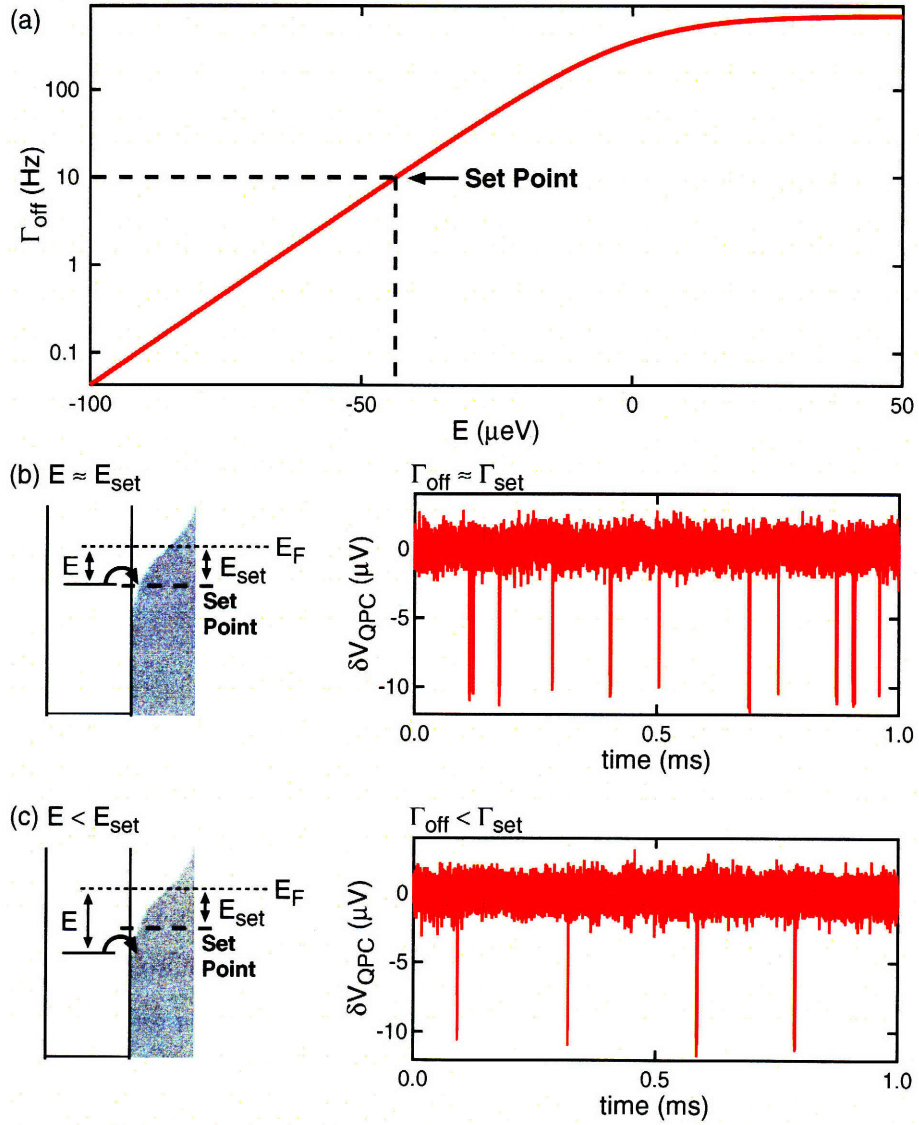
Figure 4-3: (a) An example of $\Gamma_{off} = \Gamma(1 - f(E))$ as a function of E for $\Gamma = 700$ Hz and $T = 120$ mK. For $E < -k_B T \approx -10$ μeV, Γ_{off} is exponentially sensitive to E. The dashed vertical line shows a typical energy that we choose for a set point E_{set}; the dashed horizontal line shows the corresponding value of Γ_{set}. (b) and (c) Real-time data and the corresponding dot energy diagrams. Since the energy of the ground state is below the Fermi energy E_F, the electron tunnels off only occasionally because of the small density of hole states in the leads. The dot does not remain empty for long, however, because there are many filled electron states in the leads, so an electron quickly tunnels back onto the dot (on a timescale of Γ^{-1}). Therefore each tunneling event appears as a sharp spike, and the computer can easily count the number of events in a given time to determine Γ_{off}.

64

is $\delta\Gamma = N^{1/2}/t_f$. If $\Gamma_{off} = \Gamma_{set}$ then the expected value of $N = \Gamma_{set}t_f$ and the error in the measured rate is $\delta\Gamma = (\Gamma_{set}/t_f)^{1/2}$. We need to set the tolerance to be larger than this expected error, so we have $\Gamma_{tol} \geq (\Gamma_{set}/t_f)^{1/2}$, which then implies

$$t_f \geq \frac{\Gamma_{set}}{\Gamma_{tol}^2} \tag{4.8}$$

While the feedback system makes possible many of the measurements reported in this thesis, it also adds to the time we are not acquiring data. We usually choose t_f to be between 5 and 10 s, and the amount of time spent in the feedback sequence ranges from 25%-50% of the total aquisition time. A number of improvements could decrease the amount of time spent in the feedback sequence. First, the time it takes to analyze the feedback data is about 50% of t_f. This can be improved by reducing the time resolution of the data during t_f, as we are not concerned about the times at which electron tunneling events occur. Also, it may be possible to implement multi-threading so that the triggers analyze the data aquired as part of the experiment in parallel with the collection of data for the feedback step (currently, data collection and analysis occurs serially).

4.3 Energy-dependent tunneling in a quantum dot

4.3.1 Introduction

In this section, we use real-time charge sensing and gate pulsing techniques to study electron tunneling in a single electron quantum dot. We observe that the rates for tunneling onto and off of the dot, Γ_{on} and Γ_{off} respectively, are exponentially sensitive to V_{ds} and V_g. We show that this exponential dependence of the tunneling rates is in excellent quantitative agreement with a model that assumes elastic tunneling and accounts for the effect on tunneling of the energies of the states of the dot relative to the heights of the tunnel barriers connecting the dot to its leads.

4.3.2 Tunneling as a function of drain-source bias

Using our real-time charge sensing techniques, we characterize how the tunneling rates Γ_{on} and Γ_{off} change as a function of the bias voltage V_{ds} between leads 1 and 2. These data are shown in Fig. 4-4(a). From the data, we see that Γ_{off} increases exponentially as V_{ds} is made more negative. In contrast, as V_{ds} is made more negative Γ_{on} increases rapidly at two specific values of V_{ds} (marked by e_1 and e_2 in the bottom panel of Fig. 4-4(a)). But between these points Γ_{on} decreases as V_{ds} is made more negative.

The increases in Γ_{on} at e_1 and e_2 are because of the excited states of the dot. For negative V_{ds}, the Fermi energy of lead 1 is greater than that of lead 2, so electrons tunnel onto the dot through $b1$ and then tunnel off the dot through $b2$. The increases in Γ_{on} occur when the Fermi energy of lead 1 is aligned with the energy of one of the excited orbital states of the dot, as illustrated by the diagram in Fig. 4-4(b). Γ_{on} increases rapidly because the excited orbital states are more strongly coupled to the leads than the ground state. From the values of V_{ds} at which Γ_{on} increases, we estimate the energies of the excited states using α_{ds} measured from noise diamonds and other techniques. We obtain 1.9 and 2.9 meV, which are close to the energies of the excited states obtained from differential conductance measurements made with larger tunneling rates, shown in Fig. 4-4(c). The increases in Γ_{on} do not correspond to sharp changes in Γ_{off} because after the electron tunnels into an excited orbital state, it relaxes to the ground orbital state before it can tunnel off the dot (the relaxation timescale of $\lesssim 10$ ns [95, 96, 80] is much shorter than the timescale for tunneling). Once in the ground orbital state the electron tunnels off the dot through $b2$.

What remains to be understood is why Γ_{off} increases exponentially as V_{ds} is made more negative, while Γ_{on} decreases. From quantum mechanics, we know that the transmission of an electron through a potential barrier depends on the energy of the electron relative to the height of the barrier [97, 98]. In the semi-classical limit[5],

---

[5]To be in the semi-classical limit in the barrier, the inverse wavevector of the electron in the barrier must be much less than the length scale over which the potential varies [98]. *A priori*, it is not clear that we satisfy this condition. But the semi-classical picture provides motivation for expecting an exponential dependence of the tunneling rates on V_{ds}, which we do observe.
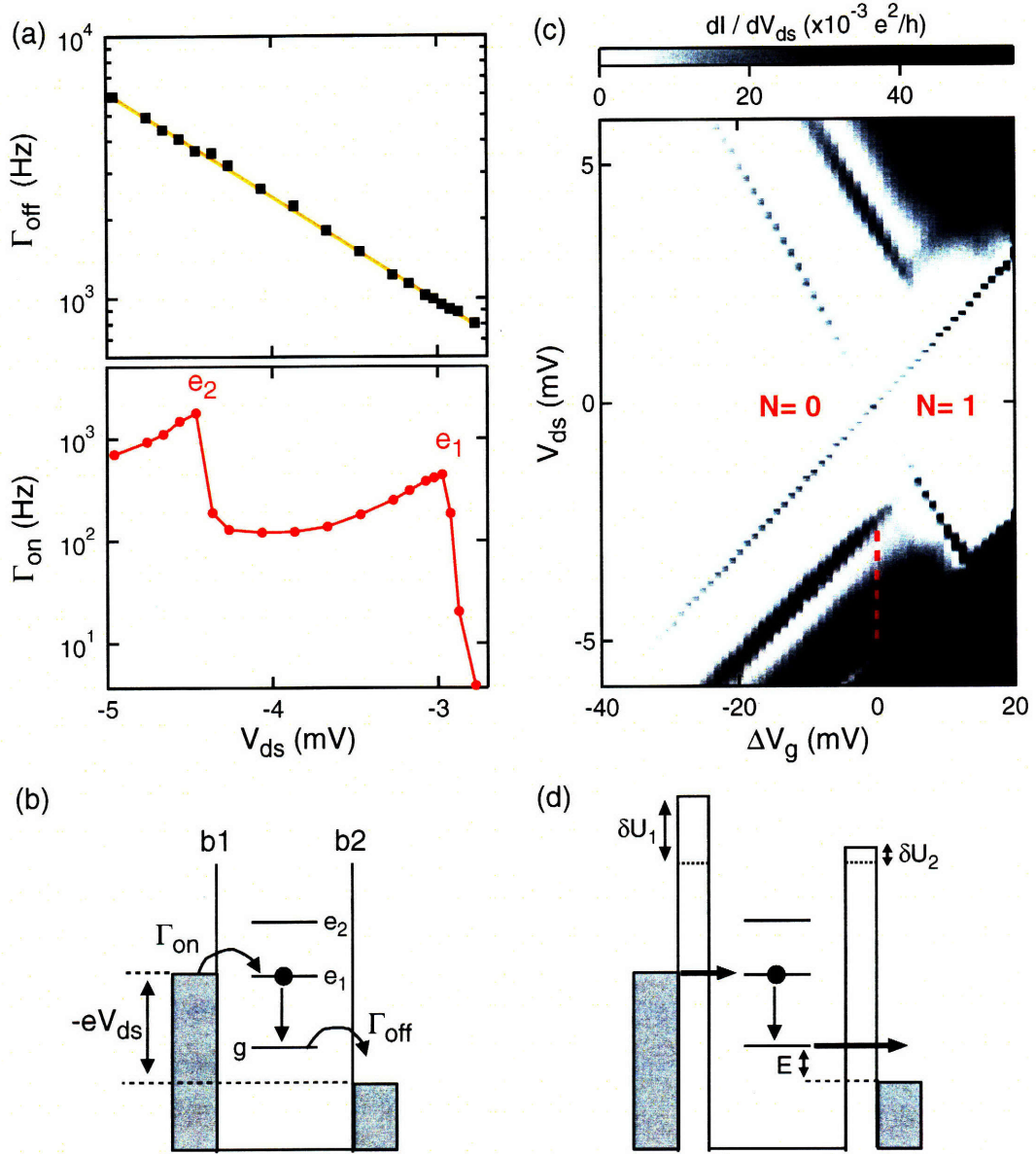
Figure 4-4: (a) Tunneling rates as a function of V_{ds} measured using real-time charge sensing techniques. The solid line in the top panel is a fit described in the text. (b) Dot diagram showing the energies of the states of the dot relative to the energies of the electrons in lead 1 (drain lead) and lead 2 (source lead). The ground orbital state is denoted g while $e1$ and $e2$ denote the two excited orbital states. (c) Differential conductance as a function of V_{ds} and ΔV_g measured with the tunneling rates large enough to use transport techniques. The vertical dashed line marks the region we measure using real-time techniques and slower tunneling rates. (d) Dot diagram showing the change in the energies of the states of the dot $\delta\epsilon = E$ and the heights of the tunnel barriers δU_1 and δU_2 caused by the bias voltage.

the transmission through a potential barrier is proportional to

$$\exp\left[-2\int\sqrt{\frac{2m}{\hbar^2}(U(x)-\epsilon)}\;dx\right]$$

where $U(x)$ is the height of the barrier and ϵ is the energy of the tunneling electron, both of which are measured from the bottom of the conduction band. We assume that tunneling is elastic, so that ϵ is also the energy of the state on the dot into which the electron is tunneling. For small perturbations to the energy of this state $\delta\epsilon$ and the potential barrier δU, we linearize the above expression and obtain $\Gamma = \Gamma_0\exp[-\kappa(\delta U - \delta\epsilon)]$, where κ and Γ_0 depend on the details of the barrier and the dot.

Applying a drain-source bias V_{ds} has the effect of varying the energies of the states in the dot; in a linear capacitance model this variation is given by $\delta\epsilon = E = -e\alpha_{ds}V_{ds}$. Similarly, we expect V_{ds} to affect the two barriers. The linear capacitance model gives $\delta U_1 = -e\alpha_{U1.ds}V_{ds}$, where $\alpha_{U1.ds}$ describes the coupling of V_{ds} to $b1$, and we have a similar dependence for δU_2.

The relative values of $\alpha_{U1.ds}$, α_{ds}, and $\alpha_{U2.ds}$ depend on geometry [99]: because lead 1 is closer to $b1$ than it is to the dot, we expect that $\alpha_{U1,ds} > \alpha_{ds}$. Similarly, lead 1 is closer to the dot than it is to $b2$, so we expect that $\alpha_{ds} > \alpha_{U2.ds}$. Thus for negative V_{ds}, we expect that $\delta U_1 > E > \delta U_2$, as illustrated in Fig. 4-4(d). Then the effect of the bias is to increase the height of $b1$ relative to the energies of the states of the dot, which then decreases the rate at which the electrons tunnel onto the dot. This explains why Γ_{on} decreases with more negative V_{ds} between the rapid increases in Fig. 4-4(a). The bias also increases the energies of the states more that it increases the height of $b2$, and this brings the states closer to the top of $b2$. This results in an increase in the rate at which electrons tunnel off the dot. For tunneling out of the ground state, we describe this quantitatively by

$$\Gamma_{off} = \Gamma_2 e^{-\beta_2 V_{ds}} \tag{4.9}$$

where Γ_2 describes the rate through $b2$ at $V_{ds} = 0$ and $\beta_2 = \kappa_2|\alpha_{U2.ds} - \alpha_{ds}|$. The solid

68
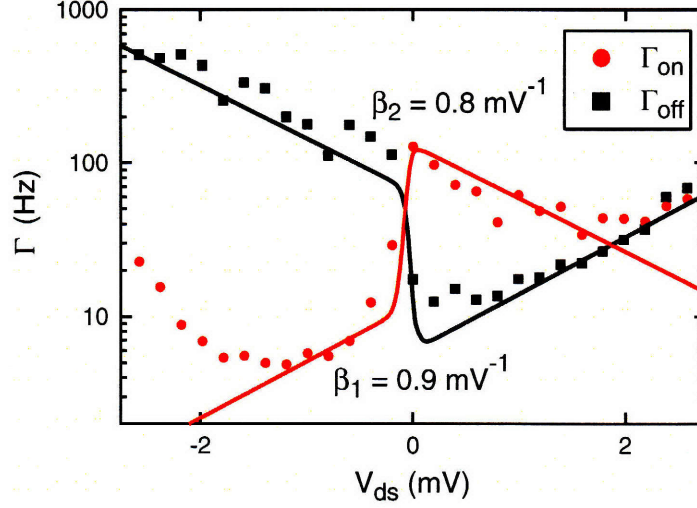
Figure 4-5: Tunneling rates through the dot as a function of V_{ds}. Near $V_{ds} = 0$ electrons can tunnel on and off the dot through both leads. The solid lines are calculations discussed in the text.

line in Fig. 4-4(a) shows a fit to this equation, from which we obtain $\beta_2 = 0.9$ mV^{-1}.

The data in Fig. 4-4(a) is for $V_{ds} \gg 0$, where electrons tunnel on through $b1$ and off through $b2$. We also study electron tunneling closer to $V_{ds} = 0$, as shown in Fig. 4-5. Near $V_{ds} = 0$, electrons can tunnel on and off the dot through both barriers, and the tunneling rates depend on the Fermi statistics in the leads. We extend Eqn. 4.9 to include these effects. For tunneling through the ground state of the dot, we have

$$\Gamma_{off} = \Gamma_2 e^{-\beta_2 V_{ds}}[1 - f_2(E)] + \Gamma_1 e^{\beta_1 V_{ds}}[1 - f_1(E)] \tag{4.10}$$

and

$$\Gamma_{on} = \eta \Gamma_2 e^{-\beta_2 V_{ds}} f_2(E) + \eta \Gamma_1 e^{\beta_1 V_{ds}} f_1(E). \tag{4.11}$$

In these equations $E = -e\alpha_{ds}V_{ds}$ is the energy of the ground state relative to the Fermi energy in lead 2, and f_1 and f_2 are the Fermi functions of the leads $f_1(E) = f(E + eV_{ds})$ and $f_2(E) = f(E)$. Also, η is the ratio of the on and off rates for a given lead, so from Eqn. 4.7 we expect $\eta = 2$ from spin degeneracy [100, 54], and we use this value for the rest of this section.

The solid lines in Fig. 4-5 show Eqns. 4.10 and 4.11 with $\beta_1 = 0.9 \text{ mV}^{-1}$. $\Gamma_1 = 6$ Hz. $\beta_2 = 0.8 \text{ mV}^{-1}$, and $\Gamma_2 = 65$ Hz. At negative V_{ds}, electrons tunnel onto the ground state through $b1$ and off through $b2$, whereas at positive V_{ds}, electrons tunnel off through $b1$ and on through $b2$. While there is good agreement between the calculation and Γ_{off} over the whole range, at large positive and negative values of V_{ds} we see that Γ_{on} deviates from the calculation. This deviation is because of the excited states. and a lineshape that includes the excited states can be calculated and gives good agreement with the data (see MacLean et al. [80] for details).

4.3.3 Tunneling as a function of gate voltage

We also characterize the dependence of the tunneling rates on changes in the gate voltages ΔV_g applied to the three gates LP1, PL, and LP2. For these measurements, the barriers are tuned so that the tunneling rate Γ_1 through $b1$ is negligible compared to that through $b2$ (the same situation described in Section 4.1). The energy of the ground state relative to the Fermi energy is given by $E = -e\alpha_g \Delta V_g$. When $E \sim 0$, electrons can tunnel on and off the dot. and we can measure both rates with our real-time charge detection techniques. However, for $E \ll 0$ and $E \gg 0$, Γ_{off} and Γ_{on} are negligibly small. respectively. For these values of E, spontaneous tunneling events are rare and we have to measure the rates using pulse techniques.

The diagrams in Figs. 4-6(a) and (b) show the position of the ground state of the dot during the pulse sequence we use to measure Γ_{off} for $E \gg 0$. The top panel in Fig. 4-6(c) shows the change in the energy of the ground state during each step. First we apply a voltage pulse to gate LP2 to bring the energy of the ground state down to the Fermi energy, and hold it at this energy for a time $t_H \approx 0.6$ ms. During this time an electron can tunnel onto the dot. After t_H, we bring the state back to its original energy and observe the electron tunneling out of the dot. The bottom panel of Fig. 4-6(c) shows an example of real-time data taken during the pulse sequence. Using our triggering system. we measure the time t_{on} between the end of the charging pulse and when the electron tunnels off the dot. We then fit a histogram of the values of t_{on} to an exponential to extract Γ_{off}. To measure Γ_{on} when $E \ll 0$, we use a
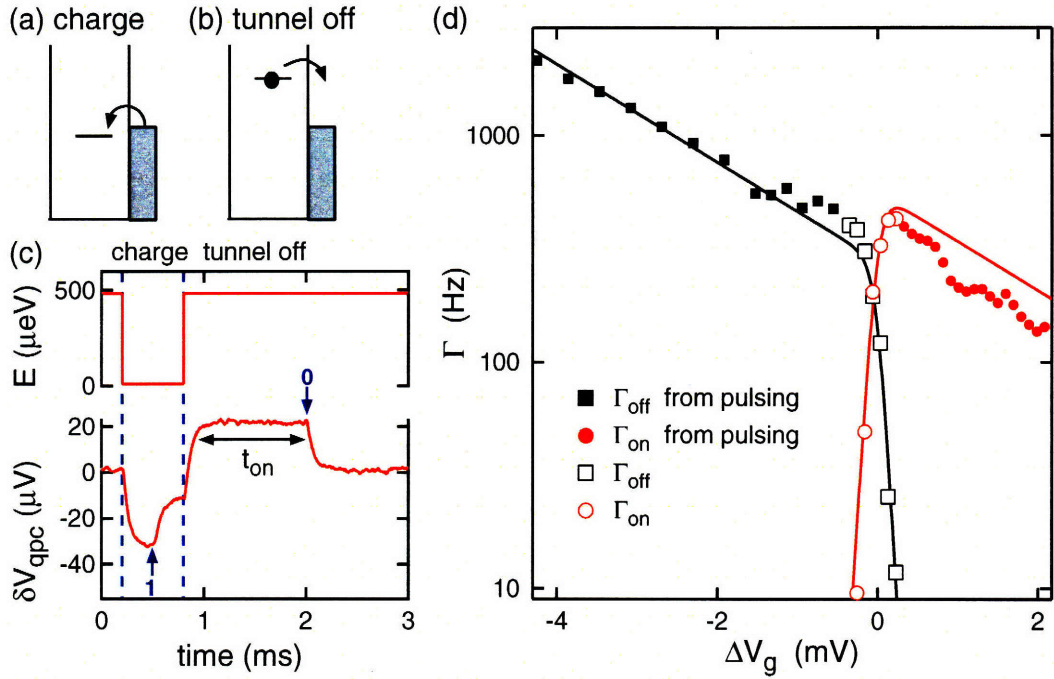
Figure 4-6: (a) and (b) are dot diagrams illustrating the position of the ground state of the dot during the two steps of the pulse sequence. The top panel of (c) shows the energy of the state during the two steps, while the bottom panel shows an example of real-time data. The direct capacitive coupling between LP2 and the QPC causes the QPC to respond to the pulse sequence; electron tunneling events are evident on top of this response. The 0's denote when an electron tunnels off the dot, while 1's denote when an electron tunnels on. Using our triggering system, we automatically measure the time t_{on} between the end of the pulse sequence and when and electron tunnels off the dot. (d) Tunneling rates as a function of ΔV_g. Near $\Delta V_g = 0$ the rates are measured by observing spontaneous tunneling. Away from $\Delta V_g = 0$, one of the rates is negligibly small and we use a pulse sequence to measure the other rate.

similar sequence where we pulse the gate to empty the dot and then measure the time it takes for an electron to tunnel onto the dot.

Measurements of the tunneling rates as a function of ΔV_g are shown in Fig. 4-6(d). Near $\Delta V_g = 0$, Γ_{off} decreases rapidly with increasing ΔV_g and Γ_{on} increases because of Fermi statistics. Away from this region, however, we see that the rates generally decrease with increasing ΔV_g. We can understand this dependence in much the same way we understood the dependence on V_{ds}. Changing the gate voltages cause a change $E = -e\alpha_g \Delta V_g$ in the energy of the dot, as well as a change $\delta U_2 = -e\alpha_{U2,g}\Delta V_g$ in the height of the tunnel barrier. Since the gates LP1, PL, and LP2 are closer to the dot than to $b2$, we expect that $\alpha_g > \alpha_{U2,g}$, so the change in energy of the dot will be greater than the change in the barrier. Then for increasing ΔV_g, the state is brought further below the top of the barrier and the tunneling rate between the dot and the lead decreases. Quantitatively, we have

$$\Gamma_{off} = \Gamma_2 e^{-\beta_{g,2}\Delta V_g}[1 - f(E)] \tag{4.12}$$

and

$$\Gamma_{on} = \eta \Gamma_2 e^{-\beta_{g,2}\Delta V_g} f(E) \tag{4.13}$$

where $\beta_{g,2} = \kappa_2|\alpha_{U2,g} - \alpha_g|$. The solid lines in Fig. 4-6(d) show fits to these equations and we obtain $\beta_{g,2} = 0.5$ mV^{-1}. In these fits we fix $\eta = 2$ because of the spin degeneracy of the ground state of the dot, although better agreement could be obtained with a smaller value [54]. The fact that the tunneling rate decreases as ΔV_g is made more positive supports our assumption of elastic tunneling. As ΔV_g is made more positive, the ground state is brought further below the Fermi energy of the lead, making more states available for inelastic tunneling processes. Despite these additional inelastic processes, the tunneling rate continues to decrease exponentially, which is consistent with our model based on purely elastic tunneling.

We can combine the equations to describe the tunneling rates of the ground state

72
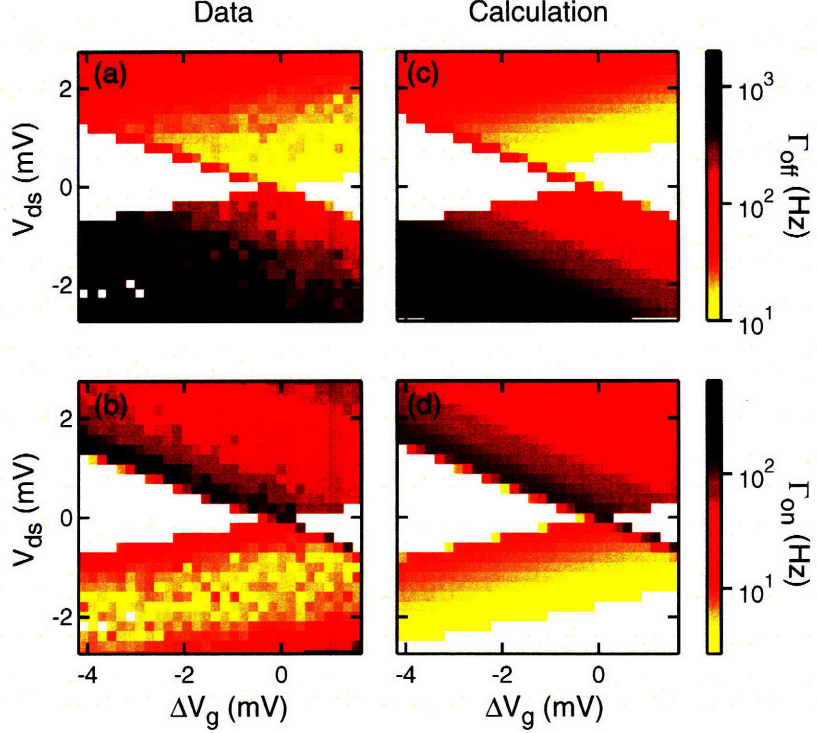
Figure 4-7: (a) and (b) show measurements of the rates for tunneling off of and onto the ground state of the quantum dot, respectively. In these data, the voltage on the QPC was changed slightly as a function of ΔV_g to maintain sensitivity over the entire range of gate voltages. (c) and (d) show results of the calculations of the rates. The value of $\beta_{g,2}$ in these calculations is different from that measured in Fig. 4-6(d) because the gate voltages are set differently to allow tunneling through both barriers. The white areas are regions where one of the calculated tunneling rates is less than 1 Hz.

as a function of both V_{ds} and ΔV_g. The combined equations are:

$$\Gamma_{off} = \Gamma_2 e^{-\beta_2 V_{ds} - \beta_{g,2} \Delta V_g} [1 - f_2(E)] + \Gamma_1 e^{\beta_1 V_{ds} - \beta_{g,1} \Delta V_g} [1 - f_1(E)]$$

and

$$\Gamma_{on} = \eta \Gamma_2 e^{-\beta_2 V_{ds} - \beta_{g,2} \Delta V_g} f_2(E) + \eta \Gamma_1 e^{\beta_1 V_{ds} - \beta_{g,1} \Delta V_g} f_1(E).$$

where $E = -e\alpha_{ds} V_{ds} - e\alpha_g \Delta V_g$ describes the combined effects of V_{ds} and ΔV_g on the energy of the ground state. Measurements of Γ_{off} and Γ_{on} as a function of V_{ds} and V_g are shown in Figs. 4-7(a) and (b), respectively. The white areas are regions

73

where one of the rates is negligibly small, so that there are few tunneling events. Tunneling rates calculated using the above equations are shown in Figs. 4-7(c) and (d). The calculation of Γ_{off} gives very good agreement with the data over the entire range. The calculation of Γ_{on} also gives good agreement, but starts to deviate from the data for $|V_{ds}| \gg 0$. These deviations are caused by the excited orbital states, which are not included in the calculation. These calculations show that we have a good understanding of the energy-dependence of tunneling in a quantum dot.

4.4 Spin-dependent tunneling into an empty quantum dot

4.4.1 Introduction

In the previous section, we develop a good understanding of tunneling in zero magnetic field. In this section, we study tunneling in a magnetic field. Tunneling in a magnetic field has been studied in both lateral GaAs quantum dots [60, 101, 102] and self-assembled InAs quantum dots coupled to three-dimensional electron reservoirs [103, 104]. Despite the progress in understanding the spin physics of tunneling, measurements of the spin state of electrons emitted from a lateral quantum dot in the Coulomb blockade regime by Potok *et al.* [55] remain unexplained. Using a magnetic focusing geometry and a QPC spin sensor [105], Potok *et al.* measure the spin polarization of electrons emitted from a quantum dot as the dot's spin state is varied from $S = 0$ to $S = 1$. Surprisingly, these authors find no variation in the polarization of the emitted electron's spin as they vary the spin state of the dot. These experiments point out the need to further understand the spin-dependence of tunneling in quantum dots.

In this section, we report experiments that use real-time charge sensing and gate pulsing techniques to probe electron tunneling into an empty quantum dot in a magnetic field B applied parallel to the 2DEG [94], where the spin states of the dot are split by the Zeeman energy $\Delta = |g|\mu_B B$. We find that the ratio of the rates for

74

tunneling into the excited and ground spin states of the empty dot decreases with increasing magnetic field. However, we find that by adjusting the voltages on the surface gates to change the orbital configuration of the dot, we restore tunneling into the excited spin state and the ratio of the tunneling rates reaches a maximum when the dot is symmetric.

4.4.2 Magnetic field dependence of tunneling

To measure the rate Γ_{on} for tunneling into the empty dot, we make the tunneling rate through $b1$ negligibly small relative to that through $b2$ and use a two-step pulse sequence (Fig. 4-8(a)) similar to that described in the previous section. First, we ionize the dot by bringing both spin states of the dot above the Fermi energy of the lead: if there is an electron on the dot then it tunnels off. Next is the loading step, during which we apply a voltage pulse V_p to gate LP2 to bring the ground spin
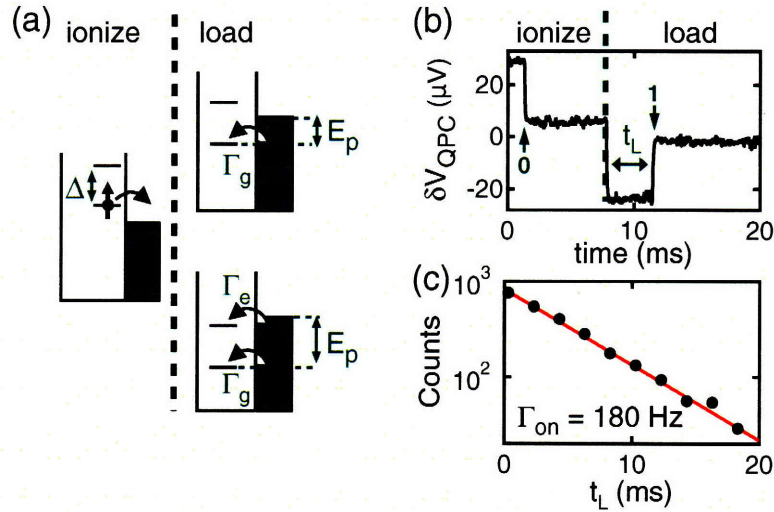
Figure 4-8: (a) Dot energy diagrams showing the positions of the Zeeman split spin states of the dot during the pulse sequence. (b) Example of real-time data. The direct capacitive coupling between LP2 and the QPC causes the QPC to respond to the pulse sequence; electron tunneling events are evident on top of this response. The 0's denote when an electron tunnels off the dot, while 1's denote when an electron tunnels onto the dot. (c) Example of a histogram of measurements of t_L for a given pulse depth V_p. The solid line is a fit to an exponential to find Γ_{on}.

75

state an energy $E_p = -e\alpha_{LP2}V_p$ below the Fermi energy of the lead for a period of time. During this time, an electron can tunnel into the ground spin state of the dot. For sufficiently large V_p, the excited spin state is also below the Fermi energy and an electron can tunnel into either spin state. We expect the rate Γ_{on} to increase when the excited spin state passes below the Fermi energy, because there is now an additional state into which the electrons can tunnel.

Figure 4-8(b) shows an example of real-time data. During the ionization step, we observe that an electron tunnels off of the dot, and then an electron tunnels onto the dot at a time t_L after we begin the loading step. We measure the time t_L with our automatic triggering system, and a histogram of these times for a fixed V_p is shown in Fig. 4-8(c). We fit these data to an exponential (solid line in Fig. 4-8(c)) to determine the rate Γ_{on} at which electrons tunnel onto the dot at this value of V_p.

The active feedback system plays an important role in this measurement. Before applying the pulse sequence, we use the feedback system to position the ground spin state near the Fermi energy. This ensures that the voltage pulse brings the state to the proper energy. We then apply a train of pulses, and after analyzing the data with the triggers, we run the feedback system again in preparation for another pulse train at a different V_p.

An example of Γ_{on} vs V_p at $B = 3$ T is shown in Fig. 4-9(a). The data is similar to the measurements of Γ_{on} in Fig. 4-6(d) (solid and open circles), except that there are now two increases in Γ_{on} instead of just one. The first rise at $V_p = 0$ is caused by the ground spin state passing below the Fermi energy, while the second rise at $V_p \approx 1$ mV is caused by the excited spin state passing below the Fermi energy. Figures 4-9(a)-(c) show examples of Γ_{on} vs V_p at several magnetic fields. The key qualitative feature of these data is that the rate increase associated with the excited spin state gets weaker with increasing magnetic field, and is not observable at $B = 7.5$ T. The arrow in Fig. 4-9(c) indicates where we would expect to find the rate increase.

We quantify this suppression of tunneling into the excited spin state relative[6] to

_____

[6]The tunneling rate through the barrier changes with magnetic field and hence it is necessary to adjust this rate using the gate voltages to keep Γ_{on} at measurable levels ($\approx 200 - 400$ Hz at the peak). This means it is not possible to compare the values of Γ_{on} at two different magnetic fields.
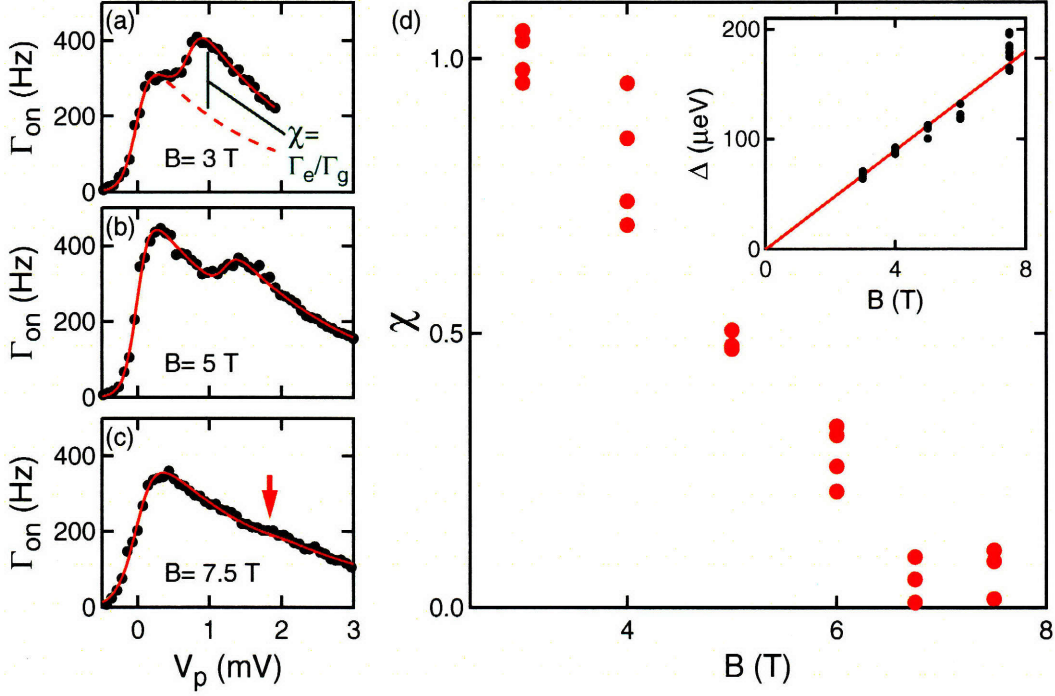
Figure 4-9: (a)-(c) Examples of Γ_{on} vs V_p at several magnetic fields. The solid and dashed lines are discussed in the text. In (a) and (b) the increase in Γ_{on} caused when the excited spin state passes below the Fermi energy of the lead is clearly visible, while the arrow in (c) marks the value of $V_p = \Delta/e\alpha_{LP2}$ where the feature is expected to be. (d) χ as a function of magnetic field from fits to data such as those in (a)-(c). For $B \leq 6$ T, the excited state feature is clearly visible and Δ can be extracted from the fit. For $B > 6$ T, the feature is not visible and fits are performed fixing $\Delta = |g|\mu_B B$, where $|g| = 0.39$ is determined by fitting measurements from which we can extract Δ (inset). These measurements include values at $B = 7.5$ T for different orbital configurations where tunneling into the excited spin state is not suppressed.

tunneling into the ground state by extending Eqn. 4.13 from the previous section to describe tunneling in a magnetic field:

$$\Gamma_{on} = \Gamma_2 e^{-\beta_{g.2}V_p}[f(E_p) + \chi f(E_p + \Delta)]. \tag{4.14}$$

Here $f(E_p)$ and $f(E_p + \Delta)$ give the occupation of the lead at the energies of the ground and excited spin states, respectively, and the factor χ accounts for spin-dependent tunneling.

The solid lines in Figs. 4-9(a)-(c) show fits to Eqn. 4.14 and the fits are in good agreement with the data. In Eqn. 4.14, the contribution of tunneling into the ground spin state is given by $\Gamma_g = \Gamma_2 e^{-\beta_{g.2}V_p}f(E_p)$ and this is shown by the dashed line in Fig. 4-9(a). The remaining contribution is caused by tunneling into the excited state with rate Γ_e. For pulses deep enough to bring the excited state below the Fermi energy so that $f(E_p) \approx f(E_p + \Delta) \approx 1$, we have $\chi = \Gamma_e/\Gamma_g$. In this way, χ describes the spin-dependence of the tunneling rates. Measurements of χ as a function of magnetic field B are shown in Fig. 4-9(d), and we see that χ decreases with increasing magnetic field.

4.4.3   Shape dependence of tunneling in a magnetic field

We affect this suppression by manipulating the orbital states of the dot using the voltages we apply to the gates [93]. The x and y axes of the dot, which correspond to the [110] and [$\bar{1}$10] GaAs crystalline axes, respectively, are shown in Fig. 4-10(a) (the magnetic field is parallel to the y-axis). When the voltages on all the gates that form the dot are approximately equal, we expect the dot to be less confined along the x-axis than along the y-axis because of the geometry of the gates, as illustrated by the black solid ellipse in Fig. 4-10(a). To change the shape of the dot. we apply a more negative voltage to gate SG1 and a less negative voltage to gates LP1, PL, and LP2; these changes are balanced to keep the ground state energy constant. The effect

---

Consequently we cannot determine whether the suppression is caused by an increase in the rate for tunneling into the ground spin state or a decrease in the rate for tunneling into the excited spin state.
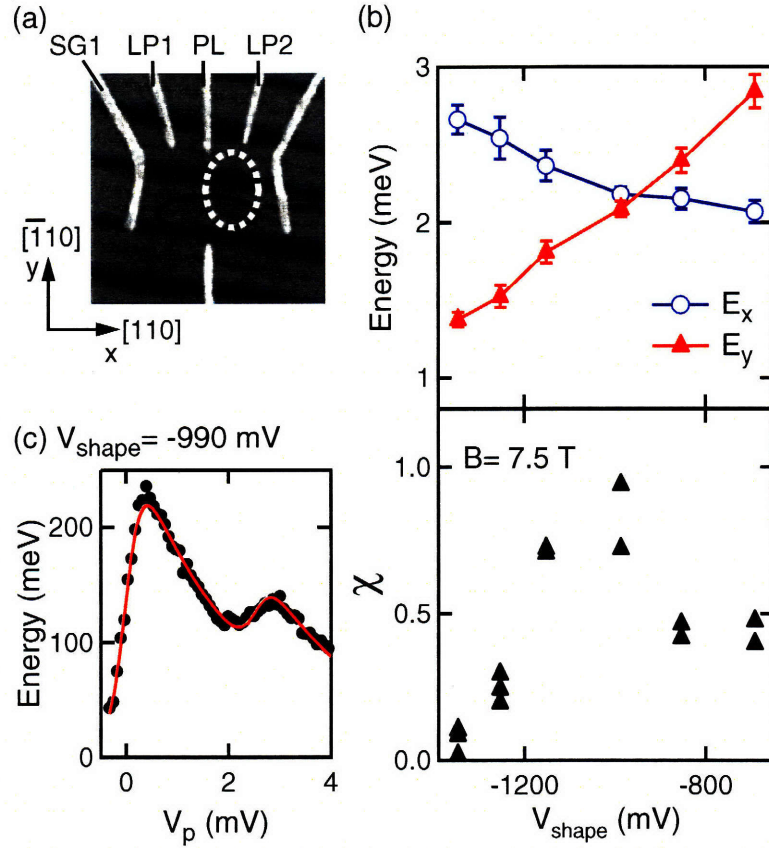
Figure 4-10: (a) The black solid (white dotted) ellipse illustrates the expected dot shape for less (more) negative V_{shape}. (b) The top panel shows the energies of the excited orbital states as a function of V_{shape}. The bottom panel shows χ measured at $B = 7.5$ T for each value of V_{shape}. (c) Data at $V_{shape} = -987$ mV and $B = 7.5$ T. Unlike Fig. 4-9(c), at this value of V_{shape} the excited state feature is clearly present. The value of V_p at which it appears is different than in Fig. 4-9(c) because α_{LP2} changes with V_{shape} (see Section 6.2).

of these changes is to increase confinement along x, while decreasing the confinement along y as illustrated by the white dotted ellipse in Fig. 4-10(a). We parameterize a set of gate voltages by V_{shape}, the numeric value of which is the voltage on gate SG1 (see Section 6.2 for more details). The data in Fig. 4-9 are at the most negative value of $V_{shape} = -1350$ mV.

We can characterize the change in the shape of the dot using the energies of the excited orbital states, which depend on the confinement potential. To see this, note that if we model the electrostatic potential of the dot with an anisotropic harmonic oscillator potential $U(x, y) = \frac{1}{2}m^*\omega_x^2 x^2 + \frac{1}{2}m^*\omega_y^2 y^2$, then the energies of the excited orbital states relative to the ground state are determined by confinement: $E_x = \hbar\omega_x$ and $E_y = \hbar\omega_y$. As we make V_{shape} more negative, we increase the confinement along x and decrease the confinement along y. Thus we expect that E_x should increase and E_y should decrease as V_{shape} is made more negative. The top panel of Fig. 4-10(b) shows the energies of the first two excited orbital states relative to the energy of the ground orbital state, which we measure using gate pulsing and real-time charge detection techniques [93] described in Section 6.2. As we expect, the energy of one state increases and the other state decreases as V_{shape} is made more negative, and this allows us to identify the states as indicated in the figure. Our interpretation of these data are confirmed by our measurements of the spin-relaxation time as a function of V_{shape}, which we discuss in Section 6.3.

At each value of V_{shape}, we measure Γ_{on} as a function of V_p at $B = 7.5$ T. From these data, we extract Δ, and verify it is independent of V_{shape}. We also extract χ and the results are shown in the bottom panel of Fig. 4-10(b). Clearly χ depends on V_{shape}, and χ reaches a maximum of ≈ 1 at $V_{shape} \approx -990$ mV. Figure 4-10(c) shows an example of data at this value of V_{shape}. In contrast to Fig. 4-9(c) the rise in Γ_{on} associated with the excited state is now clearly visible.

4.4.4 Discussion

If we assume that tunneling is elastic [80] and that there is no coupling between the electron orbital and spin states in the dot or the leads, then we would expect the

(a) $U_{eff,\uparrow}$ **(b)** $U_{eff,\downarrow} = U_{eff,\uparrow} + \Delta$
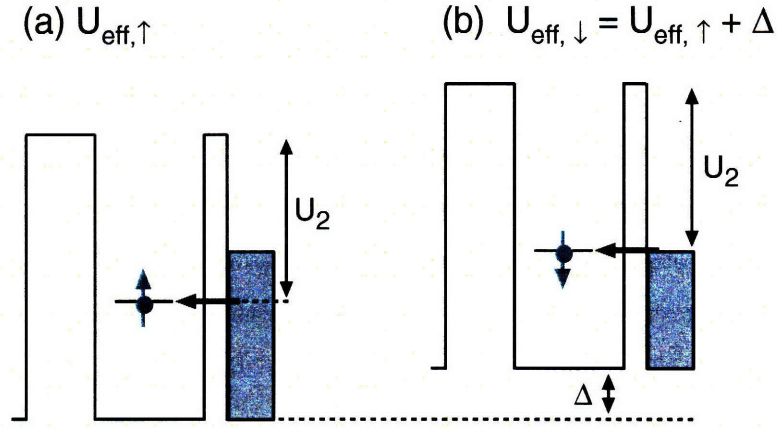
Figure 4-11: Dot diagrams for (a) spin-up and (b) spin-down electrons. The energies of the levels are set such that the excited spin state is aligned with the Fermi energy of the lead. Note that both spin species have the same Fermi energy. The horizontal arrows are to emphasize that we assume tunneling is elastic.

tunneling rates to be described by Eqn. 4.14 with $\chi = 1$. This is because in the absence of such coupling, the excited and ground spin states of the dot have the same orbital wavefunction and hence the same overlap with the leads. Thus the tunneling rates into both spin states should be the same, and the tunneling rates should have the same dependence on V_p.

This argument may seem counter-intuitive: because the spin-down state is higher in energy than the spin-up state, should not the two states have different tunneling rates? Although the spin-down state is higher in energy, the spin-down electrons tunneling into this state also see a higher tunnel barrier because the bottom of the conduction band for spin-down electrons is also shifted up by Δ, as illustrated in Fig. 4-11. To see this explicitly, we note the Hamiltonian for the system is $H = \frac{p^2}{2m^*} + U_{dot}(x,y) + \frac{1}{2}\Delta\sigma_y$, where U_{dot} is the electrostatic potential. The effective potential seen by the electrons is $U_{eff} = U_{dot} + \frac{1}{2}\Delta\sigma_y$. The potential is different for the two spin states, and they are related by $U_{eff,\downarrow} = U_{eff,\uparrow} + \Delta$. The key feature is that, assuming tunneling is elastic, the spin-up and spin-down electrons tunnel through barriers of equal height. Thus we expect tunneling to be described by Eqn. 4.14 with $\chi = 1$. That we observe χ changing with the magnetic field and with the shape of

81

the dot implies that this simple picture does not adequately describe the physics of electron tunneling in a magnetic field.

We consider several possible mechanisms- the spin-orbit interaction, a perpendicular magnetic field, and interaction with the QPC- but find that none of these account for the observed spin-dependence of tunneling. The variation of χ with the shape of the dot suggests that the tunneling into the spin states depends on the orbital states of the dot. One mechanism that can couple orbital and spin states is the spin-orbit interaction (SOI). As we will see in more detail in Chapter 6, the effect of the SOI on the states of the dot is to mix the Zeeman split ground orbital state with excited orbital states, so any difference in mixing between the spin states could cause spin-dependent tunneling. However, the SOI induced mixing is small because it is on the order of $x/\lambda_{SO} \approx 8 \times 10^{-3}$ where $x \approx 17$ nm is the length scale for a harmonic oscillator potential approximating a dot with energy spacing $E \approx 2$ meV, and the spin-orbit length $\lambda_{SO} \sim 2$ μm describes the strength of the SOI [93, 106]. Moreover, as the magnetic field increases the Zeeman splitting also increases, so the mixing of excited orbital states into the higher energy spin-down state is greater than the mixing into the lower energy spin-up state. Excited orbital states have stronger overlap with the leads, so the rate of tunneling into the spin-down state should increase relative to the rate into spin-up state and χ should increase with field, which is not what we observe in Fig. 4-9(d).

The SOI also couples the orbital and spin states of electrons in the leads. In the leads, the SOI can be thought of as a momentum-dependent effective magnetic field with magnitude $B_{SO} \approx \frac{2E_F}{\pi|g|\mu_B} \frac{\lambda_F}{\lambda_{SO}} \approx 6$ T at the Fermi energy, where $E_F \approx 7.7$ meV and $\lambda_F \approx 54$ nm are the Fermi energy and wavelength respectively. As the magnetic field increases we expect the Zeeman splitting to begin to dominate the SOI and the physics to approach the simple picture in Fig. 4-11, and thus χ should approach 1 at high fields. This is not what we observe.

Although we orient the sample such that the field is parallel to the 2DEG, a small misalignment could give a perpendicular field $B_\perp$. We estimate that the sample is parallel to within 5 degrees and this limits $B_\perp < 0.65$ T at $B = 7.5$ T, which is

the highest field we use. Since we are measuring single-electron tunneling into an empty quantum dot, there are no exchange effects in the dot; rather, the states of the dot are single-particle states. But $B_\perp$ can affect the states in the ohmic leads by forming Landau levels, and one possibility is that we would observe spin-dependent tunneling were the dot a spin-sensitive probe of the states in the leads [60]. We do not believe this is the case for several reasons. First, this mechanism does not explain how changes in the dot shape could affect χ. Also, we observe spin-dependent tunneling in a second device where we perform magneto-transport measurements on the device mesa. We find only a small variation in the voltage across the mesa with magnetic field, and if we ascribe this change to a Hall voltage, we extract $B_\perp \approx 20$ mT at $B = 7.5$ T.

Finally, we check whether the spin-dependence of tunneling depends on the current in the QPC by measuring χ for several different currents through the QPC in a second device. We vary the current by a factor of 3 (from 0.9 to 2.7 nA) but observe no significant variation in χ. These observations suggest that the QPC is not responsible for the observed effect.

Chapter 5

Spin Relaxation in Lateral Quantum Dots

In this chapter we describe how we measure the spin relaxation rate of a single electron confined in a lateral quantum dot in a magnetic field. Understanding this rate is important for spin-based applications. In the first section, we introduce spin relaxation in quantum dots and discuss theoretical predictions and previous measurements. In the second section, we discuss our measurement technique, while the third section focuses on one of the errors in our measurement. Finally, in the last section we discuss how we use measurements of the spin relaxation rate as a function of magnetic field to determine the relaxation mechanism in lateral quantum dots. Parts of this work are reported in Amasha *et al.* [107].

5.1 Introduction to spin relaxation

Understanding the interactions between a quantum system and its environment is essential to developing the system for use in applications, such as quantum information processing [29] and spintronics [21, 22, 23]. Recent experiments have demonstrated the ability to manipulate [34, 32] and read-out [35, 36] the spin states of an electron in a lateral GaAs quantum dot [4, 108], thus making this type of quantum dot an attractive option for spin based applications. One of the ways the spin of an electron in a

dot interacts with its environment is the hyperfine interaction between the electron's spin and the effective nuclear field B_{nuc} caused by nuclear spins [38, 37, 39, 41, 40]. This interaction causes phase decoherence, and the decoherence time T_2 has been measured [34].

An electron confined in a quantum dot can also exchange energy with its environment, and this affects the spin. In a magnetic field B the spin states of a single electron in a dot are split by the Zeeman energy $\Delta = |g|\mu_B B$, providing a two level quantum system. Spin relaxation occurs when the electron exchanges energy with its environment to bring the probabilities of being in the excited and ground spin states into thermal equilibrium. T_1 is the timescale over which this equilibrium is established; at low temperatures ($T \ll \Delta/k_B$), it is the average time necessary for an electron in the excited spin state to lose energy and relax to the ground spin state. Since relaxation necessarily destroys a coherent superposition of spins, it limits [46] the coherence time $T_2 < 2T_1$.

At fields $B \lesssim B_{nuc} \approx 3$ mT, the electron can relax by interacting with the nuclear spins [41]. For $B \gg B_{nuc}$, this mechanism is suppressed because of the mismatch between the Zeeman splittings for the electron and the nuclei. In this regime, a variety of mechanisms for spin relaxation have been proposed [45, 46, 109, 110, 47, 48, 111, 112, 113, 114]. Many of these mechanisms involve the spin-orbit interaction, which couples the spin states of the dot to the orbital states. The orbital states interact with fluctuating electric fields to exchange energy, and relax the spin of the electron. Relaxation can be induced by spin-orbit mediated coupling to electrical fluctuations caused by phonons [45, 46, 109, 110], as well as electrical fluctuations from surface gates [47], ohmic leads [48], or shot noise from an adjacent quantum point contact [111]. Spin relaxation can also be induced by hyperfine (rather than spin-orbit) mediated coupling to phonons [112] or gate fluctuations [47]. The mechanisms have different dependences on magnetic field (see Appendix A for details): spin-orbit mediated coupling to piezoelectric phonons is expected to dominate at large magnetic fields where spin relaxation should be faster, while the other effects may become important at low fields where relaxation should be slower.

Measurements of the spin relaxation rate $W \equiv T_1^{-1}$ over a range of fields can determine the mechanism. Such measurements are challenging because at low fields Δ is comparable to the electron temperature making spin read-out difficult. Also W is expected to be a very strong function of B, meaning an experiment must have a large dynamic range to be able to measure rates that vary over several orders of magnitude. Pulsed gate transport measurements [95, 69] in lateral dots have put lower bounds on T_1, while Elzerman et al. [35] have measured T_1 for one electron in a single lateral dot for $B \geq 8$ T and found $T_1 < 1$ ms. Hanson et al. [36] and Meunier et al. [115] have measured the triplet-singlet relaxation time at smaller fields for two electrons. Kroutvar et al. [28] have used optical methods to measure a layer of self-assembled Ga(In)As quantum dots and have demonstrated that spin-orbit mediated coupling to piezoelectric phonons accounts for the observed spin relaxation. However, the relaxation times in lateral GaAs quantum dots may be different because the presence of Indium in the self-assembled dots may lead to increased spin-orbit effects and because lateral quantum dots are coupled to surface gates, ohmic leads, and quantum point contacts, which may introduce new relaxation mechanisms at low fields.

In this chapter we describe techniques that allow us to measure the relaxation rate W of one electron in a lateral quantum dot from 7 T down to 1 T, a range over which W varies by 3 orders of magnitude. At 1 T we find $W < 1$ s^{-1}, which corresponds to $T_1 > 1$ s. These measurements are possible because of the good stability of the heterostructure we use combined with the active feedback system that compensates for residual drift and switches of the dot energy levels and allows us to maintain the stability of our read-out state, especially at low fields. Also our analysis method extends our dynamic range by allowing us to measure W even when it is faster than our electron tunneling rates. We find that our measurements of W as a function of field are fit well by a power-law and that the exponent is consistent with that predicted for the mechanism of spin-orbit mediated coupling to piezoelectric phonons [45, 46]. This demonstrates that this mechanism can account for spin relaxation in lateral quantum dots.

5.2 Measuring the spin relaxation rate

The quantum dot we use for the spin relaxation measurements is shown in Fig. 5-1. For these measurements, we adjust the voltages on the gates to make the tunneling rate through barrier $b2$ (defined by gates SG2 and OG) much larger than that through barrier $b1$ (defined by gates SG1 and OG). As in the previous chapter, this gives a dot coupled to a single lead.

To measure W at a given magnetic field, we apply a three step pulse sequence [35] on top of the dc voltage on gate LP2: $V_{LP2} = V_{dc} + V_p$. This sequence is illustrated in Fig. 5-2(d), where we convert the gate voltage pulse V_p into the resultant change in the energies of the states of the dot using $E_p = -e\alpha_{LP2}V_p$. Figures 5-2(a)-(c) show the positions of the spin states of the dot during each step in the sequence. First we bring both spin states above the Fermi energy of the lead (Fig. 5-2(a)) so that any electron on the dot will tunnel off, leaving the dot empty or ionized. Next, we bring both states below the Fermi energy of the lead (Fig. 5-2(b)) and hold the dot in this configuration for a time t_w, which we vary. During this time, an electron can tunnel into either the excited or the ground spin state of the dot with rate Γ_e or Γ_g, respectively. An electron that has tunneled into the excited state can also relax with rate W. So at the end of t_w there are three possible states for the dot. There is some probability that t_w is not long enough for an electron to tunnel into the dot, so the dot is still ionized: this is the ionized probability $P_i(t_w)$. There is also a probability $P_e(t_w)$ that the electron is still in the excited spin state, and this probability depends on W. Finally, there is some probability $P_g(t_w)$ that the electron is in the ground spin state of the dot.

The final step in the pulse sequence is the real-time read-out, shown in Fig. 5-2(c). We follow Elzerman *et al.* [35] and position the levels so that the excited state is above or near the Fermi energy of the lead and the ground state is below the Fermi energy. In this configuration, an electron in the excited spin state can quickly tunnel off the dot with rate Γ_{off}, while the tunneling rate of an electron out of the ground state Γ_b is exponentially suppressed.
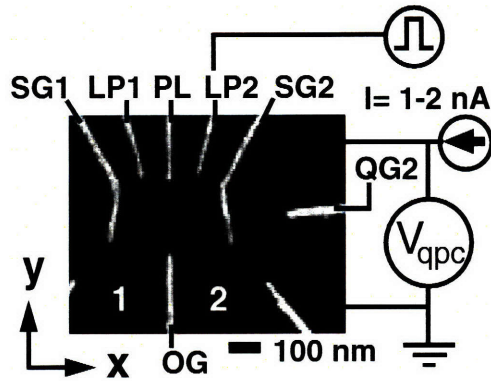
Figure 5-1: Electron micrograph of the gate geometry. Negative voltages are applied to the labeled gates to form the quantum dot and the QPC charge sensor; unlabeled gates and the ohmic leads labeled 1 and 2 are grounded. Pulses are applied to gate LP2.
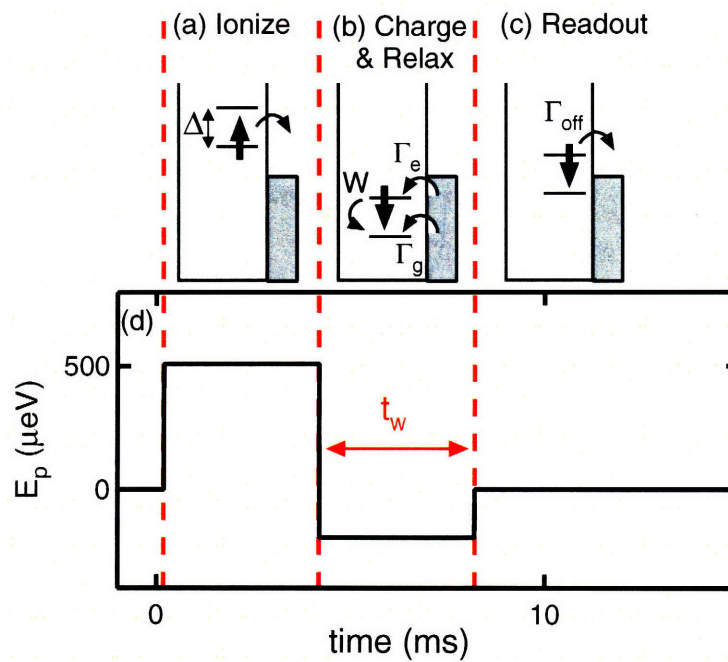
Figure 5-2: (a)-(c) diagrams showing the positions of the spin states during the three steps in the pulse sequence. In (b) relaxation is illustrated in the case where $\Delta \gg k_B T$ and an electron relaxes from the excited to the ground spin state. At lower fields where $\Delta \sim k_B T$, the reverse rate (from the ground to the excited state) is not negligible and W is the sum of the forward and reverse rates (see Appendix A.7). (d) The three step pulse sequence converted into the resultant change in the energies of the states of the dot.

An important part of our experiment is maintaining the stability of the read-out configuration, especially at low B where Δ is comparable to k_BT. To do this, we use the active feedback mechanism described in Section 4.2. The active feedback maintains $\Gamma_b \sim 10$ Hz, which keeps the ground spin state the proper energy below the Fermi energy of the lead. We run the feedback routine between applications of the T_1 measurement pulse sequence described above; we typically run the feedback routine at least once every several minutes, if not more frequently. The active feedback system maintains stability and allows us to collect large numbers of pulses at each t_w and B, typically between 4×10^3 and 1.5×10^5 pulses.

Figures 5-3(a) and (b) show two examples of data taken at $B = 2.5$ T and $t_w = 4$
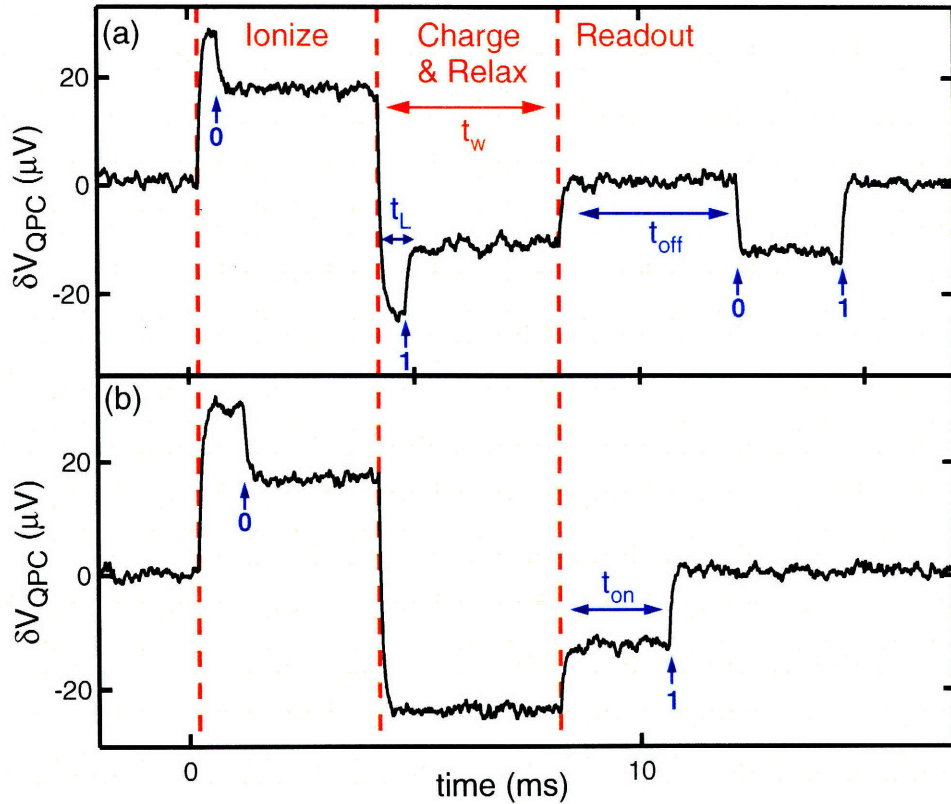
Figure 5-3: Examples of real-time data that results from applying the spin relaxation measurement pulse sequence. The direct capacitive coupling between LP2 and the QPC causes the QPC to respond to the pulse sequence; electron tunneling events are evident on top of this response. The 0's denote when an electron tunnels off the dot, while 1's denote when an electron tunnels on.

ms. In Fig. 5-3(a) we see that an electron tunnels off during the ionization pulse, leaving the dot empty. During the charging pulse, an electron tunnels onto the dot a time t_L after the pulse is applied. When we enter the read-out step, the electron tunnels off the dot, presumably from the excited spin state, at a time[1] t_{off} after the end of the charging pulse. Shortly after the electron tunnels off, an electron tunnels back onto the empty dot. We call this behavior a 'tunnel-off' event. In contrast, in Fig. 5-3(b) we see an electron tunnel off during the ionization pulse, but no electron tunnels on during the charging pulse. Thus the dot is empty entering the read-out stage and the first event in this stage is an electron tunneling onto the empty dot. We call this an 'ionization event', and measure the time t_{on} between the end of the charging pulse and the time when an electron tunnels onto the dot. We measure the times using the automatic triggering system discussed in Section 3.3.

From data such as those in Fig. 5-3 we measure the probabilities. To measure the ionized probability $P_i(t_w)$. we need to count the number of times N_i that the dot is empty entering the read-out step. To do this we histogram the measurements of t_{on} from ionization events like the one shown in Fig. 5-3(b). The results are shown in Figs. 5-4(a)-(c) for three different sets of B and t_w. We fit the data to an exponential, and the fit is shown by the solid lines in the figures. The area underneath the exponential gives N_i, and the ionized probability is then determined by $P_i = N_i/N_{pulses}$, where N_{pulses} is the total number of pulses applied at the given t_w and B.

The rate of the exponential decrease is just the rate Γ_{on} at which electrons tunnel onto the empty dot in the read-out state (Fig. 5-4(d)). In a given magnetic field, the read-out configuration is the same for all values of t_w, so we expect that Γ_{on} should be independent of t_w. This is demonstrated by the data in Figs. 5-4(e)-(g), which shows the value of Γ_{on} measured at each t_w. It is not meaningful to compare the values of Γ_{on} at different fields, because we modify the voltages on the gates SG2 and OG at each field to tune the tunneling rate through $b2$ to a value convenient for the

---

[1]Note that our definitions of t_{off} and t_{on} in this section are different from the definitions of these variables in Chapter 4.
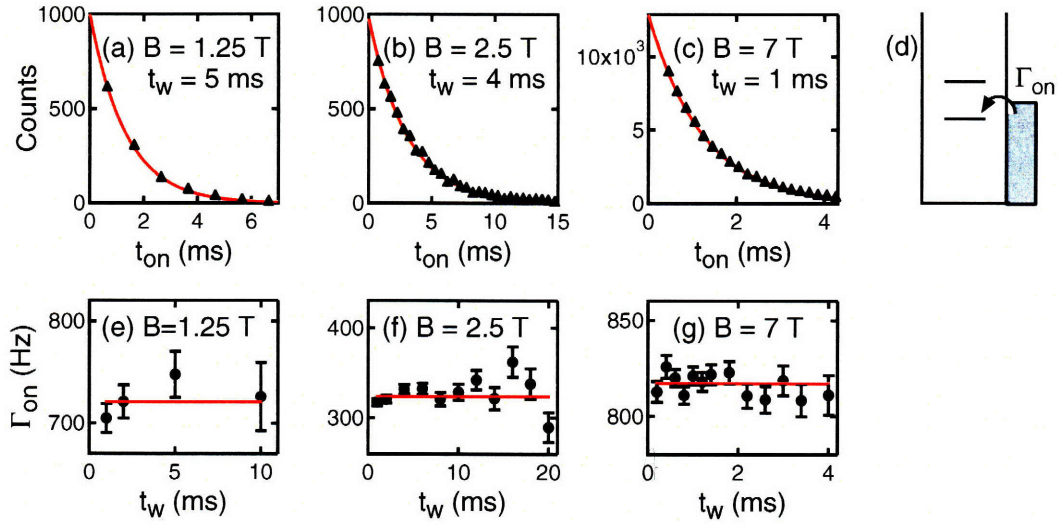
Figure 5-4: (a)-(c) Histograms of t_{on} for ionization events for three different sets of B and t_w. The solid lines are fits to exponentials discusses in the text. The rate of decrease of the exponential is the rate Γ_{on} at which electrons tunnel into the empty dot in the read-out state as illustrated by the dot diagram in (d). (e)-(g) show measurements of Γ_{on} as a function of t_w at a given field extracted from histograms like those in (a)-(c). The solid lines are the average values of Γ_{on}, which are 720, 320, and 820 Hz respectively.
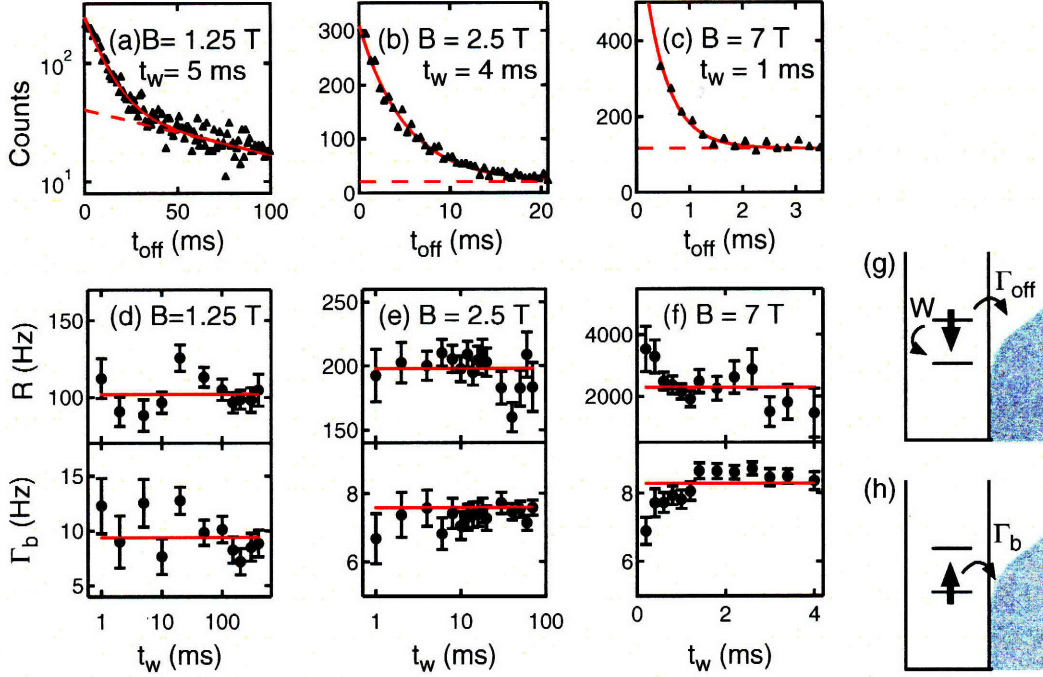
Figure 5-5: (a)-(c) Histograms of t_{off} for tunnel-off events for three different sets of B and t_w. Solid lines show fits described in the text. (d)-(f) Measurements of R (top panel) and Γ_b (bottom panel) as a function of t_w at a three different magnetic fields extracted from histograms like those in (a)-(c). The solid lines are the average values of R (102, 198, and 2300 Hz, respectively) and Γ_b (9, 8, and 8 Hz, respectively). (g) Dot diagram illustrating how an electron can leave the excited spin state in the read-out configuration by either tunneling off the dot or relaxing to the ground state. (h) Dot diagram illustrating an electron tunneling off the dot out of the ground state.

measurement.

To measure the probability P_e that an electron is still in the excited spin state after a given t_w, we need to count the number of times N_e the electron is in the excited spin state entering the read-out step. To do this, we histogram the measurements of t_{off} from tunnel-off events and the results are shown in Figs. 5-5(a)-(c) for three different sets of t_w and B. At low fields (Fig. 5-5(a)), Δ is comparable to temperature and the rates for tunneling out of the ground and excited states are similar. At these fields the data are fit well by a double exponential (solid line in Fig. 5-5(a)): the faster exponential with rate R is from electrons leaving the excited state (Fig. 5-5(g)), while the slower exponential is caused by tunneling out of the ground state at rate Γ_b

93

(Fig. 5-5(h)). The contribution of tunneling from the ground state is shown explicitly as the dashed line in Fig. 5-5(a). At larger fields (Figs. 5-5(b) and (c)), R is large enough compared to Γ_b that the background can be approximated as a constant offset (dashed line). The complete read-out probability distribution $\mathcal{P}_{ro}(t_{off})$ is derived in Appendix B.2.

Since the read-out state is the same for all values of t_w at a given magnetic field, we expect that the rates R and Γ_b should be independent of t_w. This is demonstrated by the data in Figs. 5-5(d)-(f), which show the values of R and Γ_b extracted from fits to histograms such as those in Figs. 5-5(a)-(c). The measurements at the two shortest t_w at $B = 7$ T do differ from the average, but at these small values of t_w most events are ionization events, and so the measurement is not as accurate because of the low statistics. Note that the average value of Γ_b is near 10 Hz for all three data sets, which demonstrates the efficacy of our feedback system.

The data also show that the rate R is independent of t_w. Two different processes contribute to the rate R at which an electron can exit the excited state. The electron can tunnel to the lead with rate Γ_{off} or the electron can relax before it has a chance to tunnel off the dot [36], as illustrated in Fig. 5-5(g). Thus $R = \Gamma_{off} + W$ and the area under the exponential and above the background is the fraction $\eta \equiv \Gamma_{off}/(\Gamma_{off} + W)$ of the number of electrons in the excited state that tunnel off before they relax (see Appendix B.2 for more details). Thus the area under the exponential and above the background is ηN_e, and we then determine $\eta P_e = \eta N_e/N_{pulses}$. Since $\eta = \Gamma_{off}/(\Gamma_{off} + W) = (R - W)/R$ is independent of t_w, this multiplicative factor does not affect our ability to extract W.

Figures 5-6(a)-(c) show measurements of P_i and ηP_e as a function of t_w at three different magnetic fields. To understand these data we consider the processes that occur during the charging pulse (Fig. 5-2(b)): electrons tunnel into either the ground or excited states with rates Γ_g and Γ_e, respectively, and relax with rate W. For $\Delta \gg k_B T$ the corresponding rate equations are $\dot{P}_i = -\Gamma_t P_i$ and $\dot{P}_e = \Gamma_e P_i - W P_e$, with $\Gamma_t = \Gamma_e + \Gamma_g$. Solving these equations, we find that the probabilities after time
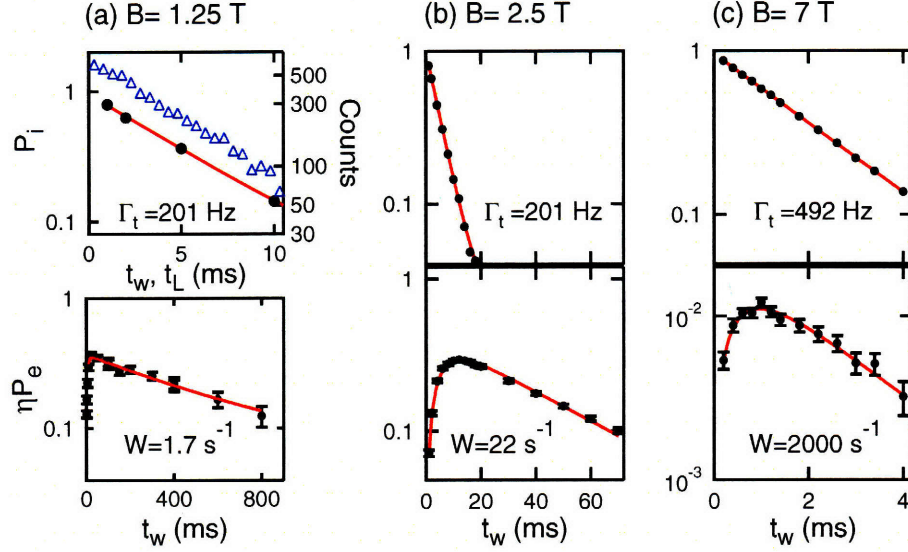
Figure 5-6: (a)-(c) The filled circles show measurements of P_i and ηP_e as a function of t_w at different values of B. The solid lines are fits discussed in the text. In (a), the open triangles go with the right axis, and are the results of making a histogram of the values of t_L at $B = 1.25$ T and $t_w = 50$ ms.

t_w are

$$P_i(t_w) = \epsilon_i e^{-\Gamma_t t_w} \tag{5.1}$$

$$P_e(t_w) = \epsilon_i \frac{\Gamma_e}{\Gamma_t} \frac{\Gamma_t}{\Gamma_t - W}\left(e^{-W t_w} - e^{-\Gamma_t t_w}\right) \tag{5.2}$$

where ϵ_i is the probability the dot is ionized by the ionization pulse. At the lowest fields where $\Delta \sim k_B T$, we need to add the term $\frac{1 - e^{-W t_w}}{1 + e^{\Delta/k_B T}}$ to Eqn. 5.2 to account for the fact that the excited state population at equilibrium is not negligible (see Appendix B.1 for details). Note that the t_w dependence of P_e depends only on W and Γ_t. In particular Eqn. 5.2 has a maximum at $t_w = \ln(\Gamma_t/W)/(\Gamma_t - W)$.

We determine Γ_t and ϵ_i by fitting measurements of $P_i(t_w)$ to Eqn. 5.1 (we include a constant offset in the fit for reasons we discuss in the next section). The fits are shown as solid lines in the top panels of Figs. 5-6(a)-(c), and the values of Γ_t extracted from the fits are shown in the figure. Another method of measuring Γ_t is to histogram the measurements of the times t_L for an electron to tunnel onto the dot during the charging pulse from events like the one in Fig. 5-3(a). An example of such a histogram

95

is shown by the open triangles in the top panel of Fig. 5-6(a), which go with the right axis. We fit these data to an exponential and obtain $\Gamma_t = 204$ Hz, which is in excellent agreement with the measurement of Γ_t from fitting P_i.

Using the value of Γ_t, we fit the measurements of $\eta P_e(t_w)$ to Eqn. 5.2 to find W and the prefactor $\Xi = \eta \epsilon_i \Gamma_e / \Gamma_t$. These fits, shown as the solid lines in the lower panels in Figs. 5-6(a)-(c), give excellent agreement with the data. It is important to note that since we measure Γ_t independently, the t_w dependence of P_e determines W.

From the upper and lower panels of Figs. 5-6(a)-(c), one can explicitly see the relationship between $P_i(t_w)$ and $P_e(t_w)$ in two different regimes. In Figs. 5-6(a) and (b) $\Gamma_t > W$, and P_i decreases over a timescale of Γ_t^{-1} as it becomes more likely that an electron has tunneled onto the empty dot. ηP_e increases over this same timescale as electrons tunnel into the excited state. After this timescale, the dot is occupied and then ηP_e decreases exponentially with rate W as the excited state population relaxes. We can see this quantitatively in Eqn. 5.2: in the limit $\Gamma_t^{-1} < t_w$ we have $\eta P_e \approx \eta \epsilon_i (\Gamma_e / \Gamma_t) e^{(-W t_w)}$.

In Fig. 5-6(c), $\Gamma_t < W$. In this case, the dot relaxes much faster than it loads. So P_e increases until it is cut-off by the relaxation rate at a timescale given by W^{-1}. After this time the probability of being in the excited state is saturated at the loading rate Γ_e divided by the rate out of the excited state W, multiplied by the probability that the dot is empty P_i. We can see this explicitly from Eqn. 5.2: in the limit $W^{-1} < t_w$ we have $\eta P_e \approx \eta \epsilon_i (\Gamma_e / W) e^{(-\Gamma_t t_w)} = \eta (\Gamma_e / W) P_i(t_w)$. Thus $P_i(t_w)$ and $P_e(t_w)$ decrease with the same rate at long t_w, which is what we observe in the data. Because we can measure Γ_t directly from P_i, we can still measure W in this regime. Thus our analysis allows us to determine W over a large dynamic range.

5.3 Event misidentification

In this section we consider one of the sources of error in the spin relaxation measurement in greater detail. The capacitance between gate LP2 and the QPC causes the QPC to respond to the pulse sequence. Unfortunately, if the gate pulse is large enough, the edge trigger will identify the gate pulse as an electron tunneling event[2]. To avoid triggering on the voltage pulses, we need to allow time for the QPC to relax. To this end, we introduce a delay of about $250 - 350$ μs between when the dot is pulsed into the read-out configuration and when the triggers start looking for electron tunneling events. This delay is illustrated in Fig. 5-7: the left-most dashed vertical line marks the time when the levels on the dot are pulsed into the read-out configuration and the second dashed line marks the time when the triggers begin looking for electron tunneling events. We call the time between when we enter the read-out configuration and when the triggers start looking for events the 'blind spot'.

This delay causes the triggers to misidentify electron tunneling events on occasion, and the two types of misidentification are shown in Fig. 5-7. The data in Fig. 5-7(a) show an example of an ionization event that is misidentified as a tunnel-off event: the dot is ionized when it enters the read-out state but the triggers miss the electron tunneling into the empty dot because it happens during the blind spot. The first charge transition observed is when the electron tunnels off the dot, and hence this is misidentified as a tunnel-off event. An example of the other type of misidentification is shown by the data in Fig. 5-7(b): an electron is on the dot when the dot enters the read-out state and tunnels off during the blind spot. Then the first electron transition found by the trigger is an electron tunneling back onto the empty dot, causing this event to be misidentified as an ionization event.

These misidentified events can have a small effect on our measurements of P_i and P_e, as shown by the data in Fig. 5-8. The data in Fig. 5-8(a) shows measurements of P_i out to long values of t_w, where P_i decreases at a much slower rate. At such long values of t_w there should be no ionization events, and this tail in P_i is caused by tunnel-

---

[2]We actually took advantage of this in Section 3.3 to characterize the edge trigger.
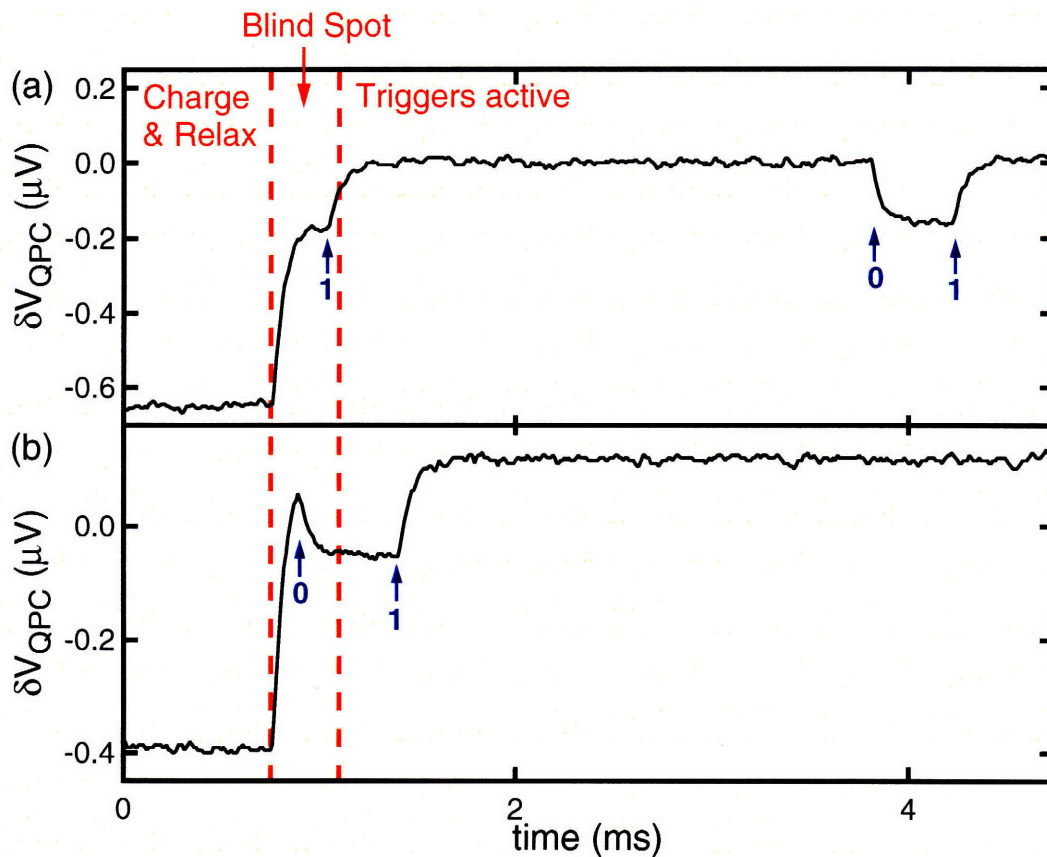
Figure 5-7: Real-time data taken during the T_1 measurement pulse sequence at $B = 2$ T. The 0's denote when an electron tunnels off the dot, while 1's denote when an electron tunnels on. The left-most dashed vertical line marks when the dot is pulsed into the read-out state, while the right-most dashed vertical line marks when the triggers start searching for electron tunneling events. The time in-between (350 μs in this example) is the blind spot. In (a), an electron tunnels into the empty dot during the blind spot, and this event is misidentified as a tunnel-off event. In (b) an electron tunnels off during the blind spot, and this event is misidentified as an ionization event.

off events that the triggers misidentify as ionization events. We can quantitatively describe this effect by noting that this type of misidentification is much more likely to happen when the electron is in the excited spin state rather than the ground spin state, because the rate out of the excited state is much greater than the rate out of the ground spin state. Then the contribution to P_i caused by misidentified events should be proportional to P_e, and using Eqn. 5.2 for P_e we have

$$
\begin{aligned}
P_i(t_w) &= \epsilon_i e^{-\Gamma_t t_w} + A_i P_e(t_w) \\
&= \epsilon_i e^{-\Gamma_t t_w} + \tilde{A}_i (e^{-W t_w} - e^{-\Gamma_t t_w}) \\
&= (\epsilon_i - \tilde{A}_i) \, e^{-\Gamma_t t_w} + \tilde{A}_i \, e^{-W t_w}.
\end{aligned}
$$

Here A_i is the contribution of misidentified excited state events to P_i and $\tilde{A}_i = A_i \epsilon_i \frac{\Gamma_e}{\Gamma_t} \frac{\Gamma_t}{\Gamma_t - W}$. The solid line in Fig. 5-8(a) shows a fit to a double exponential. There is good agreement with the data and we extract the rates $\Gamma_t = 201$ Hz and $W = 15$ s^{-1} from the fit. This value of Γ_t is consistent with the measurement of $\Gamma_t = 206$ Hz from histograms of the times t_L for an electron to tunnel onto the dot during the charging pulse. Also, the measurement of W is consistent with $W = 15$ s^{-1} which we obtain from fitting ηP_e. As an alternative to the double exponential fit, we find that fitting the data with a single exponential with a constant offset also gives an accurate value for Γ_t. Fitting to a single exponential without an offset gives $\Gamma_t = 180$ Hz, which is significantly slower than the correct value.

Misidentified events also have a small effect on our measurement of ηP_e. One way this happens is from a misidentified ionization event: the dot is empty when it enters the read-out state and an electron tunnels into the excited spin state of the dot during the blind spot. This electron then tunnels out of the dot while the triggers are active, as shown in Fig. 5-7(a), and is counted as a tunnel off event. This will then lead to an artificial enhancement in our measurement of the probability of being in the excited spin state.

This effect is not significant at high fields, because the excited spin state is above
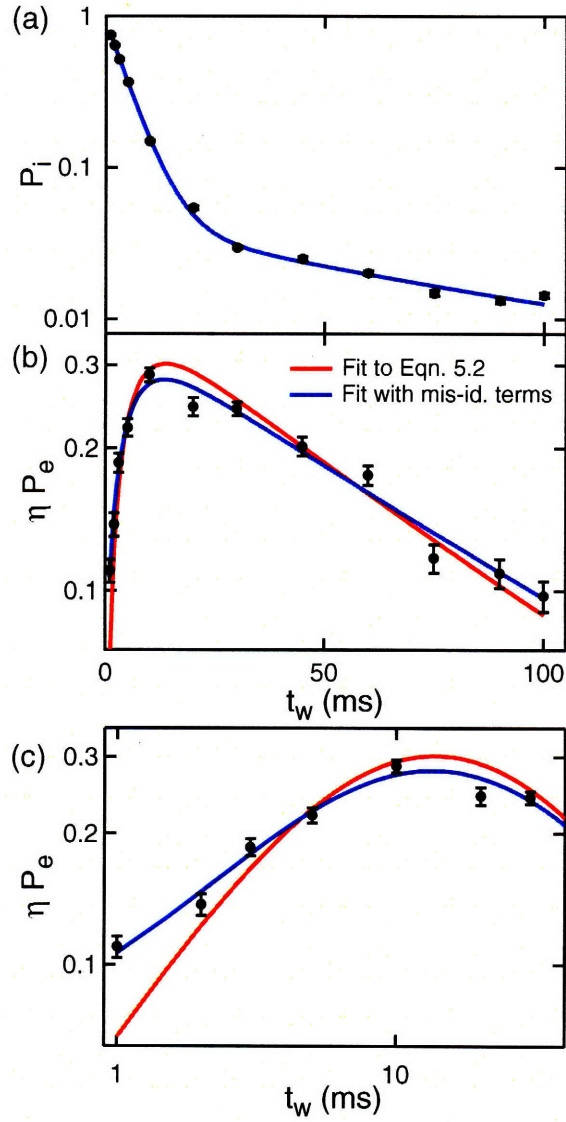
Figure 5-8: Measurements of (a) $P_i(t_w)$ and (b) $\eta P_e(t_w)$ at $B = 2$ T. (b) is a semi-log plot, while (c) is a log-log plot of the data in (b) over a smaller range in t_w. The solid lines are fits discussed in the text.

the Fermi energy of the lead in the read-out state and the probability of an electron tunneling into this state is negligible. But for data at low fields, like those in Fig. 5-8 which is at $B = 2$ T, this type of misidentification can affect ηP_e. Measurements of ηP_e as a function of t_w are shown in Fig. 5-8(b) and one of the curves shows a fit to Eqn. 5.2. Since this type of misidentification requires that the dot be ionized when entering the read-out state, the effect is largest at low values of t_w, when there is a high probability the dot is ionized. Figure 5-8(c) focuses on ηP_e at $t_w < 40$ ms. The fit to Eqn. 5.2 is not consistent with the measurements because of the enhancement caused by misidentified ionization events. Since the probability of this type of misidentified event is proportional to P_i, we can quantitatively account for these misidentified events by adding a term $A_e P_i = \tilde{A}_e e^{-\Gamma_i t_w}$ to Eqn. 5.2, where we use Eqn. 5.1 for P_i, $\tilde{A}_e = A_e \epsilon_i$, and A_e describes the contribution of the misidentified events. The other curve in Figs. 5-8(b) and (c) shows a fit to this equation, and it gives good agreement with the data. From this we obtain $W = 14$ s^{-1}. From the fit to Eqn. 5.2 over the full range we obtain $W = 16$ s^{-1}, which is close to the value obtained by fitting to the form that accounts for misidentified events.

To determine the central value of W we use the fit to Eqn. 5.2 over a range of t_w where the effect of misidentification is small ($t_w \geq 3$ ms in Fig. 5-8(b)). For the data in Fig. 5-8(b) this gives $W = 15$ s^{-1}, which is very close to the value obtained from the fit accounting for misidentification. We use the fit to the equation that includes the term accounting for misidentification to help determine the error bar on the central value. We choose error bars that encompass the value from the fit including the misidentification term, as well as the results of other fits where we vary the range of t_w that we fit over, etc.

5.4 Magnetic field dependence of the spin relaxation rate
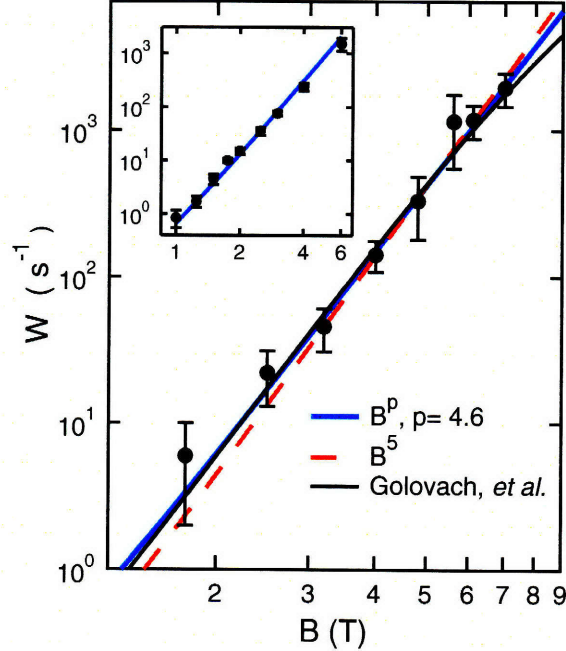
Figure 5-9: Spin relaxation rate W as a function of magnetic field. The lines are fits discussed in the text. The inset shows W as a function of B for a different set of gate voltages. The fit in the inset is to the temperature-corrected power-law with $p = 4.6$.

Using the techniques we discuss in the previous sections, we measure W as a function of magnetic field and the data are plotted in Fig. 5-9 (the inset shows data for a different set of gate voltages). At low fields, the relaxation rate becomes very slow: we measure $T_1 > 1$ s at $B = 1$ T (Fig. 5-9 inset). These data also demonstrate that we can measure W over 3 orders of magnitude.

In the limit where the dipole approximation can be applied to the electrical fluctuations (such as when the phonon wavelength is much larger than the dot), theory predicts that W is a power-law in field: $W = CB^p \coth(\Delta/(2k_B T))$ where p is determined by the spin relaxation mechanism and the coth factor accounts for finite temperature at low fields (see Appendix A for details). Spin-orbit mediated coupling to piezoelectric phonons [45, 46] gives $p = 5$, while other mechanisms [47, 48, 111, 112]

that could contribute at low fields give different values of p. For example, spin-orbit mediated coupling to gate or ohmic electrical fluctuations [47, 48] give $p = 3$, as does hyperfine mediated coupling to piezoelectric phonons [112]. The thick solid line in Fig. 5-9 shows a fit to this temperature-corrected power law and we find $p = 4.6 \pm 0.8$, which is consistent with spin-orbit mediated coupling to piezoelectric phonons. The red dashed line shows a fit with $p = 5$ and is consistent with the data.

At $B = 7$ T, the wavelength of the phonon emitted via spin relaxation is $\lambda = \Delta/v_s \approx 100$ nm, where $v_s \approx 4000$ m/s is the average sound velocity in GaAs. This wavelength is close to the size of the dot, so we compare our data to a theoretical prediction for spin-orbit mediated coupling to phonons by Golovach et $al.$ [46] that includes finite wavelength effects. The calculation is shown as the solid black line in Fig. 5-9 and gives good agreement with the data. We discuss this calculation in more detail in the next chapter.

Chapter 6

Electrical Control of Spin Relaxation in a Quantum Dot

In the previous chapter, we use the magnetic field dependence of the spin relaxation rate $W \equiv T_1^{-1}$ to identify the relaxation mechanism in lateral quantum dots as spin-orbit mediated coupling to piezoelectric phonons. In this chapter, we utilize this mechanism to demonstrate *in-situ* electrical control over the relaxation rate. In the first section, we discuss the spin-orbit interaction and spin-orbit mediated coupling to phonons in more detail. In particular, we see that in this mechanism spin relaxation involves the excited orbital states of the dot. In the second section, we discuss how we use the gate voltages to control the electrostatic confinement potential of the dot, and hence affect the orbital states. Finally, in the last section, we study how the spin relaxation rate changes as we vary the confinement potential and demonstrate that we can vary W by over an order of magnitude at fixed $\Delta = |g|\mu_B B$. We find that W depends only on the confinement of the electron wavefunction in the direction along the applied in-plane magnetic field, as expected for the spin-orbit interaction in GaAs, and that the dependence of W on the energy scale for confinement is that predicted by theory [45, 46]. From these data we extract the spin-orbit length, which describes the strength of the spin-orbit interaction. These results are reported in Amasha *et al.* [93].

105

6.1 Spin relaxation via the spin-orbit interaction

6.1.1 The spin-orbit interaction

An essential component to spin relaxation in GaAs quantum dots is the spin-orbit interaction (SOI). The SOI is a relativistic effect that arises from the orbital motion of electrons through electric fields intrinsic to the AlGaAs/GaAs heterostructure. In the electron's rest frame these intrinsic electric fields transform into magnetic fields that interact with the electron's spin.

One of the intrinsic electric fields in the heterostructure is the field that is perpendicular to the AlGaAs/GaAs interface. This field is caused by the lack of inversion symmetry in the heterostructure and gives rise to Rashba spin-orbit coupling [116]. One can get an intuitive understanding of the form of the Rashba term in the spin-orbit Hamiltonian by considering the transformation of a uniform electric field $\mathbf{E} = E\hat{z}'$. The primed coordinate system refers to the GaAs crystalline axes, with x', y', and z' corresponding to [100], [010], and [001], respectively. For an electron with momentum $\mathbf{p}$, this electric field transforms into a magnetic field in the electron's rest frame [117] given by $\mathbf{B} = -\frac{1}{m^*c^2}\mathbf{p} \times \mathbf{E} = \frac{E}{m^*c^2}(-p_{y'}, p_{x'}, 0)$ where m^* is the effective mass of the electron. The electron's spin interacts with this magnetic field via $H = \frac{g\mu_B}{\hbar}\mathbf{B} \cdot \mathbf{S}$, where $\mathbf{S} = \frac{\hbar}{2}\boldsymbol{\sigma}$ and $\boldsymbol{\sigma}$ are the Pauli matrices. This gives

$$H_R = \alpha(p_{x'}\sigma_{y'} - p_{y'}\sigma_{x'})$$

where α is the Rashba spin-orbit parameter. This is the form of the Rashba term in the spin-orbit Hamiltonian [116]. While this argument gives intuition as to the form of the Rashba term, it is important to note that proper calculations of α are much more complicated, and involve the band structure of GaAs [118].

A second contribution to the SOI in GaAs arises because GaAs is a polar crystal and the zinc blende crystal structure of GaAs lacks inversion symmetry. This creates an intrinsic electric field, which causes Dresselhaus spin-orbit coupling [119]. From

106

band structure calculations, this type of spin-orbit coupling takes the form [120]:

$$H_D = \gamma[\sigma_{x'}p_{x'}(p_{y'}^2 - p_{z'}^2) + \sigma_{y'}p_{y'}(p_{z'}^2 - p_{x'}^2) + \sigma_{z'}p_{z'}(p_{x'}^2 - p_{y'}^2)]$$

where γ describes the strength of the interaction. Electrons in the 2DEG are confined in the z-direction, where they occupy the lowest sub-band, and this gives $\langle p_{z'} \rangle = 0$ while $\langle p_{z'}^2 \rangle \neq 0$ [118, 108]. Combining this with the above equation gives us the familiar form for the Dresselhaus spin-orbit term:

$$H_D = \beta(p_{y'}\sigma_{y'} - p_{x'}\sigma_{x'}) + \gamma(\sigma_{x'}p_{x'}p_{y'}^2 - \sigma_{y'}p_{y'}p_{x'}^2).$$

In this equation, β is the Dresselhaus spin-orbit parameter, and gives the strength of the term that is linear in momentum.

In spin relaxation, the contribution of the spin-orbit terms that are linear in momentum dominate the contribution from the cubic terms [46]. So for the work discussed in this thesis, it is sufficient to consider the spin-orbit Hamiltonian

$$H_{SO} = \alpha(p_{x'}\sigma_{y'} - p_{y'}\sigma_{x'}) + \beta(p_{y'}\sigma_{y'} - p_{x'}\sigma_{x'}).$$

This Hamiltonian is written with respect to the GaAs crystalline axes. However the natural x and y axes of the dot are rotated with respect to the crystalline axes, and are aligned along the [110] and [$\bar{1}$10] axes, respectively, as shown in Fig. 4-10(a). We re-write H_{SO} in terms of these axes using the transformations

$$
\begin{aligned}
p_{x'} &= \cos(\theta)p_x - \sin(\theta)p_y & \sigma_{x'} &= \cos(\theta)\sigma_x - \sin(\theta)\sigma_y \\
p_{y'} &= \sin(\theta)p_x + \cos(\theta)p_y & \sigma_{y'} &= \sin(\theta)\sigma_x + \cos(\theta)\sigma_y
\end{aligned}
$$

with $\theta = \pi/4$. This gives the Hamiltonian:

$$H_{SO} = (\beta - \alpha)p_y\sigma_x + (\beta + \alpha)p_x\sigma_y. \tag{6.1}$$

Finally, two useful quantities that describe the strength of the spin-orbit inter-

action are the length scales $\lambda_+ = \hbar/(m^*(\beta + \alpha))$ and $\lambda_- = \hbar/(m^*(\beta - \alpha))$ [46]. Physically, these length scales represent the distance an electron has to travel in the x or y direction, respectively, for its spin to rotate by a certain angle φ [118]; for our definition of $\lambda_\pm$ this angle is $\varphi = 2$ radians. To see this, we consider an electron moving along the y-axis, so that $p_x = 0$ and $H_{SO} = (\beta - \alpha)p_y\sigma_x$. We compare this to the Hamiltonian for the interaction between a magnetic field and a spin given by $H = \frac{g\mu_B}{\hbar}\mathbf{B}\cdot\mathbf{S}$ and we see that the spin-orbit interaction acts like an effective magnetic field $\mathbf{B_{SO}} = \frac{2(\beta-\alpha)}{|g|\mu_B}p_y\hat{x}$ along the x-axis. The spin will precess around this field with frequency $\omega = |g|\mu_B B_{SO}/\hbar = 2(\beta - \alpha)p_y/\hbar$. The net precession angle during a time t is given by $\varphi = \omega t = 2(\beta - \alpha)m^*L/\hbar$, where $L = v_y t$ is the distance the electron travels in time t. Then $\varphi = 2L/\lambda_-$, which implies that the spin rotates by 2 radians over the length scale given by $L = \lambda_-$. The stronger the spin-orbit interaction, the shorter this distance will be.

6.1.2 Spin-orbit mediated coupling to piezoelectric phonons

An electron in a quantum dot can exchange energy with its environment by interacting with phonons via the piezoelectric and deformation potential electron-phonon interactions [121]. Phonons couple different orbital states of the dot, and these interactions are responsible for the very short relaxation times ($\lesssim 10$ ns) between the excited and ground orbital states [95, 96]. While phonons couple different orbital states of the dot, they cannot couple different spin states (Fig. 6-1(b)). Coupling between spin states is mediated by the SOI, which mixes the Zeeman split ground orbital state with excited orbital states of the opposite spin [45], as illustrated in Fig. 6-1(c). This allows phonons to induce spin relaxation. Because the phonon coupling to the spin states must be mediated by the SOI, the spin relaxation rates we measure in Chapter 5 are much slower than the orbital relaxation rates. Another difference between orbital and spin relaxation is the type of phonon involved. For orbital relaxation, which has a typical energy scale of 1 meV, deformation potential phonons are the dominant mechanism. For the range of magnetic fields we study in this thesis, the Zeeman energy Δ is of order 100 μeV, and on this energy scale

(a)
B = 0
H_{SO}= 0

(b)
B ≠ 0
H_{SO}= 0

(c)
B ≠ 0
H_{SO} ≠ 0

$|g\downarrow\rangle$

$|g\downarrow\rangle_{SO} = |g\downarrow\rangle + \varepsilon_- |e\uparrow\rangle +...$

$|g\rangle$

$|g\uparrow\rangle$

$|g\uparrow\rangle_{SO} = |g\uparrow\rangle + \varepsilon_+ |e\downarrow\rangle +...$
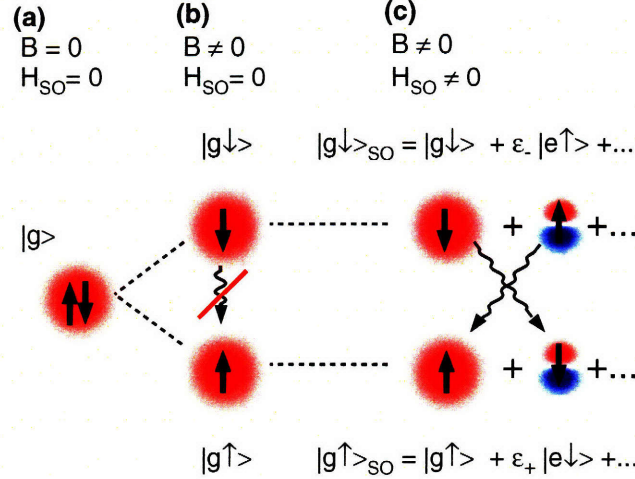
Figure 6-1: (a) At $B = 0$ and with no SOI, the spin-↑ and spin-↓ states of the ground orbital state $|g\rangle$ are degenerate. (b) Applying a magnetic field splits the spin states but phonon coupling between $|g\uparrow\rangle$ and $|g\downarrow\rangle$ is prohibited. (c) The SOI acts as a perturbation and mixes the orbital and spin states: the perturbed spin states $|g\uparrow\rangle_{SO}$ and $|g\downarrow\rangle_{SO}$ contain excited orbital states ($|e\rangle$) of the opposite spin so the perturbed states can be coupled by phonons.

piezoelectric phonons are primarily responsible for spin relaxation [46].

We can describe the SOI mediated mixing using perturbation theory. We have

$$\varepsilon_+ = \frac{\langle e\downarrow|H_{SO}|g\uparrow\rangle}{\hbar\omega_0 + \Delta} \qquad \text{and} \qquad \varepsilon_- = \frac{\langle e\uparrow|H_{SO}|g\downarrow\rangle}{\hbar\omega_0 - \Delta}$$

where $\hbar\omega_0$ is the energy of the excited orbital state $|e\rangle$ relative to the ground orbital state $|g\rangle$. We use this to understand the dependence of the spin relaxation rate W on $\hbar\omega_0$ and B. This is worked out in detail in Appendix C, but approximately we have $\langle e\downarrow|H_{SO}|g\uparrow\rangle \sim \langle e\uparrow|H_{SO}|g\downarrow\rangle \sim i\varepsilon_{SO}$, where ε_{SO} is real. The electron relaxes from the state $|g\downarrow\rangle_{SO}$ to $|g\uparrow\rangle_{SO}$ by emitting a phonon, and the matrix element for this transition is

$$M =_{SO} \langle g\downarrow|U_{ph}|g\uparrow\rangle_{SO} \sim i\langle U_{ph}\rangle \frac{\varepsilon_{SO}}{\hbar\omega_0} \left(\frac{1}{1 + \frac{\Delta}{\hbar\omega_0}} - \frac{1}{1 - \frac{\Delta}{\hbar\omega_0}} \right)$$

where $\langle U_{ph}\rangle \sim \langle e|U_{ph}|g\rangle \sim \langle g|U_{ph}|e\rangle$ describes how piezoelectric phonons couple the ground and excited orbital states of the dot.
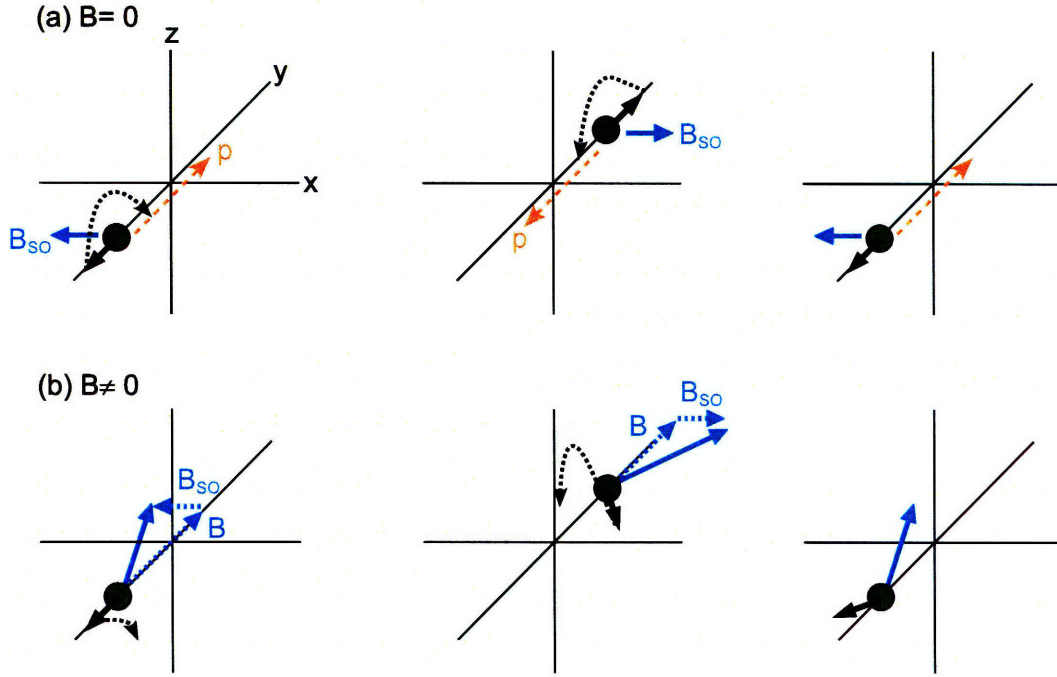
Figure 6-2: (a) An oscillating electron in zero external field. The electron's spin precesses around the effective magnetic field $\mathbf{B_{SO}}$ caused by the SOI. The SOI is time reversal invariant, so $\mathbf{B_{SO}}$ reverses its direction when the electron reverses its momentum $\mathbf{p}$. As a result, there is no net precession of the spin. (b) An external field B breaks time reversal symmetry and allows the oscillation to induce a net spin precession.

An important feature of the matrix element is that $M \to 0$ as $B \to 0$. This is called van Vleck cancellation and is a consequence of the time reversal invariance of the spin-orbit interaction [45, 108, 122]. An intuitive picture for this effect is given by Hanson *et al.* [108]. Suppose a phonon causes the electron to oscillate along the y-axis, as illustrated in Fig. 6-2(a). Then $H_{SO} = (\beta - \alpha)p_y\sigma_x$ and the electron will feel an effective magnetic field $\mathbf{B_{SO}} = \frac{2(\beta-\alpha)}{|g|\mu_B}p_y\hat{\boldsymbol{x}}$ along the x-axis from the SOI. If the external magnetic field $B = 0$, then the electron's spin will precess around $\mathbf{B_{SO}}$. The key point is that because the direction of $\mathbf{B_{SO}}$ depends on the electron's momentum, any spin rotation caused by the electron moving in one direction along the y-axis is reversed when the electron moves back in the opposite direction, as illustrated in Fig. 6-2(a). So with $B = 0$, the oscillation induced by the phonon produces no net

110

change in the direction of the electron's spin.

This is not the case if there is an external magnetic field **B**. Then the electron's spin precesses around the vector sum of **B** and **B$_{SO}$** as illustrated in Fig. 6-2(b). When the electron reverses its motion, **B$_{SO}$** reverses directions, but **B** does not, so the electron's spin does not precess back to its original position. This picture illustrates how controlled oscillations of an electron can be used to manipulate its spin via the SOI: this type of manipulation is called electron-dipole spin resonance [123, 124, 125]. However, since piezoelectric phonons in the environment of the dot are incoherent, this mechanism leads to spin relaxation.

Returning to the matrix element M, we take the limit $\Delta \ll \hbar\omega_0$ since the Zeeman splitting is much smaller than the energies of the excited orbital states. Then we have

$$M \propto \langle U_{ph} \rangle \frac{\varepsilon_{SO}}{\hbar\omega_0} \frac{\Delta}{\hbar\omega_0} \propto \omega^{1/2} \Delta \lambda_{SO}^{-1} (\hbar\omega_0)^{-2}$$

where ω is the frequency of the emitted phonon and $\epsilon_{SO} \propto \lambda_{SO}^{-1}$. We also use $\langle U_{ph} \rangle \propto \omega^{1/2}$, which comes from the form of the piezoelectric electron-phonon interaction in GaAs [45] (see Appendices A.4 and C for details). The spin relaxation rate is given by Fermi's golden rule: $W = \frac{2\pi}{\hbar} |M|^2 D_{ph}(\omega)$ where $D_{ph}(\omega) \propto \omega^2$ is the density of phonon states at the frequency of the emitted phonon. Then $W \propto \omega^3 \Delta^2 \lambda_{SO}^{-2} (\hbar\omega_0)^{-4} \propto \Delta^5 \lambda_{SO}^{-2} (\hbar\omega_0)^{-4}$ because energy conservation requires that the emitted phonon have energy $\hbar\omega = \Delta$. More precisely we have

$$W = A \frac{B^5}{\lambda_{SO}^2 (\hbar\omega_0)^4} \tag{6.2}$$

where, $A = 33 \text{ s}^{-1}\text{meV}^4\mu\text{m}^2/\text{T}^5$ depends on the g-factor of the dot and phonon parameters in GaAs[1].

From the arguments presented above, we see that the B^5 dependence of W is

---

[1]For the g-factor we use $|g| = 0.38$, which is the average of the measurements in Sections 2.4 and 4.4.2. The uncertainty in $|g|$ is accounted for in the error on the parameters we extract from the fits in Section 6.3. The phonon parameters we use are from Golovach et $al.$ [46] and they are effective mass $m^* = 0.067$, dielectric constant $\kappa = 13.1$, crystal density $\rho_c = 5.3$ g/cm^3, sound velocities $v_t = 3.35 \times 10^3$ m/s and $v_l = 4.73 \times 10^3$ m/s, piezoelectric constant $h_{14} = -0.16$ C/m^2 and deformation potential $\xi_0 = 6.7$ eV.

111

characteristic of the mechanism of SOI mediated coupling to piezoelectric phonons: two powers of B come from the time reversal invariance of the SOI in the matrix element, two powers come from the phonon density of states, and the final power comes from the form of the piezoelectric electron-phonon interaction. Another important feature of Eqn. 6.2 is that W depends sensitively on the energies of the excited orbital states. The lower the energies of the excited orbital states, the more effective the SOI is at mixing excited states of opposite spin into the Zeeman split ground orbital state. The spectrum of excited orbital states of a quantum dot is determined by the shape of its confining potential, which we can control electrically as we discuss in the next section.

6.2 Controlling the orbital states of the dot

Varying the voltage applied to the gates allows us to manipulate the electrostatic confining potential of the dot and hence its orbital states. We model the electrostatic potential of the dot with an anisotropic harmonic oscillator potential $U(x, y) = \frac{1}{2}m^*\omega_x^2 x^2 + \frac{1}{2}m^*\omega_y^2 y^2$. When the voltages on all the gates that form the dot are roughly equal, one expects from the geometry of the gates that the dot is less confined along the x-axis than along the y-axis, as illustrated by the black solid ellipse in Fig. 6-3(a). The energies of the excited orbital states relative to the ground state are determined by confinement: the lowest lying excited state is at energy $E_x = \hbar\omega_x$ above the ground state, while the next higher excited state has $E_y = \hbar\omega_y$ (assuming $E_y < 2E_x$).

To change the shape of the dot, we simultaneously change the voltage on 4 gates: we apply a more negative voltage to SG1 and apply a less negative voltage to the gates LP1, PL, and LP2. These changes are balanced to keep the ground state energy constant. The more negative voltage on SG1 pushes the dot toward SG2 and increases confinement along x, while the less negative voltages on LP1, PL, and LP2 reduces confinement along y. The net effect of these changes are illustrated by the white dotted ellipse in Fig. 6-3(a). We use the parameter V_{shape} to indicate a set of gate voltages $(V_{SG1}, V_{LP1}, V_{PL}, V_{LP2})$. Numerically, V_{shape} takes the value of V_{SG1} for the

112
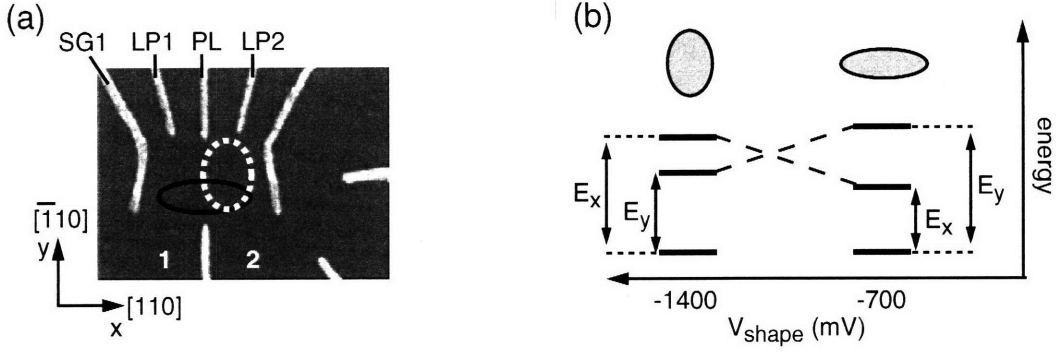
Figure 6-3: (a) Electron micrograph of the gate geometry. To change the shape of the confining potential, we change the voltages on the labeled gates. The black solid (white dotted) ellipse illustrates the expected dot shape for less (more) negative V_{shape}. The magnetic field is parallel to the y-axis and all voltage pulses are applied to gate LP2. For all the work in this chapter, we set the voltages so that the tunneling rate to lead 1 is negligible compared to that to lead 2. (b) The energies of the orbital excited states of the dot as a function of V_{shape}.

set. From these geometric considerations, we expect E_x to increase and E_y to decrease as V_{shape} is made more negative, as illustrated in Fig. 6-3(b).

At each V_{shape} we measure the energies of the excited orbital states using a three step pulse sequence, shown in Figs. 6-4(a)-(c), with $B = 0$. After ionizing the dot (Fig. 6-4(a)), we apply a voltage pulse V_p to gate LP2 to bring the ground orbital state an energy $E_p = e\alpha_{LP2}V_p$ below the Fermi energy of the lead (Fig. 6-4(b)). We apply this pulse for time t_p that is short (15 μs $< t_p <$ 400 μs) compared to the average tunneling time into the ground orbital state ($\approx$ 10 ms near the Fermi energy). For such a short pulse time, the probability for tunneling into the ground orbital state is small. However, for sufficiently large V_p, one or more excited orbital states will be below the Fermi energy of the lead. These states are more strongly coupled to the lead than the ground orbital state [53, 80], and an electron can tunnel onto the dot with rate Γ_{on}. Once it has tunneled into an excited orbital state, the electron quickly decays to the ground orbital state [95, 96] by emitting a phonon.

The third and final step is to bring the dot to the read-out state (Fig. 6-4(c)), where the ground state is just below the Fermi energy of the leads. If the dot is still ionized then an electron tunnels onto the dot during the read-out step (top diagram in
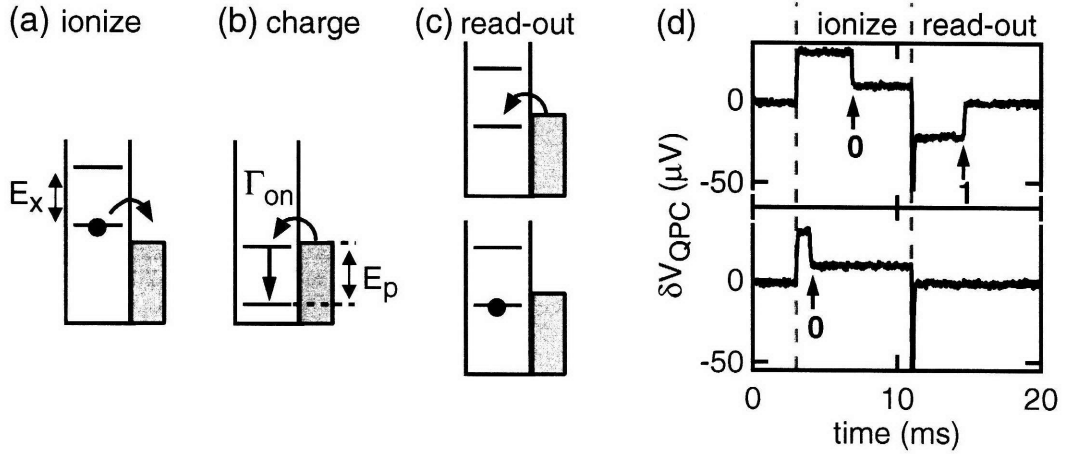
Figure 6-4: (a)-(c) Three step pulse sequence for measuring the energies of the excited orbital states. (d) Examples of real-time data. The direct capacitive coupling to the pulsed gate causes the QPC to respond to the pulse sequence; electron tunneling events are evident on top of this response. The 0's denote when an electron tunnels off the dot, while 1's denote when an electron tunnels on. The charging pulse ($t_p = 50~\mu s$ for this example) appears as a sharp spike between the ionization and read-out periods.

Fig. 6-4(c)), and we observe this with our real-time charge detection system (top panel of Fig. 6-4(d)). However, if an electron tunnels into the dot during the charging pulse, then no electron tunnels on during the read-out step (bottom diagram in Fig. 6-4(c)), and we observe no tunneling event in the read-out state (bottom panel of Fig. 6-4(d)).

To measure Γ_{on} at a given V_p, we repeat this pulse sequence the same number of times for several different values of t_p and count the number of times N_{ion} that the dot is still ionized after the charging pulse. An example of N_{ion} vs t_p is shown in Fig. 6-5(a). N_{ion} decreases exponentially and the rate of decrease gives Γ_{on}. Figure 6-5(b) shows Γ_{on} as a function of V_p: the two large increases in the rate are at the pulse voltages at which an excited orbital state crosses the Fermi energy (the positions are marked with the dashed vertical lines).

To convert the positions of the increases in Γ_{on} into the energies of the excited orbital states, we need to measure α_{LP2}, which relates the voltage pulse to the resultant change in the energies of the states of the dot by $E_p = e\alpha_{LP2}V_p$. To do this, we measure the average time an electron spends on (τ_{on}) and off (τ_{off}) the dot

114
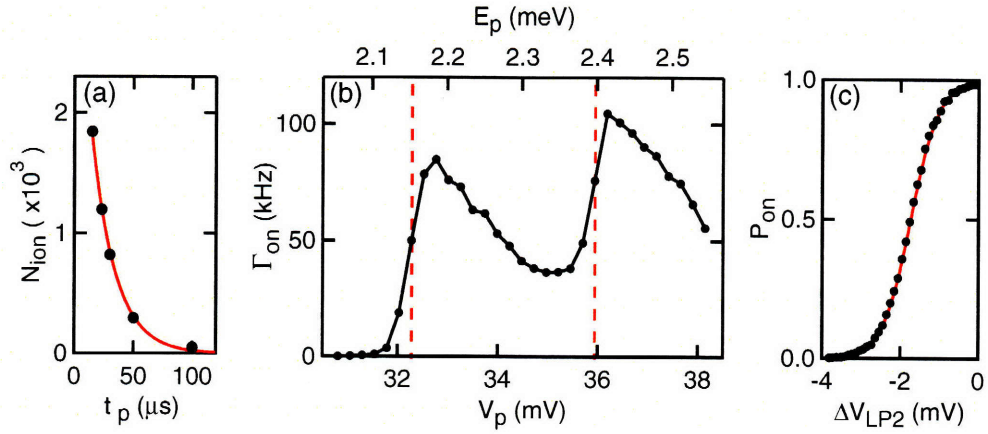
Figure 6-5: (a) The number of events N_{ion} as a function of t_p. The solid line is a fit discussed in the text. (b) Γ_{on} vs V_p for $V_{shape} = -850$ mV. The two sharp rises marked by the dashed vertical lines occur at pulse voltages where an excited state crosses the Fermi energy. (c) P_{on} vs ΔV_{LP2} at $T = 280$ mK. The solid line is a fit to the Fermi function to extract α_{LP2} as discussed in the text.
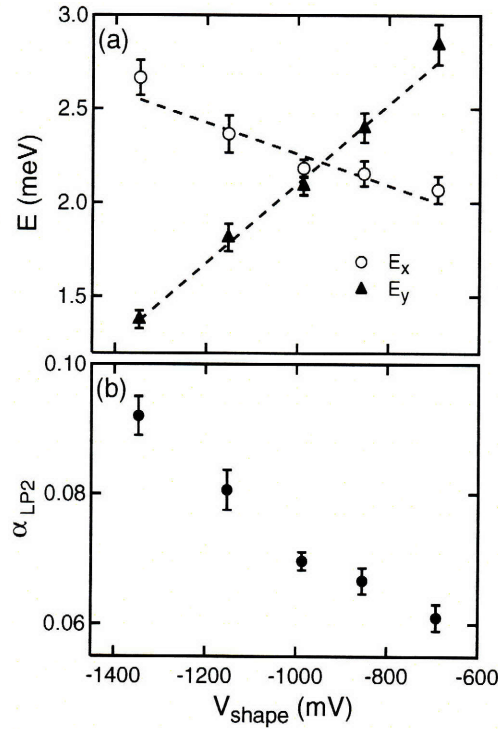
Figure 6-6: (a) Energies of the excited orbital states and (b) α_{LP2} as a function of V_{shape}. The dashed lines in (a) are linear fits discussed in the text.

as gate LP2 is made more negative and the ground state is swept from below to above the Fermi energy of the lead. Then from Section 4.1. $P_{on} = \tau_{on}/(\tau_{on} + \tau_{off}) = f(-e\alpha_{LP2}\Delta V_{LP2} + V_0)$. where $f(x) = (1 + e^{x/k_BT})^{-1}$ is the Fermi function. We perform these measurements at $T = 280$ mK so that the Fermi function is broader, which gives a more accurate measurement of α_{LP2}. Figure 6-5(c) shows an example of a measurement of P_{on} vs ΔV_{LP2} and a fit to determine α_{LP2}. Using this value, we convert V_p into E_p as shown on the top axis of Fig. 6-5(b). The energies of the excited states are given by the positions of the sharp increases in Γ_{on}.

We repeat this procedure for measuring the excited state energies at several values of V_{shape}. The results are shown in Fig. 6-6(a) and show one state increasing and one state decreasing in energy. This behavior is what we expect from the geometric considerations: as the confinement along x increases and along y decreases with more negative V_{shape}. the energy E_x of the x-excited state increases, while the energy E_y of the y-excited state decreases. allowing us to identify the x and y states as indicated in Fig. 6-6(a). The value of α_{LP2} as a function of V_{shape} is plotted in Fig. 6-6(b). We see that α_{LP2} increases with more negative V_{shape}, which is what we expect from the geometric considerations in Fig. 6-3(a). As V_{shape}. and hence V_{SG1}, is made more negative the dot is pushed toward LP2. More negative V_{shape} also corresponds to less negative V_{LP2}. which tends to reduce the confinement along y and bring the dot closer to LP2. These considerations lead us to expect that α_{LP2} should increase, as we observe.

6.3   Electrical control of the spin relaxation rate

At each V_{shape}. we measure $W \equiv T_1^{-1}$ at $B = 3$ T. The results are shown as a function of V_{shape} in the top panel of Fig. 6-7 and we see that we can vary W by over an order of magnitude. At each V_{shape} we also measure Δ at $B = 7.5$ T. For this measurement, we use the pulse sequence discussed in Section 4.4 to measure Γ_{on} vs V_p. The separation between the increases in Γ_{on} associated with the ground and excited spin states give Δ. and we extract this by fitting to Eqn. 4.14. We perform this

116
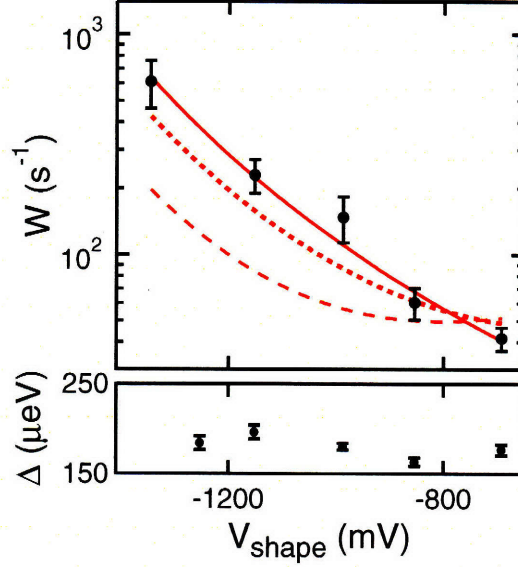
Figure 6-7: Top panel: W vs V_{shape} at $B = 3$ T. The solid, dotted, and dashed lines show fits with $A_x/A_y = 0.01, 0.25$ and 1, respectively. Bottom panel: Δ vs V_{shape} at $B = 7.5$ T.

measurement at $B = 7.5$ T because this is where Δ is largest, and can be measured most accurately. The results are shown in the bottom panel of Fig. 6-7, and from the data we see that Δ does not vary systematically with V_{shape}. This confirms that the variation in W with V_{shape} in Fig. 6-7 is not caused by changes in Δ. Thus the data in Fig. 6-7 demonstrate electrical control of W at constant Δ.

As we discuss in Section 6.1.1, the energies of the excited orbital states affect W because the higher the energies of the excited states, the weaker the SOI coupling to the ground state, hence the slower the relaxation rate. If we model W assuming the anisotropic 2-D harmonic oscillator potential $U(x, y)$, an in-plane magnetic field B, a SOI that is linear in the electron momentum, and a phonon wavelength much greater than the dot size (dipole approximation), then W has the form $W = A_x E_x^{-4} + A_y E_y^{-4}$ (full derivation presented in Appendix C). Here A_x and A_y describe the contribution of each orbital state to spin relaxation and $W \propto E^{-4}$ because of van Vleck cancellation [45].

We fit the data in Fig. 6-7 to this equation by approximating $E_x(V_{shape})$ and

$E_y(V_{shape})$ by the dashed lines shown in Fig. 6-6(a). The result is shown as the solid line in Fig. 6-7 and the fit gives $A_x/A_y = (0.9 \pm 5.6)\%$. To determine a limit on A_x/A_y we use this result, as well as the results of other fits where we use different estimates for the linear fits to $E_x(V_{shape})$ and $E_y(V_{shape})$. From these, we determine that $A_x/A_y < 14\%$, which implies that only the y-excited orbital state is contributing to spin relaxation. The dotted and dashed lines in Fig. 6-7 show fits with $A_x/A_y = 25\%$ and 100%, respectively. Clearly, these are not consistent with the data.

We can understand why the y-excited state dominates spin relaxation from the spin-orbit Hamiltonian $H_{SO} = (\beta - \alpha)p_y\sigma_x + (\beta + \alpha)p_x\sigma_y$. The magnetic field B is applied along the y-axis and so the spin-up and spin-down states are eigenstates of σ_y. But this implies that σ_y cannot couple states of opposite spin, as required for spin relaxation. Only the first term in H_{SO}, which is proportional to σ_x, can couple different spin states as in Fig. 6-1(c). Since the first term is proportional to p_y, a change in parity along the y-axis is also required. The x-excited state does not satisfy this requirement, so the $p_y\sigma_x$ term couples the Zeeman split ground orbital state to y-excited states of opposite spin. Alternatively, because the first term is proportional to p_y, only the energy scale for confinement in the y-direction, which is given by E_y, matters for spin relaxation. A consequence is that for $V_{shape} > -1000$ mV, it is the higher energy excited state that determines W, an unusual situation.

To compare to theory, Fig. 6-8 shows W as a function of E_y: here the directly measured values of E_y are used. In the limit where the phonon wavelength is much larger than the size of the dot, we have from Eqn. 6.2 that $W = AB^5E_y^{-1}\lambda_{SO}^{-2}$ where $A = 33 \text{ s}^{-1}\text{meV}^4\mu\text{m}^2/\text{T}^5$. Since only the first term in H_{SO} contributes to spin relaxation, we have $\lambda_{SO} = \lambda_- = \hbar/m^*|\beta - \alpha|$. We fit the data in Fig. 6-8 to the theoretical prediction by Golovach et al. [46] that includes the effects of the phonon wavelength being comparable to the size of the dot and obtain $\lambda_{SO} = 1.7 \pm 0.2 \mu$m, consistent with previous measurements of spin-orbit length scales in dots [106].

Spin relaxation also depends sensitively on the magnetic field [28] as shown in Fig. 6-9 for two different sets of gate voltages (these are the data from Fig. 5-9 and the inset). These data demonstrate electrical control of W over a range of fields.

118
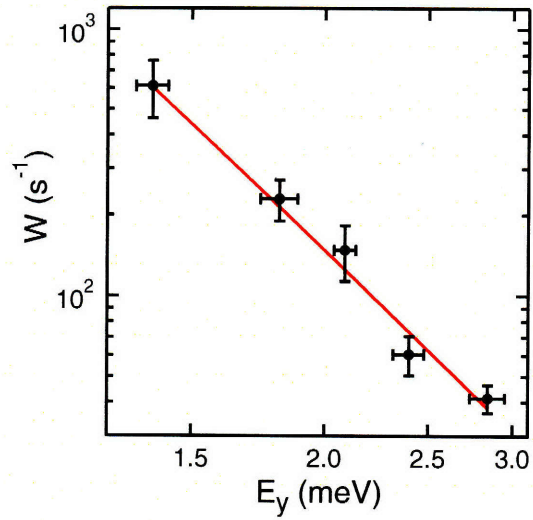
Figure 6-8: The same relaxation rate data as in Fig. 6-7, plotted as a function of the measured values of E_y from Fig. 6-6(a). The solid line is a fit to find the spin-orbit length as discussed in the text.
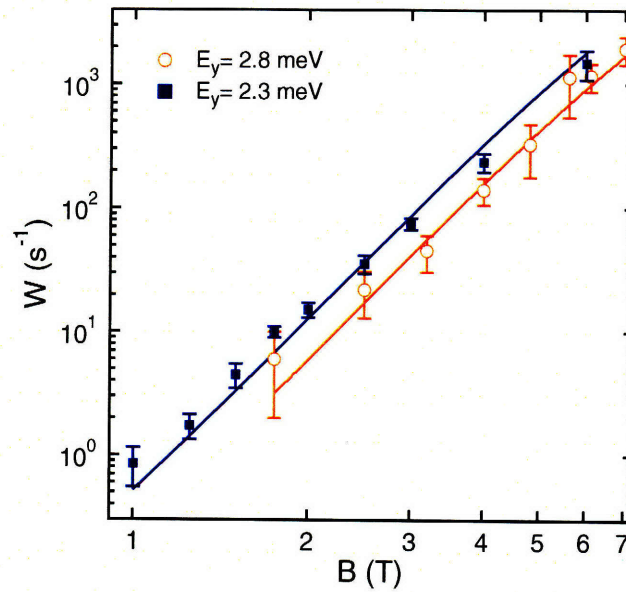
Figure 6-9: Spin relaxation rate as a function of magnetic field for two different sets of gate voltages. Solid lines are fits discussed in the text.

Using our value of $\lambda_{SO} = 1.7\ \mu m$, we independently estimate E_y for the two sets of gate voltages by fitting the data to the theory of Golovach $et\ al.$ [46]. The solid lines in Fig. 6-9 show the fit results, and we extract values of E_y consistent with what we expect for these gate voltages. Moreover, the agreement between our data and theory down to a field of 1 T demonstrates that spin-orbit mediated coupling to piezoelectric phonons is the dominant mechanism down to low fields, corresponding to very long spin relaxation times.

Chapter 7

Conclusions

In summary, we use real-time charge detection to measure electron tunneling and spin relaxation in a lateral quantum dot. First, we characterize our real-time charge detection system and find that it has a sensitivity of $2 \times 10^{-3}e/\text{Hz}^{1/2}$ and a bandwidth of 4 kHz. Our sensitivity is aided by the large size of our signal: an electron tunneling event causes a 10% change in the voltage across the QPC. However, the sensitivity is limited by both the amplifier noise and peaks in the noise spectrum from electrical pick-up and vibrations, and better sensitivity could be achieved using an amplifier with lower noise and improving the vibration and electrical isolation of the experiment. Using a cryogenic amplifier mounted near the sample would have the additional benefit of increasing the bandwidth by reducing the capacitance of the wires going to the amplifier.

For these measurements, we also develop a novel triggering system to identify events in real-time data, and compress the massive amounts of data we collect (20-65 gigabytes per day) by a factor of about 1000. This allows us to acquire good statistics in our measurements. We also develop a novel feedback system that correctly positions the states of the dot and maintains their stability. This allows us to perform a variety of measurements and to take data continuously for periods as long as 2 days.

Understanding electron tunneling in quantum dots is important for applications of quantum dots in spintronics, and other fields. Using real-time charge detection and gate pulsing techniques, we characterize the rate at which an electron tunnels

121

onto and off of the quantum dot in zero magnetic field. We find that the tunneling rates depend exponentially on the gate and drain-source bias voltages. We explain this exponential dependence with a model that assumes elastic tunneling, and accounts for the energies of the states in the dot relative to the heights of the tunnel barriers. A particular significant observation is that as an empty state is brought further below the Fermi energy of the leads, we find the rate for tunneling onto the dot decreases exponentially. This decrease occurs despite the increasing number of inelastic processes available; however, the decrease is consistent with the model that assumes purely elastic tunneling.

We also measure the rate for tunneling into an empty quantum dot in a magnetic field, where the spin states are split by the Zeeman energy. We find that the ratio of the rates for tunneling into the excited and ground spin states decreases with increasing magnetic field. However, by changing the orbital configuration of the dot, we can change the ratio and the ratio reaches a maximum when the dot is symmetric. We consider several possible explanations for these observations, but find that none of them can explain the spin-dependence of tunneling into the quantum dot.

Next, we measure the spin relaxation rate $W \equiv T_1^{-1}$ for a single electron in a lateral quantum dot in a magnetic field. Using our feedback system to maintain the stability of our read-out state and our triggering system to collect good statistics, we measure W at fields as low as 1 T, where the Zeeman splitting is comparable to temperature. At this field we find that $T_1 > 1$ s, which is very promising for applications of quantum dots in quantum computing and as spin memory [27, 28] in spintronics. We also measure W from 1 T up to 7 T, a range over which W varies by 3 orders of magnitude. The dependence of W on field is a power-law, and the power is characteristic of the spin relaxation mechanism. From our measurements, we determine that the dominant spin relaxation mechanism in lateral dos is spin-orbit mediated coupling to piezoelectric phonons.

Finally, we demonstrate *in-situ* electrical control over the spin relaxation rate in a lateral dot. This control is possible because spin relaxation requires that the spin-orbit interaction couple the Zeeman split ground orbital state to excited orbital states

of opposite spin, and this coupling depends on the energies of the excited states. By varying the voltages on the surface gates, we affect the confining potential of the dot, and hence the energies of the orbital states. We demonstrate that we can vary W by over an order of magnitude at fixed Δ, and that this variation depends only on the confinement of the electron wavefunction in the direction along the applied in-plane magnetic field, as predicted by theory. From these data we extract the spin-orbit length, which describes the strength of the spin-orbit interaction in GaAs.

The results in this thesis point toward several directions for future work. Our observation of spin-dependent tunneling into an empty dot, taken in conjunction with measurements by Potok *et al.* [55] of the lack of spin polarization of electrons emitted from a quantum dot in a magnetic field, suggest that the spin physics of tunneling in quantum dots is not yet understood. Further experimental studies of electron tunneling in a magnetic field are needed to help determine the underlying cause of these effects. Developing a theory to explain the experimental observations could have important implications for applications of dots in spintronics. It could also have implications for quantum computation, where spin-dependent tunneling could affect the initialization of a quantum dot qubit.

There is also more work to be done characterizing spin relaxation in quantum dots. The Rashba and Dresselhaus spin-orbit interactions have different forms, and this causes the spin relaxation rate W to vary as we change the orientation of the in-plane magnetic field with respect to the GaAs crystalline axes [46]. For some orientations of the field, the Rashba and Dresselhaus interactions cooperate, and W is at a maximum. For other orientations, the interactions oppose one another, and the relaxation rate is at a minimum. If the Rashba and Dresselhaus parameters are equal, then the two interactions can cancel one another at the minimum, and the spin relaxation would become dominated by other mechanisms, such as hyperfine coupling to phonons. *A priori* the Rashba and Dresselhaus parameters are not necessarily equal. However, experiments have demonstrated gate control over the spin-orbit interaction [126], so it may be possible to tune these parameters to be equal.

Appendix A

Spin Relaxation Mechanisms

A.1 General approach to spin relaxation

The purpose of this appendix is to motivate the dependence of the spin relaxation rate on magnetic field and confinement potential of the dot for different possible relaxation mechanisms. Consequently, the treatment in this appendix will not be rigorous; rather we will seek to capture the essential elements necessary to understand the physics behind the mechanisms. Full treatments of the various mechanisms are given in the references [45, 46, 47, 48, 111, 112], and we consider one mechanism in great detail in Appendix C.

In magnetic fields B that are on the order of the effective nuclear field B_{nuc} caused by the nuclear spins, relaxation proceeds through the hyperfine interaction between the electrons's spin and the nuclear spins [37, 41]. However, at fields $B \gg B_{nuc}$, the Zeeman splitting of the electron is much greater than that of the nuclei, and this mechanism is suppressed, so other mechanisms dominate spin relaxation. In general, these other mechanisms involve two types of interactions. One type of interaction is responsible for absorbing the energy released when the electron flips its spin. Since electrons are charged, electrical fluctuations from phonons and ohmic fluctuations couple very strongly to the electron's charge distribution (which is essentially the orbital part of the electron's wavefunction), and are good candidates for absorbing the energy. However while electrical fluctuations can couple orbital states, they do

not couple directly to spin and cannot induce a spin-flip. Consequently, another interaction is needed to couple the electron's orbital states to its spin states, thus mediating spin relaxation. Two interactions that can couple orbital and spin states are the spin-orbit and hyperfine interaction.

To describe these mechanisms quantitatively, we can write the Hamiltonian for the system as [47]:

$$H = \underbrace{\frac{p^2}{2m^*} + \frac{1}{2}m^*\omega_0^2(x^2 + y^2) + -\frac{1}{2}\Delta\sigma_y + V_{SF} + U_E}_{H_0}$$

Here U_E describes the source of electrical fluctuations (phonons, gate or ohmic fluctuations, etc), V_{SF} describes the interaction responsible for coupling states of opposite spin (hyperfine interaction or spin-orbit interaction), and ω_0 describes the confinement potential. The eigenstates of H_0 are $|n, s\rangle$ where n is the index of the harmonic oscillator states with energy $E_n = (n + 1)\hbar\omega_0$ and s is the spin state (we ignore the orbital index m). The higher energy spin-down state and the lower energy spin-up state are separated by the Zeeman energy $\Delta = |g|\mu_B B$. We can account for the effects of V_{SF} using perturbation theory [45, 47]:

$$|0 \uparrow\rangle_{eff} = |0 \uparrow\rangle + \sum_{n,s} \frac{|n, s\rangle\langle n, s|V_{SF}|0 \uparrow\rangle}{E_{0\uparrow} - E_{n,s}}$$

and

$$|0 \downarrow\rangle_{eff} = |0 \downarrow\rangle + \sum_{n,s} \frac{|n, s\rangle\langle n, s|V_{SF}|0 \downarrow\rangle}{E_{0\downarrow} - E_{n,s}}$$

To first order in V_{SF} the matrix element for a spin-flip transition caused by coupling to electrical fluctuations is [45, 47]:

$$\begin{aligned}
M &= {}_{eff}\langle 0 \downarrow|U_E|0 \uparrow\rangle_{eff} \\
&= \langle 0 \downarrow|U_E|0 \uparrow\rangle \\
&\quad + \sum_{n,s} \frac{\langle 0 \downarrow|U_E|n, s\rangle\langle n, s|V_{SF}|0 \uparrow\rangle}{E_{0\uparrow} - E_{n,s}} + \sum_{n,s} \frac{\langle 0 \downarrow|V_{SF}|n, s\rangle\langle n, s|U_E|0 \uparrow\rangle}{E_{0\downarrow} - E_{n,s}}
\end{aligned}$$

126

The electrical fluctuations cannot cause a spin-flip, so $\langle 0 \downarrow |U_E|0 \uparrow \rangle = 0$ and

$$M = \sum_n \frac{\langle 0 \downarrow |U_E|n \downarrow \rangle \langle n \downarrow |V_{SF}|0 \uparrow \rangle}{E_{0\uparrow} - E_{n\downarrow}} + \frac{\langle 0 \downarrow |V_{SF}|n \uparrow \rangle \langle n \uparrow |U_E|0 \uparrow \rangle}{E_{0\downarrow} - E_{n\uparrow}}$$

In the dipole approximation we have that $U_E \propto E_\omega . r$ where E_ω is the electric field for fluctuations at frequency $\omega = \Delta/\hbar$ and $\Delta = |g|\mu_B B$. Also, for a harmonic confining potential $\langle n|x|0 \rangle \neq 0$ for $n = 1$ and is 0 otherwise, so

$$M \propto E_\omega \underbrace{\left(\frac{\langle 0|x|1 \rangle \langle 1 \downarrow |V_{SF}|0 \uparrow \rangle}{\hbar\omega_0 + \Delta} + \frac{\langle 0 \downarrow |V_{SF}|1 \uparrow \rangle \langle 1|x|0 \rangle}{\hbar\omega_0 - \Delta} \right)}_{\xi}$$

Let us denote the terms in the parentheses in the above expression by ξ. At $T = 0$ the electron will relax from the excited spin-down state to the ground spin-up state through spontaneous emission (we consider the effects of finite temperature in the last section). The rate W_0 is given by Fermi's Golden rule [45, 47]:

$$W_0 = \frac{2\pi}{\hbar^2}|M|^2 \mathcal{D}(\omega) \propto E_\omega^2 |\xi|^2 \mathcal{D}(\omega)$$

where $\mathcal{D}(\omega)$ denotes the density of states at frequency ω for the electrical fluctuations. The spectrum of electrical fluctuations $S(\omega) = E_\omega^2 \mathcal{D}(\omega)$ [47, 48] and so we have

$$W_0 \propto |\xi|^2 S(\omega) \tag{A.1}$$

The advantage of expressing spin-relaxation in terms of ξ and S is that the magnetic field and confining potential dependence of ξ is determined by V_{SF}, while that of S is determined by the electrical fluctuations U_E. We now consider these terms in greater detail.

A.2   Hyperfine interaction

The hyperfine interaction is caused when the spin of the electron on the dot interacts with the spins of the Ga and As nuclei [38, 37, 39, 41, 40]. The wavefunction of the dot electron is spread out over N nuclei, and $N = n_{nuclei} A d$, where n_{nuclei} is the density of nuclei, d is the depth of the 2DEG, and $A \propto x^2$ is the area of the dot [41]. The electron's spin interacts with the average nuclear field, and fluctuations in this field can induce spin-flips in the dot. The fluctuations are on the order of $V_{HF} \propto (C_{HF}/N^{1/2})\sigma$, where C_{HF} is the hyperfine coupling constant and σ represents the Pauli sigma matrices (we don't worry about the index of the matrix here. The details are worked out in the references). But $N^{-1/2} \propto A^{-1/2} \propto x^{-1}$ and so we have

$$\xi_{HF} \propto \frac{\langle 0|x|1\rangle \langle 1|\frac{1}{x}|0\rangle}{\hbar\omega_0 + \Delta} + \frac{\langle 0|\frac{1}{x}|1\rangle \langle 1|x|0\rangle}{\hbar\omega_0 - \Delta}$$

We note that $\langle 0|x|1\rangle \propto (\hbar\omega_0)^{-1/2}$, $\langle 1|\frac{1}{x}|0\rangle \propto (\hbar\omega_0)^{1/2}$, and similarly for the other terms. Then using the fact that $\Delta \ll \hbar\omega_0$, we have

$$\xi_{HF} \propto \frac{1}{\hbar\omega_0} \tag{A.2}$$

A.3   Spin-orbit interaction

The spin-orbit interaction is a relativistic effect that is caused by the electron's motion through electric fields intrinsic to the semiconductor heterostructure [119, 116]. This interaction is discussed in greater detail in Section 6.1.1. We approximate $V_{SF} \propto p\sigma$ and we have

$$\xi_{SO} \propto \langle \downarrow|\sigma|\uparrow\rangle \left(\frac{\langle 0|x|1\rangle \langle 1|p|0\rangle}{\hbar\omega_0 + \Delta} + \frac{\langle 0|p|1\rangle \langle 1|x|0\rangle}{\hbar\omega_0 - \Delta} \right)$$

For a harmonic oscillator potential $\langle 0|x|1\rangle = \langle 1|x|0\rangle \propto \omega_0^{-1/2}$ and $\langle 1|p|0\rangle \propto \omega_0^{1/2}$. But $\langle 0|p|1\rangle = -\langle 1|p|0\rangle$ and so we have

$$\xi_{SO} \propto \frac{1}{\hbar\omega_0 + \Delta} - \frac{1}{\hbar\omega_0 - \Delta}$$

Here we drop the term $\langle\downarrow|\sigma|\uparrow\rangle$ because it does not depend on the confinement potential or the magnitude of the magnetic field. In this equation, we note that $\xi_{SO} = 0$ at $B = 0$. This is known as van Vleck cancellation [45] and is caused by the time-reversal invariance of the spin-orbit interaction. This is discussed in more detail in Section 6.1.2. For $\Delta \ll \hbar\omega_0$, we have

$$\xi_{SO} \propto \frac{\Delta}{(\hbar\omega_0)^2}.$$ (A.3)

A.4 Piezoelectric phonons

One source of electrical fluctuations is from phonons via the piezoelectric interaction [121]. The piezoelectric electron-phonon interaction has the form

$$U_E \propto \omega^{-1/2} e^{i(\mathbf{q}\mathbf{r} - \omega t)}$$

where we neglect angular factors (these are considered explicitly in Appendix C). Then the magnitude of the oscillating electric field is

$$E_\omega \propto |-\nabla U_E| \propto q\omega^{-1/2} \propto \omega^{1/2}$$

where this last proportionality follows from $q \propto \omega$. For phonons, the density of states is given by $\mathcal{D}(\omega) \propto \omega^2$ and so we have

$$S_{ph}(\omega) \propto |E_\omega|^2 \mathcal{D}(\omega) \propto \omega^3$$

and using $\omega \propto \Delta$ gives [48]

$$S_{ph} \propto \Delta^3.$$ (A.4)

Another type of electron-phonon interaction is through the deformation potential. For the range of Δ studied in this thesis, the contribution of deformation potential phonons should be small.

A.5 Ohmic fluctuations

Another source of electrical fluctuations are the voltage fluctuations intrinsic to a conductor, and these will be present on the gates and ohmic leads [47, 48]. These fluctuations are called 'ohmic' fluctuations and are described by the fluctuation-dissipation theorem. From this we can obtain [48]

$$S_{ohmic}(\omega) \propto R\hbar\omega$$

where R describes the impedance of the conductor. To gain some intuition. we note that at finite temperature the density of emitted electrical fluctuations is given by $S_{ohmic}(\omega)n(\hbar\omega)$, where $n(\hbar\omega) = (e^{(\hbar\omega/k_BT)}-1)^{-1}$ is the Bose occupation factor. Notice that in the limit $\hbar\omega \ll k_BT$, we have $S_{ohmic}(\omega)n(\omega) \propto Rk_BT$. which is what we expect for the intrinsic Johnson noise of a conductor. For now, we continue to consider $T = 0$ and so we have

$$S_{ohmic} \propto \Delta \tag{A.5}$$

where we use $\hbar\omega = \Delta$. Note that in certain limits, the electrical fluctuations from the QPC are also described by ohmic fluctuations [111].

A.6 Results at $T = 0$

Having evaluated ξ and S for different mechanisms, we can now use Eqn. A.1 to combine these pieces to find the dependence of W_0 on magnetic field and confinement potential for several different mechanisms. These results are summarized in table A.1.

Mechanism	W_0
hyperfine coupling to phonons	$\Delta^3(\hbar\omega_0)^{-2}$
hyperfine coupling to ohmic fluctuations	$\Delta(\hbar\omega_0)^{-2}$
spin-orbit coupling to phonons	$\Delta^5(\hbar\omega_0)^{-4}$
spin-orbit coupling to ohmic fluctuations	$\Delta^3(\hbar\omega_0)^{-4}$

Table A.1: This table gives the dependence of the spin relaxation rate on magnetic field $B = \Delta/|g|\mu_B$ and confinement potential $\hbar\omega_0$ for a variety of possible relaxation mechanisms. Here phonons refer to piezoelectric phonons. At high fields, spin-orbit coupling to piezoelectric phonons dominates, while at low fields other mechanisms may contribute.

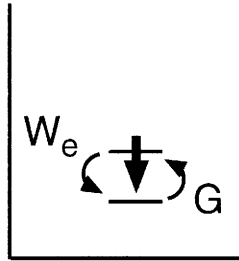# A.7 Effect of finite temperature

Figure A-1: Transition rates that establish thermal equilibrium in a quantum dot decoupled from its leads.

We now consider the effects of finite temperature on the spin relaxation rate. We consider an electron confined in a quantum dot that is not coupled to its leads, as illustrated in Fig. A-1. The transition rate from the excited spin-down state to the

131

ground spin-up state is W_e and the reverse rate from the spin-up state to the spin-down state is G. At $T = 0$, the electron can relax from the spin-down to the spin-up state through the spontaneous emission of an electrical fluctuation, however, it cannot absorb energy and transition from spin-up to spin-down. Thus $W_e = W_0$ and $G = 0$. At finite T, the transition rates are given by the familiar formulas for absorption and emission [45]: $G = W_0 n(\Delta)$ for stimulated absorption and $W_e = W_0(1 + n(\Delta))$ for spontaneous and stimulated emission, where $n(\Delta) = (e^{(\Delta/k_B T)} - 1)^{-1}$.

With these rates, the evolution of the probability for being in the spin-down state P_e is described by:

$$\dot{P}_e = GP_g - W_e P_e$$

where P_g is the probability for being in the lower energy spin-up state. Since $P_g = 1 - P_e$ we have

$$\dot{P}_e = G - (W_e + G)P_e.$$

Solving this equation for P_e we obtain:

$$P_e(t) = \frac{G}{W_e + G} + \left(P_{e,0} - \frac{G}{W_e + G} \right) e^{-(W_e + G)t} \tag{A.6}$$

where $P_{e,0} = P_e(t = 0)$. From this equation we see that as $t \to \infty$ and the system reaches thermal equilibrium, $P_{e,\infty} = \frac{G}{W_e + G}$ and $P_{g,\infty} = 1 - P_{e,\infty} = \frac{W_e}{W_e + G}$. Then in thermal equilibrium we have $P_{e,\infty}/P_{g,\infty} = \frac{G}{W_e} = \frac{n(\Delta)}{1 + n(\Delta)} = e^{-\Delta/k_B T}$ as we expect.

From Eqn. A.6, we see that the timescale for reaching equilibrium is given by $W = W_e + G$ where $W \equiv T_1^{-1}$ is the spin relaxation rate. Then $W = W_0(2n(\Delta) + 1)$ and simplifying this gives

$$W = W_0 \coth(\Delta/2k_B T) \tag{A.7}$$

For $\Delta \gg k_B T$ we are in the $T = 0$ limit and $W = W_0$. For $\Delta \ll k_B T$ we have $W = W_0 \frac{2k_B T}{\Delta}$.

Appendix B

Probability calculations for spin relaxation measurements

B.1   Ionized and excited state probabilities
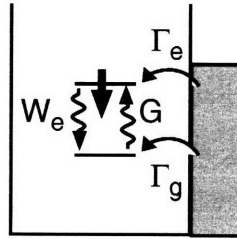
Figure B-1: Diagram of processes that can occur during the charging step of the spin relaxation measurement sequence.

In this section we consider in detail the processes that occur during the charging step of the spin-relaxation measurement pulse sequence discussed in Section 5.2. Before the charging step, both spin states are brought above the Fermi energy of the leads, so that any electron can tunnel off the dot, leaving the dot ionized. During the charging step, the spin states are brought below the Fermi energy of the leads and held in this configuration for a time t_w. During this time, electrons can tunnel into the excited and ground spin states with rates Γ_e and Γ_g respectively, as illustrated in Fig. B-1. We do not assume that $\Gamma_e = \Gamma_g$ *a-priori*, because we see in Section 4.4

that this is not always the case. Electrons can also transition from the excited spin state to the ground spin state with rate W_e, and the reverse process has rate G. Thus after waiting a time t_w, the dot can be in one of three possible states: there is some probability $P_i(t_w)$ that the dot is still ionized, there is some probability $P_e(t_w)$ that the electron is in the excited spin state, and finally there is some probability $P_g(t_w)$ that the electron is in the ground state. Note that $P_i + P_e + P_g = 1$. In this section, we will calculate $P_i(t_w)$ and $P_e(t_w)$.

The rate equation describing P_i is

$$\dot{P}_i = -(\Gamma_e + \Gamma_g)P_i.$$

We can solve this equation to get

$$P_i(t_w) = \epsilon_i e^{-\Gamma_t t_w} \tag{B.1}$$

where $\Gamma_t = \Gamma_e + \Gamma_g$ is the total rate at which electrons tunnel onto the quantum dot and $\epsilon_i = P_i(t_w = 0)$ is the ionization efficiency, which describes how effective the ionization pulse is at emptying the dot. Thus the probability that the dot remains empty decreases exponentially with increasing t_w.

Having found $P_i(t_w)$, we now consider P_e. The rate equation is given by

$$\begin{aligned} \dot{P}_e &= \Gamma_e P_i + G P_g - W_e P_e \\ &= (\Gamma_e - G)P_i - (W_e + G)P_e + G \end{aligned}$$

where we use $P_g = 1 - P_e - P_i$ to eliminate P_g from the equation. Substituting in Eqn. B.1 and solving for P_e gives

$$P_e(t_w) = P_{e,0} e^{-W t_w} + \frac{G}{W}(1 - e^{-W t_w}) + \frac{\epsilon_i(\Gamma_e - G)}{\Gamma_t - W}(e^{-W t_w} - e^{-\Gamma_t t_w}) \tag{B.2}$$

where $W = W_e + G$ is the spin relaxation rate and $P_{e,0} = P_e(t_w = 0)$. We note that $G/W = G/(G + W_e) = (1 + W_e/G)^{-1} = (1 + e^{\Delta/k_B T})^{-1}$, where we use the fact that

$W_e/G = e^{\Delta/k_B T}$ as shown in Appendix A.

We can simplify Eqn. B.2 further with some approximations. $P_{e,0}$ should be small because, before the ionization pulse, the dot is in thermal equilibrium and the probability the electron is in the excited spin state is approximately $e^{-\Delta/k_B T}$. When the ionization pulse is applied, most of these electrons should then tunnel off the dot. If we assume [1] that $\Gamma_{off,\uparrow} \sim \Gamma_{off,\downarrow}$, then we have $P_{e,0} \approx (1 - \epsilon_i)e^{-\Delta/k_B T}$. In our experiments $\epsilon_i \approx 0.95$ and at the lowest field of $B = 1$ T, $e^{-\Delta/k_B T} \approx 0.1$ so that $P_{e,0} \lesssim 5 \times 10^{-3}$. This is much smaller than the second term in equation Eqn. B.2 because $G/W = (1+e^{\Delta/k_B T})^{-1} > e^{-\Delta/k_B T}$, so we can neglect the first term in equation Eqn. B.2.

The second approximation we make is that $G \ll \Gamma_e$. This is justified because for most measurements, $\Delta \gg k_B T$ and hence $G \approx We^{-\Delta/k_B T}$ is exponentially suppressed. At the lowest magnetic fields $e^{-\Delta/k_B T} \approx 0.1$ but at these fields $W \sim 1$ Hz, so G is still small compared to Γ_e. With these approximations we have

$$P_e(t_w) = \frac{1 - e^{-Wt_w}}{1 + e^{\Delta/k_B T}} + \epsilon_i \frac{\Gamma_e}{\Gamma_t} \frac{\Gamma_t}{\Gamma_t - W}(e^{-Wt_w} - e^{-\Gamma_t t_w}) \qquad \text{(B.3)}$$

where we can safely neglect the first term when $\Delta \gg k_B T$.

---

[1] Both the field dependence measurements of W are made at V_{shape} settings where $\chi \gtrsim 0.5$ and the shape dependence of W is measured at $B = 3$ T, where $\chi \approx 1$.

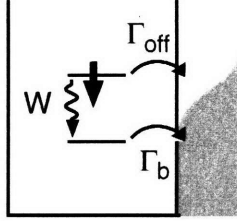# B.2 Probability distribution for tunnel-off events in the read-out state

Figure B-2: Diagram of the processes that can occur during the read-out of the spin state in the spin relaxation measurement experiments.

In this section we consider tunnel-off events, like the one shown in Fig. 5-3(a), that occur when the dot is in the read-out configuration of the spin relaxation measurement sequence. This configuration is illustrated above in Fig. B-2. The goal of this section is to calculate the probability distribution $\mathcal{P}_{ro}$ of the times t_{off} at which electrons tunnel off the dot. This distribution will describe the histograms shown in Fig. 5-5. In this calculation we neglect the transition rate G from the ground to the excited spin state because it is very slow compared to the other rates in the problem, and so we can approximate $W_e = W$.

First we consider the probability $P_{ro,e}(t_{off})$ that a time t_{off} after we enter the read-out state the electron is still in the excited spin state. The rate equation for $P_{ro,e}$ is given by

$$\dot{P}_{ro,e} = -\Gamma_{off} P_{ro,e} - W P_{ro,e} = -(\Gamma_{off} + W) P_{ro,e}.$$

Solving this gives

$$P_{ro,e}(t_{off}) = P_e e^{-R t_{off}}$$

where $R = \Gamma_{off} + W$. We note that $P_e = P_{ro,e}(t_{off} = 0) = P_e(t_w)$ is just the probability that the dot is in the excited spin state at the end of the charging pulse. We can also write down the rate equations for the probability $P_{ro,g}(t_{off})$ that the electron

136

is in the ground spin state at a time t_{off} after we enter the read-out configuration. The rate equation is

$$
\begin{aligned}
\dot{P}_{ro,g} &= -\Gamma_b P_{ro,g} + W P_{ro,e} \\
&= -\Gamma_b P_{ro,g} + W P_e e^{-Rt_{off}}.
\end{aligned}
$$

We can solve this equation and we obtain

$$
P_{ro,g}(t_{off}) = P_g e^{-\Gamma_b t_{off}} + P_e \frac{W}{R - \Gamma_b}(e^{-\Gamma_b t_{off}} - e^{-Rt_{off}})
$$

where $P_g = P_g(t_w)$. The first term in this equations are from electrons that start in the ground spin state at the beginning of the read-out step, while the second term is caused by electrons relaxing from the excited to the ground spin state during the read-out.

We can now calculate the probability distribution $\mathcal{P}_{ro}(t_{off})$. The probability that an electron tunnels off the dot between t_{off} and $t_{off} + \Delta t$ is

$$
\mathcal{P}_{ro}(t_{off})\Delta t = \Gamma_{off}\Delta t \; P_{ro,e}(t_{off}) + \Gamma_b \Delta t \; P_{ro,g}(t_{off}).
$$

To understand this equation, we note that given the electron is in the excited spin state at time t_{off} (which happens with probability $P_{ro,e}(t_{off})$), the probability it tunnels off between t_{off} and $t_{off} + \Delta t$ is just $\Gamma_{off}\Delta t$. Similarly, the probability of tunneling off the dot given the electron is in the ground state at t_{off} is $\Gamma_b \Delta t$. Substituting our results for $P_{ro,e}(t_{off})$ and $P_{ro,g}(t_{off})$ into the above equation and simplifying, we obtain

$$
\mathcal{P}_{ro}(t_{off}) = \left(1 - \frac{W}{R - \Gamma_b}\frac{\Gamma_b}{\Gamma_{off}}\right)\frac{\Gamma_{off}}{R}P_e R \; e^{-Rt_{off}} + \left(P_g + \frac{W}{R - \Gamma_b}P_e\right)\Gamma_b \; e^{-\Gamma_b t_{off}}.
\tag{B.4}
$$

There are a couple of important things to note about this equation. First, $\int_0^\infty \mathcal{P}_{ro}(t_{off})dt_{off} = P_e + P_g$, which is just the total probability that an electron is on the dot after the charging pulse. The first exponential in the equation has rate

$R = \Gamma_{off} + W$ and corresponds to electrons leaving the excited spin state by tunneling off the dot or relaxing to the ground state. The area under this first exponential is P_e multiplied by a factor $\eta = (1 - \frac{W}{R-\Gamma_b}\frac{\Gamma_b}{\Gamma_{off}})\frac{\Gamma_{off}}{R}$, which describes the fraction of excited state electrons that tunnel off before they relax. In the limit $\Gamma_{off} \gg (W, \Gamma_b)$ we have that $\eta \approx 1$. We can simplify the expression for η further. At low magnetic fields $W \ll \Gamma_{off}$ and $\Gamma_b/\Gamma_{off} \approx 0.1$, so that $\frac{W}{R-\Gamma_b}\frac{\Gamma_b}{\Gamma_{off}} \ll 1$. At high magnetic fields $W \sim \Gamma_{off}$ so $W/R \sim 1$. But at these fields the Zeeman splitting is large so that $\Gamma_{off} \gg \Gamma_b$ so again $\frac{W}{R-\Gamma_b}\frac{\Gamma_b}{\Gamma_{off}} \ll 1$. Thus we can simplify the expression for η to $\eta \approx \Gamma_{off}/R$.

The second exponential in Eqn. B.4 corresponds to electrons tunneling out of the ground state. There are two contributions: one from electrons initially in the ground state and a second from electrons that relax to the ground state before tunneling off. In the limit where $\Gamma_b \ll R$, then $e^{-\Gamma_b t_{off}}$ is approximately constant over the scale of $e^{-R t_{off}}$. Thus

$$\mathcal{P}_{ro}(t_{off}) = \eta P_e R\, e^{-R t_{off}} + \left(P_g + \frac{W}{R - \Gamma_b} P_e \right) \Gamma_b \tag{B.5}$$

which is the form we fit to in Chapter 5.

Appendix C

Spin Relaxation in a Rotated

Anisotropic Quantum Dot

We consider a quantum dot with coordinate system x and y such that we can approximate the confining potential by an anisotropic 2D harmonic oscillator potential $U(x,y) = \frac{1}{2}m^*(\omega_x^2 x^2 + \omega_y^2 y^2)$, where m^* is the effective mass. We assume that the z-axis is along the [001] crystallographic axis but that the x and y axes are rotated by an angle ϕ_c with respect to the crystallographic axes $x' = [100]$ and $y' = [010]$. The goal of this calculation is to show that the spin relaxation rate W_0 at $T = 0$ takes the form $W_0 = A_x(\hbar\omega_x)^{-4} + A_y(\hbar\omega_y)^{-4}$.

The form of the spin-orbit Hamiltonian will depend on how the x and y axes are oriented with respect to the GaAs crystallographic axes. The most general spin-orbit Hamiltonian has the form

$$H_{SO} = \sum_{i,j=x,y} B_{ij} p_i \sigma_j = B_{xx} p_x \sigma_x + B_{xy} p_x \sigma_y + B_{yx} p_y \sigma_x + B_{yy} p_y \sigma_y$$

where we assume the B_{ij} are real. For the quantum dot in this thesis, we have $x = [110]$ and $y = [\bar{1}10]$ so $B_{xx} = B_{yy} = 0$, $B_{yx} = (\beta - \alpha)$, and $B_{xy} = (\beta + \alpha)$, where β and α are the Dresselhaus and Rashba spin-orbit parameters. But we shall proceed with the most general form of H_{SO} to derive the spin relaxation rate W_0.

In the absence of spin-orbit coupling the eigenstates of the dot are 2D harmonic

oscillator eigenstates $|n_x, n_y, s\rangle$ where n_x and n_y are the orbital states of the harmonic oscillator potential and $s = +, -$ are the spin-up and spin-down states along the magnetic field direction $\hat{\mathbf{B}}$. The energy difference between the spin states is the Zeeman energy for spin splitting $\Delta = |g|\mu_B B$. We treat the spin-orbit interaction in perturbation theory. Then the effective states to first order in H_{SO} are:

$$|00+\rangle_{SO} = |00+\rangle + \sum_{n_x, n_y, s} \frac{|n_x, n_y, s\rangle\langle n_x, n_y, s|H_{SO}|00+\rangle}{E_{00+} - E_{n_x, n_y, s}}$$

and

$$|00-\rangle_{SO} = |00-\rangle + \sum_{n_x, n_y, s} \frac{|n_x, n_y, s\rangle\langle n_x, n_y, s|H_{SO}|00-\rangle}{E_{00-} - E_{n_x, n_y, s}}$$

For an electron-phonon interaction U_{e-ph} the matrix element to first order in H_{SO} is

$$
\begin{aligned}
M &= {}_{SO}\langle 00-|U_{e-ph}|00+\rangle_{SO} \\
&= \langle 00-|U_{e-ph}|00+\rangle \\
&+ \sum_{n_x, n_y, s} \frac{\langle 00-|U_{e-ph}|n_x, n_y, s\rangle\langle n_x, n_y, s|H_{SO}|00+\rangle}{E_{00+} - E_{n_x, n_y, s}} \\
&+ \sum_{n_x, n_y, s} \frac{\langle 00-|H_{SO}|n_x, n_y, s\rangle\langle n_x, n_y, s|U_{e-ph}|00+\rangle}{E_{00-} - E_{n_x, n_y, s}}
\end{aligned}
$$

Now U_{e-ph} cannot flip the electron's spin [45], so $\langle 00-|U_{e-ph}|00+\rangle = 0$ and

$$
\begin{aligned}
M &= \sum_{n_x, n_y} \frac{\langle 00-|U_{e-ph}|n_x, n_y, -\rangle\langle n_x, n_y, -|H_{SO}|00+\rangle}{E_{00+} - E_{n_x, n_y, -}} \\
&+ \sum_{n_x, n_y} \frac{\langle 00-|H_{SO}|n_x, n_y, +\rangle\langle n_x, n_y, +|U_{e-ph}|00+\rangle}{E_{00-} - E_{n_x, n_y, +}}
\end{aligned}
$$

In the limit where the phonon wavelength is much larger than the size of the dot we can use the dipole approximation for the interaction and we have $U_{e-ph} = -e\mathbf{E}_{\mathbf{q},\alpha}\cdot\mathbf{r}$ where $\alpha = t, l$ refers to the two transverse phonon modes and the one longitudinal mode. From the form of U_{e-ph} we have that $\mathbf{E}_{\mathbf{q},\alpha} = E_{\mathbf{q},\alpha}\hat{\mathbf{q}}$. Thus we can write $U_{e-ph} = -eE_{\mathbf{q},\alpha}(\hat{q}_x x + \hat{q}_y y + \hat{q}_z z)$ where $\hat{\mathbf{q}} = (\cos(\phi)\sin(\theta), \sin(\phi)\sin(\theta), \cos(\theta))$ and θ

and ϕ are the polar and azimuthal angles of the wave-vector $\mathbf{q}$ in the x-y coordinate system.

For the anisotropic harmonic oscillator potential, we have $x = \sqrt{\frac{\hbar}{2m^*\omega_x}}(a_x^\dagger + a_x)$, $p_x = i\sqrt{\frac{m^*\hbar\omega_x}{2}}(a_x^\dagger - a_x)$, and similarly for y and p_y where $a^\dagger$ and a are raising and lowering operators. This gives

$$
\begin{aligned}
M = {} & -eE_{\mathbf{q},\alpha}\sin(\theta)[\\
& \frac{\langle 00|\cos(\phi)x|10\rangle B_{xx}\langle 10|p_x|00\rangle\langle -|\sigma_x|+\rangle}{-(\hbar\omega_x + \Delta)} \\
& + \frac{\langle 00|\cos(\phi)x|10\rangle B_{xy}\langle 10|p_x|00\rangle\langle -|\sigma_y|+\rangle}{-(\hbar\omega_x + \Delta)} \\
& + \frac{\langle 00|\sin(\phi)y|01\rangle B_{yx}\langle 01|p_y|00\rangle\langle -|\sigma_x|+\rangle}{-(\hbar\omega_y + \Delta)} \\
& + \frac{\langle 00|\sin(\phi)y|01\rangle B_{yy}\langle 01|p_y|00\rangle\langle -|\sigma_y|+\rangle}{-(\hbar\omega_y + \Delta)} \\
& + \frac{B_{xx}\langle -|\sigma_x|+\rangle\langle 00|p_x|10\rangle\langle 10|\cos(\phi)x|00\rangle}{-(\hbar\omega_x - \Delta)} \\
& + \frac{B_{xy}\langle -|\sigma_y|+\rangle\langle 00|p_x|10\rangle\langle 10|\cos(\phi)x|00\rangle}{-(\hbar\omega_x - \Delta)} \\
& + \frac{B_{yx}\langle -|\sigma_x|+\rangle\langle 00|p_y|01\rangle\langle 01|\sin(\phi)y|00\rangle}{-(\hbar\omega_y - \Delta)} \\
& + \frac{B_{yy}\langle -|\sigma_y|+\rangle\langle 00|p_y|01\rangle\langle 01|\sin(\phi)y|00\rangle}{-(\hbar\omega_y - \Delta)}]
\end{aligned}
$$

so

$$
\begin{aligned}
M = {} & \frac{ei\hbar}{2}E_{\mathbf{q},\alpha}\sin(\theta)[\\
& \frac{\cos(\phi)B_{xx}\langle -|\sigma_x|+\rangle}{\hbar\omega_x + \Delta} + \frac{\cos(\phi)B_{xy}\langle -|\sigma_y|+\rangle}{\hbar\omega_x + \Delta} \\
& + \frac{\sin(\phi)B_{yx}\langle -|\sigma_x|+\rangle}{\hbar\omega_y + \Delta} + \frac{\sin(\phi)B_{yy}\langle -|\sigma_y|+\rangle}{\hbar\omega_y + \Delta} \\
& - \frac{B_{xx}\langle -|\sigma_x|+\rangle\cos(\phi)}{\hbar\omega_x - \Delta} - \frac{B_{xy}\langle -|\sigma_y|+\rangle\cos(\phi)}{\hbar\omega_x - \Delta} \\
& - \frac{B_{yx}\langle -|\sigma_x|+\rangle\sin(\phi)}{\hbar\omega_y - \Delta} - \frac{B_{yy}\langle -|\sigma_y|+\rangle\sin(\phi)}{\hbar\omega_y - \Delta}]
\end{aligned}
$$

Using $\Delta \ll \hbar\omega_x, \hbar\omega_y$, we have

$$
\begin{aligned}
M = \;& -eih\Delta E_{\mathbf{q},\alpha}\sin(\theta)[\\
& \frac{\cos(\phi)B_{xx}\langle -|\,\sigma_x\,|+\rangle}{(\hbar\omega_x)^2} + \frac{\sin(\phi)B_{yx}\langle -|\,\sigma_x\,|+\rangle}{(\hbar\omega_y)^2} \\
& + \frac{\cos(\phi)B_{xy}\langle -|\,\sigma_y\,|+\rangle}{(\hbar\omega_x)^2} + \frac{\sin(\phi)B_{yy}\langle -|\,\sigma_y\,|+\rangle}{(\hbar\omega_y)^2}]
\end{aligned}
$$

To evaluate the matrix elements of the σ matrices, we use the spin eigenstates in the $\mathbf{B}$ direction in the σ_z basis: $|+\rangle = (\cos(\vartheta/2)e^{-i\varphi/2}, \sin(\vartheta/2)e^{i\varphi/2})$ and $|-\rangle = (\sin(\vartheta/2)e^{-i\varphi/2}, -\cos(\vartheta/2)e^{i\varphi/2})$, where ϑ and φ are the polar and azimuthal angles of the magnetic field with respect to the x and y axes. Then it is easy to compute that $\langle -|\,\sigma_x\,|+\rangle = i\sin(\varphi) - \cos(\vartheta)\cos(\varphi)$ and $\langle -|\,\sigma_y\,|+\rangle = -i\cos(\varphi) - \cos(\vartheta)\sin(\varphi)$. So we have

$$
M = -eih\Delta E_{\mathbf{q},\alpha}\sin(\theta)\left[\frac{\cos(\phi)M_x}{(\hbar\omega_x)^2} + \frac{\sin(\phi)M_y}{(\hbar\omega_y)^2}\right]
$$

with $M_x = B_{xx}\langle -|\,\sigma_x\,|+\rangle + B_{xy}\langle -|\,\sigma_y\,|+\rangle$ and $M_y = B_{yx}\langle -|\,\sigma_x\,|+\rangle + B_{yy}\langle -|\,\sigma_y\,|+\rangle$.

The spin relaxation rate is given by Fermi's Golden Rule [45]:

$$
W_0 = \sum_\alpha \frac{2\pi}{\hbar}\int\frac{d^3q}{(2\pi)^3}|M(\mathbf{q},\alpha)|^2\delta(\hbar s_\alpha q - \Delta)
$$

where s_α is the sound velocity of phonon mode α. The δ function arises from energy conservation. Let's consider the relaxation rate for one phonon mode $W_{0,\alpha}$; the total rate will be the sum of the contributions from the two transverse and one longitudinal modes. We have

$$
\begin{aligned}
W_{0,\alpha} &= \frac{2\pi}{\hbar}\int\frac{d^3q}{(2\pi)^3}|M(\mathbf{q},\alpha)|^2\delta(\hbar s_\alpha q - \Delta) \\
&= \frac{q^2}{(2\pi)^2\hbar^2 s_\alpha}\int\sin(\theta)d\theta d\phi|M(\mathbf{q},\alpha)|^2
\end{aligned}
$$

142

where $q = \Delta/(\hbar s_\alpha)$ from energy conservation. Then

$$
\begin{aligned}
W_{0,\alpha} &= \frac{e^2 \Delta^2 q^2}{(2\pi)^2 s_\alpha} \int d\theta d\phi \sin^3(\theta) |E_{\mathbf{q},\alpha}|^2 \left| \frac{M_x \cos(\phi)}{(\hbar\omega_x)^2} + \frac{M_y \sin(\phi)}{(\hbar\omega_y)^2} \right|^2 \\
&= \frac{e^2 \Delta^2 q^2}{(2\pi)^2 s_\alpha} \int d\theta d\phi \sin^3(\theta) |E_{\mathbf{q},\alpha}|^2 \left[\frac{|M_x|^2 \cos^2(\phi)}{(\hbar\omega_x)^4} + \frac{|M_y|^2 \sin^2(\phi)}{(\hbar\omega_y)^4} \right] \\
&+ \frac{e^2 \Delta^2 q^2}{(2\pi)^2 s_\alpha} \int d\theta d\phi \sin^3(\theta) |E_{\mathbf{q},\alpha}|^2 \left(\frac{2\Re e(M_x M_y^*) \cos(\phi) \sin(\phi)}{(\hbar\omega_x)^2 (\hbar\omega_y)^2} \right).
\end{aligned}
$$

To integrate over $E_{\mathbf{q},\alpha}$ we must consider the details of piezoelectric phonons in GaAs. The electron-phonon interaction is given by [45]:

$$
U_{e-ph}^{\mathbf{q},\alpha} = \sqrt{\frac{\hbar}{2\rho\omega}} exp(i\mathbf{q}\cdot\mathbf{r} - i\omega t) e A_{\mathbf{q},\alpha} + c.c.
$$

with $A_{\mathbf{q},\alpha} = \hat{q}_{i'} \hat{q}_{k'} \beta_{i'k'j'} e_{\mathbf{q},\alpha}^{j'}$ where $\mathbf{e}_{\mathbf{q},\alpha}$ is the phonon polarization vector ($e_{\mathbf{q},\alpha}^{j'}$ are the components of this vector), and $\beta_{i'k'j'} = h_{14}$ when the i', k', j' are different and 0 otherwise. The components of the vectors are to be taken in the crystallographic coordinate system given by the x' and y' axes. ρ is the mass density. Following a dipole expansion, we have that $E_{\mathbf{q},\alpha} = \mathcal{E}_{q,\alpha} A_{\mathbf{q},\alpha}$, with $A_{\mathbf{q},\alpha} = 2h_{14}(\hat{q}_{x'} \hat{q}_{y'} e_{\mathbf{q},\alpha}^{z'} + \hat{q}_{x'} \hat{q}_{z'} e_{\mathbf{q},\alpha}^{y'} + \hat{q}_{y'} \hat{q}_{z'} e_{\mathbf{q},\alpha}^{x'})$ containing all the angular dependence for $E_{\mathbf{q},\alpha}$ while $\mathcal{E}_{q,\alpha} = -iq\sqrt{\frac{\hbar}{2\rho\omega}}$ depends only on the magnitude of $\mathbf{q}$.

Substituting,

$$
W_{0,\alpha} = C_\alpha \left(\frac{|M_x|^2 I_{x,\alpha}}{(\hbar\omega_x)^4} + \frac{|M_y|^2 I_{y,\alpha}}{(\hbar\omega_y)^4} + \frac{\Re e(M_x M_y^*) I_{xy,\alpha}}{(\hbar\omega_x)^2 (\hbar\omega_y)^2} \right) \tag{C.1}
$$

where $C_\alpha = \frac{e^2 \Delta^2 q^2}{(2\pi)^2 s_\alpha} |\mathcal{E}_{q,\alpha}|^2$, $q = \Delta/(\hbar s_\alpha)$, and the integrals are given by:

$$
\begin{aligned}
I_{x,\alpha} &= \int d\theta d\phi \sin^3(\theta) |A_{\mathbf{q},\alpha}|^2 \cos^2(\phi) \\
I_{y,\alpha} &= \int d\theta d\phi \sin^3(\theta) |A_{\mathbf{q},\alpha}|^2 \sin^2(\phi)
\end{aligned}
$$

and

$$
I_{xy,\alpha} = \int d\theta d\phi \sin^3(\theta) |A_{\mathbf{q},\alpha}|^2 \sin(2\phi)
$$

We now consider these integrals for each of the phonon modes. For longitudinal phonons, $\mathbf{e}_{\mathbf{q},l} = \hat{\mathbf{q}}$ so $e^{j'}_{\mathbf{q},l} = \hat{q}_{j'}$ and

$$A_{\mathbf{q},l} = 6h_{14}(\hat{q}_{x'}\hat{q}_{y'}\hat{q}_{z'}) = 6h_{14}\sin^2(\theta')\cos(\theta')\cos(\phi')\sin(\phi')$$

where θ' and ϕ' are the polar and azimuthal angles with respect to the crystallographic axes. Since the z axis is the $z' = [001]$ crystallographic axis, we have $\theta = \theta'$. As discussed earlier, we assume the x-y axes are rotated an angle ϕ_c from the crystallographic axes so that $\phi' = \phi + \phi_c$. Then we can evaluate the integrals to find that

$$I_{x,l} \quad = \quad I_{y,l} \quad = \quad 16\pi h_{14}^2/35$$

$$\text{and}$$

$$I_{xy,l} \quad = \quad 0.$$

This last integral results because

$$I_{xy,l} \quad \propto \quad \int d\phi \cos^2(\phi')\sin^2(\phi')\sin(2\phi)$$

$$= \quad 1/4 \int d\phi \sin^2(2\phi')\sin(2\phi)$$

$$= \quad 1/8 \int d\phi(1 - \cos(4\phi'))\sin(2\phi)$$

$$= \quad 1/8 \int d\phi(1 - \cos(4\phi)\cos(4\phi_c) + \sin(4\phi)\sin(4\phi_c))\sin(2\phi)$$

$$= \quad 0.$$

For the transverse modes, we have to pick the phonon polarization vectors. Natural vectors to choose are $\hat{\mathbf{e}}_{\mathbf{q},t1} = (-\sin(\phi'), \cos(\phi'), 0) = (\hat{\mathbf{z}}' \times \hat{\mathbf{q}})/\sin(\theta')$ and $\hat{\mathbf{e}}_{\mathbf{q},t2} = (-\cos(\phi')\cos(\theta'), -\sin(\phi')\cos(\theta'), \sin(\theta')) = \hat{\mathbf{q}} \times \hat{\mathbf{e}}_{\mathbf{q},t1}$. Then

$$A_{\mathbf{q},t1} = 2h_{14}\sin(\theta')\cos(\theta')(\cos^2(\phi') - \sin^2(\phi'))$$

and

$$A_{\mathbf{q},t2} = 2h_{14}\sin(\theta')\cos(\phi')\sin(\phi')(1 - 3\cos^2(\theta'))$$

144

What is usually done [45, 96, 127] is to take the average transverse mode given by $|A_{\mathbf{q},t}|^2 = (|A_{\mathbf{q},t1}|^2 + |A_{\mathbf{q},t2}|^2)/2$ which gives

$$|A_{\mathbf{q},t}|^2 = 2h_{14}^2[\sin^2(\theta')\cos^2(\theta') + \cos^2(\phi')\sin^2(\phi')\sin^4(\theta')(1 - 9\cos^2(\theta'))].$$

Using this average gives equivalent results to considering the modes independently. For the transverse modes, we have

$$I_{x,t} = I_{y,t} = 32\pi h_{14}^2/105$$

$$\text{and}$$

$$I_{xy,t} = 0.$$

This last integral results because

$$I_{xy,t} \propto \int d\theta d\phi[\sin^2(\theta')\cos^2(\theta') + \cos^2(\phi')\sin^2(\phi')\sin^4(\theta')(1 - 9\cos^2(\theta'))]\sin(2\phi)$$

$$= \int d\theta d\phi[\cos^2(\phi')\sin^2(\phi')\sin^4(\theta')(1 - 9\cos^2(\theta'))]\sin(2\phi)$$

$$\propto \int d\phi[\cos^2(\phi')\sin^2(\phi')]\sin(2\phi)$$

$$= 0.$$

The total relaxation rate is obtained by summing Eqn. C.1 over the phonon modes:

$$W_0 = C\left(\frac{|M_x|^2}{(\hbar\omega_x)^4} + \frac{|M_y|^2}{(\hbar\omega_y)^4}\right) \tag{C.2}$$

$$M_x = B_{xx}(i\sin(\varphi) - \cos(\vartheta)\cos(\varphi)) + B_{xy}(-i\cos(\varphi) - \cos(\vartheta)\sin(\varphi))$$

$$M_y = B_{yx}(i\sin(\varphi) - \cos(\vartheta)\cos(\varphi)) + B_{yy}(-i\cos(\varphi) - \cos(\vartheta)\sin(\varphi))$$

and using the fact that $I_{x,\alpha} = I_{y,\alpha}$, we have $C = \sum_\alpha C_\alpha I_{x,\alpha} \propto h_{14}^2 \rho^{-1}\Delta^5(s_l^{-5} + \frac{4}{3}s_t^{-5})$. Equation C.2 is the form of W_0 we wanted to demonstrate.

Finally, to check our work, we compare our results to those in Khaetskii *et al.* [45] for the anisotropic harmonic oscillator potential. The result in [45] are for $x = [100]$

and $y = [010]$ and only Dresselhaus spin-orbit coupling so $B_{xx} = -\beta$, $B_{yy} = \beta$, and $B_{xy} = B_{yx} = 0$. Then we have $M_x = -\beta(i\sin(\varphi) - \cos(\vartheta)\cos(\varphi))$ and $M_y = \beta(-i\cos(\varphi) - \cos(\vartheta)\sin(\varphi))$, so $|M_x|^2 = \beta^2(\sin^2(\varphi) + \cos^2(\vartheta)\cos^2(\varphi))$ and $|M_y|^2 = \beta^2(\cos^2(\varphi) + \cos^2(\vartheta)\sin^2(\varphi))$. Substituting into Eqn. C.2 we have

$$
\begin{aligned}
W_0 \; &\propto \; \frac{\sin^2(\varphi) + \cos^2(\vartheta)\cos^2(\varphi)}{(\hbar\omega_x)^4} + \frac{\cos^2(\varphi) + \cos^2(\vartheta)\sin^2(\varphi)}{(\hbar\omega_y)^4} \\
&\propto \; \frac{1 - \cos(2\varphi) + \cos^2(\vartheta)(1 + \cos(2\varphi))}{(\hbar\omega_x)^4} + \frac{1 + \cos(2\varphi) + \cos^2(\vartheta)(1 - \cos(2\varphi))}{(\hbar\omega_y)^4} \\
&= \; \frac{1 + \cos^2(\vartheta) - \sin^2(\vartheta)\cos(2\varphi)}{(\hbar\omega_x)^4} + \frac{1 + \cos^2(\vartheta) + \sin^2(\vartheta)\cos(2\varphi)}{(\hbar\omega_y)^4} \\
&= \; (1 + \cos^2(\vartheta))((\hbar\omega_x)^{-4} + (\hbar\omega_y)^{-4}) - \sin^2(\vartheta)\cos(2\varphi)((\hbar\omega_x)^{-4} - (\hbar\omega_y)^{-4})
\end{aligned}
$$

This is precisely the form of the result in Eqn. 7 of Khaetskii *et al.* [45] when we note that $\alpha_{xx} \propto (\hbar\omega_x)^{-2}$ and $\alpha_{yy} \propto (\hbar\omega_y)^{-2}$.

We can also compare our results to those in Golovach *et al.* [46], for $x = [100]$, $y = [010]$ and $\hbar\omega_x = \hbar\omega_y$. Then $B_{xx} = -\beta$, $B_{xy} = \alpha$, $B_{yx} = -\alpha$, and $B_{yy} = \beta$ which gives

$$
\begin{aligned}
M_x &= -\beta(i\sin(\varphi) - \cos(\vartheta)\cos(\varphi)) + \alpha(-i\cos(\varphi) - \cos(\vartheta)\sin(\varphi)) \\
M_y &= -\alpha(i\sin(\varphi) - \cos(\vartheta)\cos(\varphi)) + \beta(-i\cos(\varphi) - \cos(\vartheta)\sin(\varphi))
\end{aligned}
$$

Then we have

$$
\begin{aligned}
W_0 &= \frac{C}{(\hbar\omega_x)^4}|(\beta\cos(\varphi) - \alpha\sin(\varphi))\cos(\vartheta) - i(\alpha\cos(\varphi) + \beta\sin(\varphi))|^2 \\
&+ \frac{C}{(\hbar\omega_x)^4}|(\alpha\cos(\varphi) - \beta\sin(\varphi))\cos(\vartheta) - i(\beta\cos(\varphi) + \alpha\sin(\varphi))|^2 \\
&= \frac{C}{(\hbar\omega_x)^4}[(\beta\cos(\varphi) - \alpha\sin(\varphi))^2\cos^2(\vartheta) + (\alpha\cos(\varphi) + \beta\sin(\varphi))^2] \\
&+ \frac{C}{(\hbar\omega_x)^4}[(\alpha\cos(\varphi) - \beta\sin(\varphi))^2\cos^2(\vartheta) + (\beta\cos(\varphi) + \alpha\sin(\varphi))^2] \\
&= \frac{C}{(\hbar\omega_x)^4}[(\alpha^2 + \beta^2)\cos^2(\vartheta) - 4\alpha\beta\cos(\varphi)\sin(\varphi)\cos^2(\vartheta) \\
&\quad + (\alpha^2 + \beta^2) + 4\alpha\beta\cos(\varphi)\sin(\varphi)]
\end{aligned}
$$

so that

$$W_0 = \frac{C}{(\hbar \omega_x)^4} [(\alpha^2 + \beta^2)(1 + \cos^2(\vartheta)) + 2\alpha\beta \sin(2\varphi) \sin^2(\vartheta)].$$

For $\vartheta = \pi/2$ and $\alpha = 0$, we have $W(\vartheta = \pi/2, \alpha = 0) = \frac{C\beta^2}{(\hbar \omega_x)^4}$ so that $\frac{C}{(\hbar \omega_x)^4} = W(\vartheta = \pi/2, \alpha = 0)/\beta^2$ and we have

$$W = \left(\frac{W(\vartheta = \pi/2, \alpha = 0)}{\beta^2} \right) [(\alpha^2 + \beta^2)(1 + \cos^2(\vartheta)) + 2\alpha\beta \sin(2\varphi) \sin^2(\vartheta)].$$

This is the result in Golovach $et\ al.$ [46].

Bibliography

[1] M. A. Kastner, Reviews of Modern Physics **64**, 849 (1992).

[2] M. A. Kastner, Physics Today **46**, 24 (1993).

[3] R. C. Ashoori, Nature **379**, 413 (1996).

[4] L. P. Kouwenhoven, C. M. Marcus, P. L. McEuen, S. Tarucha, R. M. Wester-velt, and N. S. Wingreen, Electron transport in quantum dots, in *Mesoscopic Electron Transport*, edited by L. L. Sohn, L. P. Kouwenhoven, and G. Schön, volume 345 of *NATO ASI Series E*, pp. 105–214, Kluwer, Dordrecht, 1997.

[5] L. Kouwenhoven and C. Marcus, Physics World **11**, 35 (1998).

[6] C. B. Murray, D. J. Norris, and M. G. Bawendi, Journal of the American Chemical Society **115**, 8706 (1993).

[7] M. J. Biercuk, S. Garaj, N. Mason, J. M. Chow, and C. M. Marcus, Nano Letters **5**, 1267 (2005).

[8] C. Fasth, A. Fuhrer, M. T. Björk, and L. Samuelson, Nano Letters **5**, 1487 (2005).

[9] J. H. Davies, *The Physics of Low-Dimensional Semiconductors* (Cambridge University Press, Cambridge, 1998).

[10] T. K. Ng and P. A. Lee, Physical Review Letters **61**, 1768 (1988).

[11] L. I. Glazman and M. E. Raikh, JETP Letters **47**, 452 (1988).

[12] D. Goldhaber-Gordon, H. Shtrikman, D. Mahalu, D. Abush-Magder, U. Meirav, and M. A. Kastner, Nature **391**, 156 (1998).

[13] S. M. Cronenwett, T. H. Oosterkamp, and L. P. Kouwenhoven, Science **281**, 540 (1998).

[14] D. Goldhaber-Gordon, J. Göres, M. A. Kastner, H. Shtrikman, D. Mahalu, and U. Meirav, Physical Review Letters **81**, 5225 (1998).

[15] Y. Meir, N. S. Wingreen, and P. A. Lee, Physical Review Letters **70**, 2601 (1993).

[16] J. E. Moore and X.-G. Wen, Physical Review Letters **85**, 1722 (2000).

[17] T. A. Costi, Physical Review Letters **85**, 1504 (2000).

[18] A. Kogan, S. Amasha, D. Goldhaber-Gordon, G. Granger, M. A. Kastner, and H. Shtrikman, Physical Review Letters **93**, 166602 (2004).

[19] S. Amasha, I. J. Gelfand, M. A. Kastner, and A. Kogan, Physical Review B **72**, 045308 (2005).

[20] A. Kogan, S. Amasha, and M. A. Kastner, Science **304**, 1293 (2004).

[21] S. A. Wolf, D. D. Awschalom, R. A. Buhrman, J. M. Daughton, S. von Molnár, M. L. Roukes, A. Y. Chtchelkanova, and D. M. Treger, Science **294**, 1488 (2001).

[22] I. Žutić, J. Fabian, and S. Das Sarma, Reviews of Modern Physics **76**, 323 (2004).

[23] D. D. Awschalom and M. E. Flatté, Nature Physics **3**, 153 (2007).

[24] J. A. Folk, R. M. Potok, C. M. Marcus, and V. Umansky, Science **299**, 679 (2003).

[25] R. Hanson, L. M. K. Vandersypen, L. H. Willems van Beveren, J. M. Elzerman, I. T. Vink, and L. P. Kouwenhoven, Physical Review B **70**, 241304(R) (2004).

[26] S. K. Watson, R. M. Potok, C. M. Marcus, and V. Umansky, Physical Review Letters **91**, 258301 (2003).

[27] P. Recher, E. V. Sukhorukov, and D. Loss, Physical Review Letters **85**, 1962 (2000).

[28] M. Kroutvar, Y. Ducommun, D. Heiss, M. Bichler, D. Schuh, G. Abstreiter, and J. J. Finley, Nature **432**, 81 (2004).

[29] D. Loss and D. P. DiVincenzo, Physical Review A **57**, 120 (1998).

[30] D. P. DiVincenzo, Science **270**, 255 (1995).

[31] D. P. DiVincenzo, cond-mat/9612126, 1996.

[32] F. H. L. Koppens, C. Buizert, K. J. Tielrooij, I. T. Vink, K. C. Nowack, T. Meunier, L. P. Kouwenhoven, and L. M. K. Vandersypen, Nature **442**, 766 (2006).

[33] H.-A. Engel and D. Loss, Physical Review Letters **86**, 4648 (2001).

[34] J. R. Petta, A. C. Johnson, J. M. Taylor, E. A. Laird, A. Yacoby, M. D. Lukin, C. M. Marcus, M. P. Hanson, and A. C. Gossard, Science **309**, 2180 (2005).

[35] J. M. Elzerman, R. Hanson, L. H. Willems van Beveren, B. Witkamp, L. M. K. Vandersypen, and L. P. Kouwenhoven, Nature **430**, 431 (2004).

[36] R. Hanson, L. H. Willems van Beveren, I. T. Vink, J. M. Elzerman, W. J. M. Naber, F. H. L. Koppens, L. P. Kouwenhoven, and L. M. K. Vandersypen, Physical Review Letters **94**, 196802 (2005).

[37] I. A. Merkulov, Al. L. Efros, and M. Rosen, Physical Review B **65**, 205309 (2002).

[38] A. V. Khaetskii, D. Loss, and L. Glazman, Physical Review Letters **88**, 186802 (2002).

[39] K. Ono and S. Tarucha, Physical Review Letters **92**, 256803 (2004).

[40] F. H. L. Koppens, J. A. Folk, J. M. Elzerman, R. Hanson, L. H. Willems van Beveren, I. T. Vink, H. P. Tranitz, W. Wegscheider, L. P. Kouwenhoven, and L. M. K. Vandersypen, Science **309**, 1346 (2005).

[41] A. C. Johnson, J. R. Petta, J. M. Taylor, A. Yacoby, M. D. Lukin, C. M. Marcus, M. P. Hanson, and A. C. Gossard, Nature **435**, 925 (2005).

[42] D. Klauser, W. A. Coish, and D. Loss, Physical Review B **73**, 205302 (2006).

[43] G. Giedke, J. M. Taylor, D. D'Alessandro, M. D. Lukin, and A. Imamoğlu, Physical Review A **74**, 032316 (2006).

[44] D. Stepanenko, G. Burkard, G. Giedke, and A. Imamoglu, Physical Review Letters **96**, 136401 (2006).

[45] A. V. Khaetskii and Y. V. Nazarov, Physical Review B **64**, 125316 (2001).

[46] V. N. Golovach, A. Khaetskii, and D. Loss, Physical Review Letters **93**, 016601 (2004).

[47] F. Marquardt and V. A. Abalmassov, Physical Review B **71**, 165325 (2005).

[48] P. San-Jose, G. Zarand, A. Shnirman, and G. Schön , Physical Review Letters **97**, 076803 (2006).

[49] R. C. Ashoori, H. L. Stormer, J. S. Weiner, L. N. Pfeiffer, S. J. Pearton, K. W. Baldwin, and K. W. West, Physical Review Letters **68**, 3088 (1992).

[50] M. Field, C. G. Smith, M. Pepper, D. A. Ritchie, J. E. F. Frost, G. A. C. Jones, and D. G. Hasko, Physical Review Letters **70**, 1311 (1993).

[51] R. J. Schoelkopf, P. Wahlgren, A. A. Kozhevnikov, P. Delsing, and D. E. Prober, Science **280**, 1238 (1998).

[52] L. S. Levitov, H. Lee, and G. B. Lesovik, Journal of Mathematical Physics **37**, 4845 (1996).

[53] S. Gustavsson, R. Leturcq, B. Simovič, R. Schleser, T. Ihn, P. Studerus, K. Ensslin, D. C. Driscoll, and A. C. Gossard, Physical Review Letters **96**, 076605 (2006).

[54] T. Fujisawa, T. Hayashi, R. Tomita, and Y. Hirayama, Science **312**, 1634 (2006).

[55] R. M. Potok, J. A. Folk, C. M. Marcus, V. Umansky, M. Hanson, and A. C. Gossard, Physical Review Letters **91**, 016802 (2003).

[56] E. B. Foxman, *Single Electron Charging and Quantum Effects in Semiconductor Nanostructures*, PhD dissertation, Massachusetts Institute of Technology, Department of Physics, 1993.

[57] D. Goldhaber-Gordon, *The Kondo Effect in a Single-Electron Transistor*, PhD dissertation, Massachusetts Institute of Technology, Department of Physics, 1999.

[58] G. Granger, *Spin Effects in Single-Electron Transistors*, PhD dissertation, Massachusetts Institute of Technology, Department of Physics, 2005.

[59] G. Granger, M. A. Kastner, I. Radu, M. P. Hanson, and A. C. Gossard, Physical Review B **72**, 165309 (2005).

[60] M. Ciorga, A. S. Sachrajda, P. Hawrylak, C. Gould, P. Zawadzki, S. Jullian, Y. Feng, and Z. Wasilewski, Physical Review B **61**, R16315 (2000).

[61] S. Datta, *Electronic Transport in Mesoscopic Systems* (Cambridge University Press, Cambridge, 1995).

[62] P. L. McEuen, E. B. Foxman, U. Meirav, M. A. Kastner, Y. Meir, N. S. Wingreen, and S. J. Wind, Physical Review Letters **66**, 1926 (1991).

[63] P. L. McEuen, E. B. Foxman, J. Kinaret, U. Meirav, M. A. Kastner, N. S. Wingreen, and S. J. Wind, Physical Review B **45**, 11419 (1992).

[64] R. C. Ashoori, H. L. Stormer, J. S. Weiner, L. N. Pfeiffer, K. W. Baldwin, and K. W. West, Physical Review Letters **71**, 613 (1993).

[65] O. Klein, C. de C. Chamon, D. Tang, D. M. Abusch-Magder, U. Meirav, X.-G. Wen, M. A. Kastner, and S. J. Wind, Physical Review Letters **74**, 785 (1995).

[66] B. Schuh, Journal of Physics A **18**, 803 (1985).

[67] C. Weisbuch and C. Hermann, Physical Review B **15**, 816 (1977).

[68] C. Hermann and C. Weisbuch, Physical Review B **15**, 823 (1977).

[69] R. Hanson, B. Witkamp, L. M. K. Vandersypen, L. H. Willems van Beveren, J. M. Elzerman, and L. P. Kouwenhoven, Physical Review Letters **91**, 196802 (2003).

[70] E. Bonet, M. M. Deshmukh, and D. C. Ralph, Physical Review B **65**, 045317 (2002).

[71] M. M. Deshmukh, E. Bonet, A. N. Pasupathy, and D. C. Ralph, Physical Review B **65**, 073301 (2002).

[72] M. Pioro-Ladrière, J. H. Davies, A. R. Long, A. S. Sachrajda, L. Gaudreau, P. Zawadzki, J. Lapointe, J. Gupta, Z. Wasilewski, and S. Studenikin, Physical Review B **72**, 115331 (2005).

[73] D. V. Averin and Y. V. Nazarov, Macroscopic quantum tunneling of charge and co-tunneling, in *Single Charge Tunneling*, edited by H. Grabert and M. H. Devoret, volume 294 of *NATO ASI Series B*, pp. 217-247, Plenum Press, New York, 1992.

[74] D. V. Averin and Y. V. Nazarov, Physical Review Letters **65**, 2446 (1990).

[75] S. De Franceschi, S. Sasaki, J. M. Elzerman, W. G. van der Wiel, S. Tarucha, and L. P. Kouwenhoven, Physical Review Letters **86**, 878 (2001).

[76] J. Lambe and R. C. Jaklevic, Physical Review **165**, 821 (1968).

[77] W. Lu, Z. Ji, L. Pfeiffer, K. W. West, and A. J. Rimberg, Nature **423**, 422 (2003).

[78] R. Schleser, E. Ruh, T. Ihn, K. Ensslin, D. C. Driscoll, and A. C. Gossard, Applied Physics Letters **85**, 2005 (2004).

[79] S. Amasha, K. MacLean, D. M. Zumbühl, I. Radu, M. A. Kastner, M. P. Hanson, and A. Gossard, Proc SPIE **6244**, 624419 (2006).

[80] K. MacLean, S. Amasha, I. P. Radu, D. M. Zumbühl, M. A. Kastner, M. P. Hanson, and A. C. Gossard, Physical Review Letters **98**, 036802 (2007).

[81] B. J. van Wees, H. van Houten, C. W. J. Beenakker, J. G. Williamson, L. P. Kouwenhoven, D. van der Marel, and C. T. Foxon, Physical Review Letters **60**, 848 (1988).

[82] B. J. van Wees, L. P. Kouwenhoven, E. M. M. Willems, C. J. P. M. Harmans, J. E. Mooij, H. van Houten, C. W. J. Beenakker, J. G. Williamson, and C. T. Foxon, Physical Review B **43**, 12431 (1991).

[83] S. Gustavsson, R. Leturcq, B. Simovič, R. Schleser, P. Studerus, T. Ihn, K. Ensslin, D. C. Driscoll, and A. C. Gossard, Physical Review B **74**, 195305 (2006).

[84] S. Machlup, Journal of Applied Physics **25**, 341 (1954).

[85] P. Horowitz and W. Hill, *The Art of Electronics* (Cambridge University Press, Cambridge, 1989).

[86] G. B. Lesovik, Pis'ma Zh. Eksp. Teor. Fiz. **49**, 515 (1989).

[87] M. Büttiker, Physical Review Letters **65**, 2901 (1990).

[88] L. M. K. Vandersypen, J. M. Elzerman, R. N. Schouten, L. H. Willems van Beveren, R. Hanson, and L. P. Kouwenhoven, Applied Physics Letters **85**, 4394 (2004).

[89] I. T. Vink, T. Nooitgedagt, R. N. Schouten, L. M. K. Vandersypen, and W. Wegscheider, Applied Physics Letters **91**, 123512 (2007).

[90] D. J. Reilly, C. M. Marcus, M. P. Hanson, and A. C. Gossard, Applied Physics Letters **91**, 162101 (2007).

[91] M. Thalakulam, W. W. Xue, F. Pan, Z. Ji, J. Stettenheim, L. Pfeiffer, K. W. West, and A. J. Rimberg, cond-mat/0708.0861, 2007.

[92] L.-X. Zhang, J. P. Leburton, R. Hanson, and L. P. Kouwenhoven, Applied Physics Letters **85**, 2628 (2004).

[93] S. Amasha, K. MacLean, I. P. Radu, D. M. Zumbühl, M. A. Kastner, M. P. Hanson, and A. C. Gossard, cond-mat/0707.1656, 2007.

[94] S. Amasha, K. MacLean, I. P. Radu, D. M. Zumbühl, M. A. Kastner, M. P. Hanson, and A. C. Gossard, cond-mat/0709.1730, 2007.

[95] T. Fujisawa, D. G. Austing, Y. Tokura, Y. Hirayama, and S. Tarucha, Nature **419**, 278 (2002).

[96] J. I. Climente, A. Bertoni, G. Goldoni, and E. Molinari, Physical Review B **74**, 035313 (2006).

[97] L. D. Landau and E. M. Lifshitz, *Quantum Mechanics* (Butterworth-Heinemann, Oxford, 2003).

[98] J. J. Sakurai, *Modern Quantum Mechanics* (Addison-Wesley Publishing Company, Inc., Reading, 1994).

[99] J. C. Chen, Z. An, T. Ueda, S. Komiyama, K. Hirakawa, and V. Antonov, Physical Review B **74**, 045321 (2006).

[100] D. H. Cobden, M. Bockrath, P. L. McEuen, A. G. Rinzler, and R. E. Smalley, Physical Review Letters **81**, 681 (1998).

[101] K. Hitachi, M. Yamamoto, and S. Tarucha, Physical Review B **74**, 161301(R) (2006).

[102] O. Zarchin, Y. C. Chung, M. Heiblum, D. Rohrlich, and V. Umansky, Physical Review Letters **98**, 066801 (2007).

[103] I. Hapke-Wurst, U. Zeitler, H. Frahm, A. G. M. Jansen, R. J. Haug, and K. Pierz, Physical Review B **62**, 12621 (2000).

[104] E. E. Vdovin, Y. N. Khanin, O. Makarovsky, Y. V. Dubrovskii, A. Patanè, L. Eaves, M. Henini, C. J. Mellor, K. A. Benedict, and R. Airey, Physical Review B **75**, 115315 (2007).

[105] R. M. Potok, J. A. Folk, C. M. Marcus, and V. Umansky, Physical Review Letters **89**, 266602 (2002).

[106] D. M. Zumbühl, J. B. Miller, C. M. Marcus, K. Campman, and A. C. Gossard, Physical Review Letters **89**, 276803 (2002).

[107] S. Amasha, K. MacLean, I. Radu, D. M. Zumbühl, M. A. Kastner, M. P. Hanson, and A. C. Gossard, cond-mat/0607110, 2006.

[108] R. Hanson, L. P. Kouwenhoven, J. R. Petta, S. Tarucha, and L. M. K. Vandersypen, cond-mat/0610433, 2006.

[109] V. I. Fal'ko, B. L. Altshuler, and O. Tsyplyatyev, Physical Review Letters **95**, 076603 (2005).

[110] P. Stano and J. Fabian, Physical Review Letters **96**, 186602 (2006).

[111] M. Borhani, V. N. Golovach, and D. Loss, Physical Review B **73**, 155311 (2006).

[112] S. I. Erlingsson and Y. V. Nazarov, Physical Review B **66**, 155327 (2002).

[113] C. Calero, E. M. Chudnovsky, and D. A. Garanin, Physical Review Letters **95**, 166603 (2005).

[114] O. Olendski and T. V. Shahbazyan, Physical Review B **75**, 041306 (2007).

[115] T. Meunier, I. T. Vink, L. H. Willems van Beveren, K.-J. Tielrooij, R. Hanson, F. H. L. Koppens, H. P. Tranitz, W. Wegscheider, L. P. Kouwenhoven, and L. M. K. Vandersypen, Physical Review Letters **98**, 126601 (2007).

[116] Y. A. Bychkov and E. I. Rashba, Journal of Physics C **17**, 6039 (1984).

[117] D. J. Griffiths, *Introduction to Electrodynamics* (Prentice Hall, Upper Saddler River, 1999).

[118] D. M. Zumbühl, *Coherence and Spin in GaAs Quantum Dots*, PhD dissertation, Harvard University, Department of Physics, 2004.

[119] G. Dresselhaus, Physical Review **100**, 580 (1955).

[120] F. G. Pikus and G. E. Pikus, Physical Review B **51**, 16928 (1995).

[121] V. F. Gantmakher and Y. B. Levinson, *Carrier Scattering in Metals and Semiconductors* (North-Holland, Amsterdam, 1987).

[122] J. H. Van Vleck, Physical Review **57**, 426 (1940).

[123] Al. L. Efros and E. I. Rashba, Physical Review B **73**, 165325 (2006).

[124] V. N. Golovach, M. Borhani, and D. Loss, Physical Review B **74**, 165319 (2006).

[125] K. C. Nowack, F. H. L. Koppens, Y. V. Nazarov, and L. M. K. Vandersypen, Science **318**, 1430 (2007).

[126] J. B. Miller, D. M. Zumbühl, C. M. Marcus, Y. B. Lyanda-Geller, D. Goldhaber-Gordon, K. Campman, and A. C. Gossard, Physical Review Letters **90**, 076807 (2003).

[127] J. D. Zook, Physical Review **136**, A869 (1964).